ESTROGEN REGULATION OF THE WNT/β-CATENIN PATHWAY

IN OSTEOCYTES IN RESPONSE TO MECHANICAL LOADING

A DISSERTATION IN
Oral and Craniofacial Sciences
And
Pharmacology

Presented to the Faculty of the University
of Missouri-Kansas City in partial fulfillment of
the requirements for the degree

DOCTOR OF PHILOSOPHY

by
ERICA N.M. JACKSON

B.S., Emporia State University, 2006
M.A., Emporia State University, 2008

Kansas City, Missouri
2019

ESTROGEN REGULATION OF THE WNT/β-CATENIN PATHWAY

IN OSTEOCYTES IN RESPONSE TO MECHANICAL LOADING

Erica Jackson, Candidate for the Doctor of Philosophy Degree

University of Missouri-Kansas City, 2019

ABSTRACT

Osteoporosis is a major health concern, especially for women who are peri- and post-menopausal. During this time, estrogen levels dramatically decline followed by a subsequent loss of bone density, which increases risk of bone fracture. The increased fragility of bone negatively affects the patient's quality of life by limiting the performance of everyday activities and increasing the frequency of physician visits and medical care costs. Estrogen exerts its effects on bone at various levels. One important, yet poorly understood, aspect of its action is on the osteocyte, the most abundant cell in bone and thought to be the primary cell involved in sensing mechanical loads. The Wnt/β-catenin pathway is activated in the osteocyte upon mechanical loading. The role of estrogen (specifically estrogen loss) in regulation of this pathway in osteocytes is not fully understood. I hypothesize that estrogen is a critical factor in the responsiveness of the osteocyte to mechanical loading via regulation of the Wnt/β-catenin pathway; and in the absence of estrogen, osteocytes will have a decreased activation upon mechanical loading. The specific aims are: 1) determine the effects of ovariectomy (OVX) on the ability of the osteocyte to activate the Wnt/β-catenin pathway in response to mechanical load; 2) determine the role of estrogen on the activation of the Wnt/β-catenin pathway *in vitro* in response to mechanical load.

The OVX group failed to activate osteocyte β-catenin signaling at 24 hours post-loading, which is normal peak activation time point of the pathway following loading. Trabecular bone had significant decreases in bone mineral density, bone volume/total volume and trabecular thickness in the OVX group, along with increases in osteoclasts and decreases in osteoblast numbers. Bone micro-architecture (lacunar size and volume) and biomechanical properties remained unchanged. *In vitro*

studies showed osteocyte activation with fluid flow and the addition of Wnt3a, and activation was attenuated with the addition of an estrogen receptor inhibitor. These findings are consistent with a change in the intrinsic ability of the osteocyte to respond to loading in the absence of estrogen and support the hypothesis that estrogen plays a critical role in the osteocyte's responsiveness to mechanical loading.

APPROVAL PAGE

The faculty listed below, appointed by the Dean of the School of Graduate Studies have examined a dissertation titled “Estrogen Regulation of the Wnt/β-catenin Pathway in Osteocytes in Response to Mechanical Loading,” presented by Erica N.M. Jackson, candidate for the Doctor of Philosophy degree, and certify that in their opinion it is worthy of acceptance.

Supervisory Committee

Mark L. Johnson, Ph.D., Committee Chair
Department of Oral and Craniofacial Sciences

Mary P. Walker, Ph.D.
Department of Oral and Craniofacial Sciences

Erin Bumann, Ph.D.
Department of Oral and Craniofacial Sciences

Hari K. Bhat, Ph.D.
Department of Pharmacology

Gerald Wyckoff, Ph.D.
Department of Pharmacology

CONTENTS

ILLUSTRATIONS

Figure Page

TABLES

Table Page

ACKNOWLEDGEMENTS

I would like to express my sincere appreciation and special thanks to:

--Dr. Mark L. Johnson for his guidance and patience; for sharing his wealth of knowledge about the world of bone biology and allowing me to learn at my own pace.

--Dr. Mary P. Walker for her guidance, support, direction, supervision, management and organization.

--Drs. Erin Bumann, Hari K. Bhat and Gerald Wyckoff for their guidance and support.

--Dr. Nuria Lara-Castillo for her daily advice, patience in teaching techniques, protocol, etc., and constant support. Without your help, I would have been at a tremendous deficit.

--Drs. Ganesh Thiagarajan and Hamman Mumtaz for their engineering skills and aid in analysis of the biomechanical testing.

--Mark Dallas for his excellent assistance with micro-CT, 3-point bending, and osteomeasure.

--Yixia (Anita) Xie for her aid in preparing ulna, sectioning ulna/tibia, and staining.

--Dr. Donggao Zhao for processing and imaging the SEM specimens.

--Dr. Joanna Scott for her statistical analysis abilities.

--Dr. Mohammad Akhter for high-resolution micro-CT imaging.

--Alex Malko for analysis of micro-CT images.

--Dr. John Mullican for his patience and flexibility to accommodate a crazy schedule.

--Dr. Laura Stephenson and CAS at Washburn University for their aid

--support staff of SOD Research and Graduate Programs Office

--National Institute on Aging for providing grant support: PO1 AG039355 and 2PO1 AG039355-06

CHAPTER 1

INTRODUCTION

Bone has many functions in the body including acting as a structural support, aiding to provide movement in conjunction with skeletal muscles, protection of vital organs, providing a mineral (calcium and phosphorus) and energy (in the form of yellow marrow) storage depot, and serving as the site of hematopoiesis (in red marrow). The skeleton, despite its rather quiescent outward appearance, is a dynamic and ever changing organ. In contrast to all other organs, it is one that constantly goes through remodeling throughout the life span of an individual. This delicate balance is obtained through the antagonistic functions of two specialized bone cells: osteoblasts and osteoclasts. The osteoblast is a cuboidal-shaped cell that forms bone by secreting an organic matrix (osteoid) which is mineralized by the addition of calcium, phosphate and hydroxide (hydroxyapatite). Osteoblasts have a life span of a few weeks. The osteoclast is a large, multi-nucleated, tartrate resistant acid phosphatase (TRAP) positive cell that resorbs bone, aiding in bone maintenance and repair. The osteoclast has a lifespan of a few days. A third bone cell, the osteocyte, is a mature cell that acts to instruct certain osteoblastic and osteoclastic functions. The osteocyte is the most abundant bone cell (>90%) and is the longest lived, having a life span of decades (Bonewald 2011). The osteocyte cell body resides in a lacunar chamber which is completely surrounded by mineralized osteoid matrix and forms a highly interconnected network with other osteocytes, the vasculature and cells on the bone surface by sending dendritic processes through tiny bone channels, canaliculi. The osteocyte is postulated to be the mechanosensory cell in bone (Bonewald and Johnson 2008b; Lara-Castillo et al. 2015). Because of the anatomy of its location, the osteocyte is ideally situated in bone to sense mechanical load and translate that load into intracellular biochemical signals. The mechanosensory properties of the osteocyte and its subsequent actions in response signify a well-developed, specialized and specific process to manage its physiologic needs and adjust bone via multiple signaling cascades and endocrine secretions, both autocrine and paracrine.

Wnt/β-catenin Signaling Pathway in Bone

The skeleton has the capacity to adjust its mass and architecture in response to load. This ability is thought to be orchestrated by the osteocyte, which has long been postulated to be the mechanosensory cell in bone (Bonewald and Johnson 2008b; Lara-Castillo et al. 2015). Recently, *in vivo* and *in vitro* studies have begun to dissect the role of the osteocyte as a mechanosensory bone cell and the molecular signaling pathways involved in bone responsiveness to loading. Seventeen years ago, mutations in the human low-density lipoprotein receptor-related protein 5 (*LRP5)* were identified that caused either a low (Gong et al. 2001) or high bone (Boyden et al. 2002; Little et al. 2002) mass phenotype (G171V mutation). Coupled with the identification of Lrp5/6 as co-receptors for Wnt proteins (Pinson et al. 2000; Tamai et al. 2000; Wehrli et al. 2000; Boyden et al. 2002), the Wnt/β-catenin signaling pathway became a new research target for bone biology and the regulation of adult bone mass. As a result of these studies, an important regulatory protein of the Wnt/β-catenin pathway, sclerostin, a product of the *SOST* gene has emerged as a potential pharmaceutical target (Li et al. 2009).

At the cellular level, Wnt glycoproteins activate several signaling cascades, including the most commonly studied (“canonical”) pathway, which results in stabilization of the protein β-catenin (Clevers and Nusse 2012). In the absence of an upstream Wnt signal, β-catenin is sequestered in a degradation complex. The complex is held together by a scaffolding protein, Axin. β-catenin is phosphorylated by Glycogen Synthase Kinase-3β (GSK-3β), targeting β-catenin for ubiquitin-dependent proteolysis. The pathway is initiated when a Wnt protein binds to a co-receptor complex that includes a member of the Frizzled (FZ) family of seven-transmembrane receptors plus either Lrp5 or Lrp6 (Clevers and Nusse 2012), causing a phosphorylation cascade, involving the interaction of FZ with Dishevelled, leading to the phosphorylation of GSK-3β and inhibiting its phosphorylation of β-catenin. The receptor complex formation also results in the phosphorylation of the cytoplasmic tail of Lrp5/6, leading to the formation of a binding site for Axin (MacDonald et al. 2009). When Axin associates with the Lrp5/6 tail, the degradation complex holding β-catenin falls apart causing the release of β-catenin. Both of these events cause an increase in cytoplasmic β-catenin, which is then free to translocate into the nucleus with

Estrogen Receptor α (ERα). A key inhibitor of the Wnt/β-catenin pathway is the protein sclerostin, a product of the *SOST* gene, which inhibits the pathway by binding to Lrp5/6.

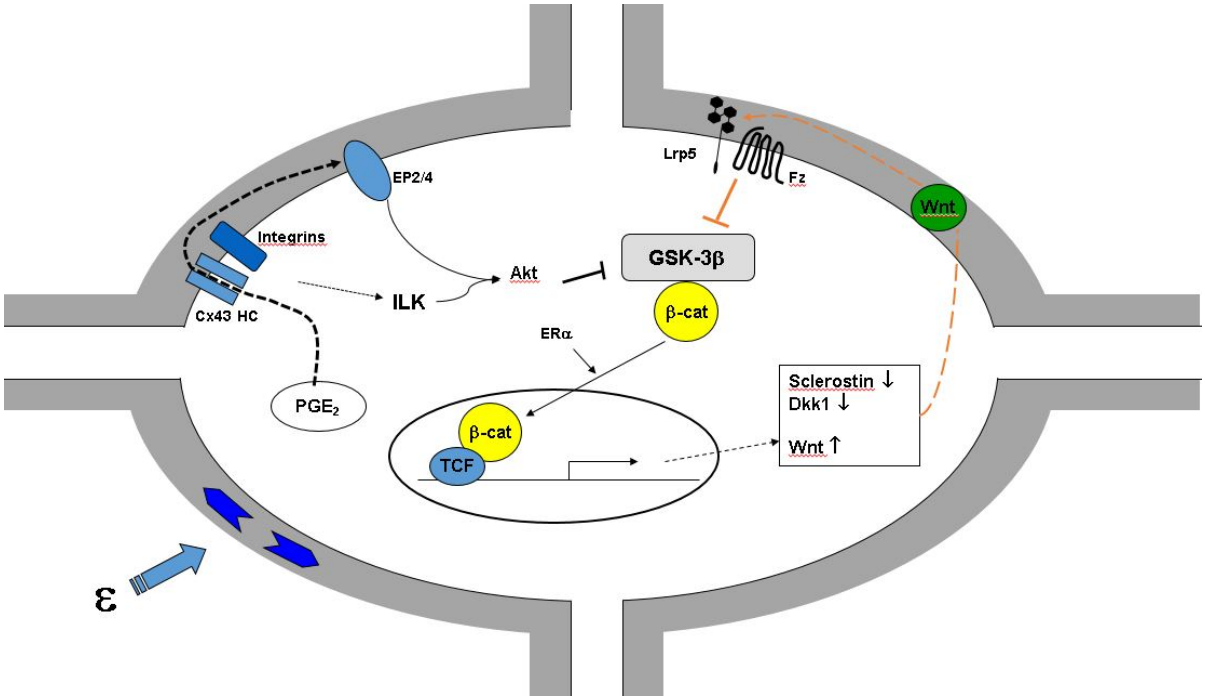

Figure 1. Wnt/β-catenin signaling pathway. Modified from (Bonewald and Johnson 2008a).

One mechanism for how osteocytes response to load, which includes the Wnt/β-catenin pathway has been proposed (fig. 1) (Bonewald and Johnson 2008a). When load is applied, it is hypothesized that fluid in the lacunar-canilicular system flows causing the release of prostaglandin E2 (PGE_2) out of connexin-43 hemi-channels (Cx43 HC). PGE_2 binds to its prostaglandin receptor (EP2/4) and causes Akt activation. Akt can phosphorylate GSK-3β and inhibit its activity independent of ligand binding to Lrp5/6. Inhibiting GSK-3β causes cytoplasmic β-catenin levels to rise and translocate into the nucleus, where it can alter transcription resulting in an increase of Wnt. Wnt can then permissively bind to Lrp5/6 and FZ and further activate and amplify the pathway.

Given the important role of the Wnt/β-catenin pathway in bone mass accrual and regulation, and the importance of estrogen in maintenance of the female skeleton, a few studies have examined the role of estrogen, estrogen receptors, and estrogen loss in regulating Wnt-β-catenin signaling in

bone. Recent studies investigated ovariectomy-induced bone loss in female mice treated with a *Sost* gene inhibitor (Artsi et al. 2014) or in mice with a deletion of the *Sost* gene (Li et al. 2008), showing that without the presence of sclerostin, the Wnt/β-catenin pathway is poorly regulated, leading to increases in almost all bone properties. It has been reported that osteocytes die via apoptosis following estrogen withdrawal (Tomkinson et al. 1997) and that ERα is important in trabecular bone formation in females (Kondoh et al. 2014) and males (Windahl et al. 2013a). These studies demonstrate the impact alterations in estrogen and its receptor can have on the osteocyte's ability to regulate its function in bone.

Many studies involving mouse models of altered Wnt/β-catenin signaling have reported differences between males and females, including gender differences in trabecular bone properties of $LRP5^{G171V}$ transgenic high bone mass (HBM) (Dubrow et al. 2007). Major gender differences have also been reported in bone strength and mass in *SOST* knockout mice (Javaheri 2012) and in mice with a deletion of a single allele of β-catenin in osteocytes (Javaheri et al. 2014). These studies illustrate alterations to bone properties following changes to players in the Wnt/β-catenin pathway. Along with the estrogen studies mention previously, these suggest the potential for hormonal differences, specifically in regards to estrogen, in the regulation of the Wnt/β-catenin pathway.

Osteoporosis

Osteoporosis is a significant health concern, which currently afflicts 10.2 million Americans, while another 43.4 million have low-density bone mass (Looker et al. 2017). Osteoporosis is a generalized skeletal disorder of low bone mass (thinning of bone) and deterioration in its architecture, causing susceptibility to fracture and is defined as bone mineral density of ≥2.5 standard deviations below the average mean peak bone mass (average young, healthy adults of the same gender) (World Health Organization 1994). By 2025, osteoporosis will cause approximately 3 million fractures and cost $25.3 billion annually (National Osteoporosis Foundation). The underlying cause osteoporosis is an imbalance in bone formation and resorption. Typically, through childhood, adolescence and adult life, there is a predilection towards osteoblast function, meaning an increase in bone volume and density, until an equilibrium is reached post-pubescent. During adulthood, bone mass is maintained through a

balanced equilibrium of osteoblast and osteoclast function to re-model and overturn bone. However, as individuals age, the osteoclast activities can become more prevalent and cause a loss of bone density. Osteoporosis can arise from an improper formation of bone during development leading to an insufficient peak bone mass in adulthood, excessive bone resorption, or an inadequate formation of new bone during remodeling (Raisz 2005).

There are three types of osteoporosis: primary type 1, primary type 2, and secondary. Primary type 1 affects post-menopausal women and is the most prevalent type among all women (World Health Organization 1994). Primary type 2 arises after the age of 75 and is seen in both men and women with a 2:1 ratio, respectively (World Health Organization 1994). Secondary osteoporosis can occur at any age from a variety of reasons such as the persistent use of glucocorticoids (World Health Organization 1994). The chance for osteoporotic fractures increases as one approaches geriatric ages, and the fractures themselves, along with osteoporosis rates, affect women more than men, with ~80% of fractures occurring in women. This is even more magnified in post-menopausal women who experience dramatic and rapid bone loss due to the decline of estrogen in the body.

Almost 80 years ago, it was first postulated that it was the loss of estrogen during and surrounding menopausal years that caused the associated bone loss and osteoporosis (Albright et al. 1941). Women show a dramatic loss of bone, specifically trabecular bone, within the first ten years post-menopausal, and a noteworthy, but less pronounced loss of cortical bone during the same time period; whereas men exhibit a gradual, slow loss of both bone types (Riggs and Melton 1986). It is established that estrogen deficiency in women leads to alterations of bone architecture, increased skeletal fragility and bone loss. A seminal peri-menopausal study by Recker and colleagues demonstrated that rapid bone loss begins as early as 2 years prior to the last menses (2000). Post-menopausal bone loss is thought to occur through bone direct (via osteoclast stimulation and osteoblast suppression) and indirect effects (via secondary hyperparathyroidism) on bone (Riggs et al. 2002).

Estrogen

Estrogen is a gonadal steroid hormone derived from cholesterol and is preferentially synthesized in the gonads (ovary/testis), specifically from thecal cells of developing follicles, but can be

produced in small amounts by conversion of dehydroepiandrosterone (DHEA) from the zona reticularis of the adrenal gland. The name estrogen is derived from the Greek “oistros” figuratively meaning “sexual passion or desire” and the suffix “-gen” meaning “producer of”. Estrogen is the primary female sex hormone responsible for producing secondary female sex characteristics, aiding in regulation of menses, and is known to diminish during menopause and remain at sub-active threshold levels.

Three forms of estrogen are active in post-menarche, pre-menopausal women. Of these, estradiol (17β-estradiol, E2) is the most biologically active, even though it is present in the blood serum in small quantities, 15-350 pg/mL, with levels fluctuating during a normal female menstrual cycle. During menopause, a preferential switch to estrone occurs. Estriol is only seen in pregnant women. The estrogen synthesis pathway is in figure 2.

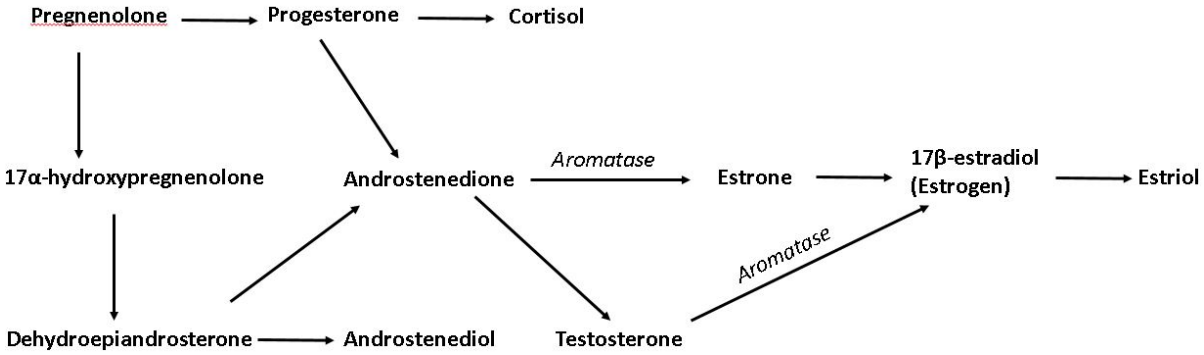

Figure 2. Estrogen synthesis pathway. Modified from (Ascenzi et al. 2006).

Because estrogen is a steroid hormone, it can easily cross the phospholipid bilayer of cell plasma membranes and enter the cell, where it can interact with its receptor in one of three locations: intracellular/cytoplasmic (which is traditionally associated to the Wnt/β-catenin pathway), nuclear-resident, or membrane-associated. Two isoforms of intracellular estrogen receptors (ER) exist: ERα and ERβ, products of two separate genes, *ESR1* and *ESR2*, respectively. Both belong to the steroid/thyroid hormone superfamily of nuclear receptors and share a common structural architecture (Evans 1988; Giguere et al. 1988). The receptor is composed of three distinct but interacting domains: the AF-1 domain at the N terminus, the DNA-binding domain containing zinc fingers, and the AF-2 or ligand-binding domain at the C terminus (fig. 3). Ligand binding to ER causes a conformational change

in the receptor, leading to a number of events, including receptor dimerization and binding to estrogen response element (ERE) in the DNA, causing transcriptional changes.

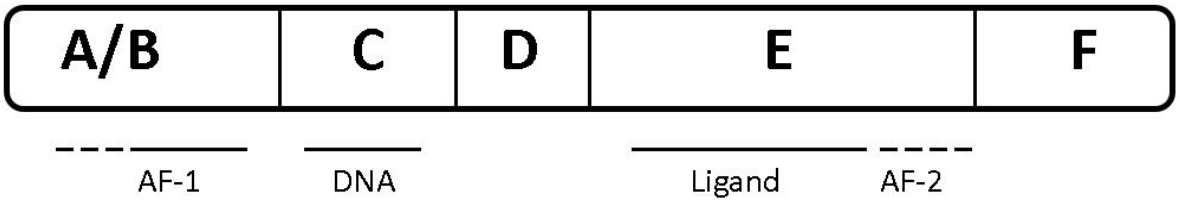

Figure 3. Structural domains of the estrogen receptor. Modified from (Nilsson et al. 2001).

It is known that ERα is critical for β-catenin nuclear translocation following activation of the Wnt/β-catenin signaling pathway (Recker et al. 2000), but this may not require estrogen (Windahl et al. 2013b). A recent study has shown that bone cell's response to load and estrogen both involve ERα, but only estrogen regulates ERα's cellular concentration (Zaman et al. 2006). This suggests that the bone loss associated with estrogen deficiency is a consequence of the reduction of ERα number/activity that is associated with low estrogen concentration.

Estrogen can also act through non-genomic mechanisms, which may then subsequently alter the osteocyte's function, e.g. possibly through Akt or other signaling pathways. These non-genomic actions may be completed in one of two ways: through membrane-bound ER, or through estrogen binding to other receptors. Membrane-bound ER can activate cytoplasmic kinases which can induce phosphorylation of transcription factors or substrate proteins and are associated to caveolae/lipid rafts that can activate non-nuclear signaling termed rapid/non-genomic/membrane initiated steroid signaling (MISS) (Mendelsohn and Karas 2010). Non-genomic estrogen effects have been reported through binding to G-protein coupled receptor 30 (GPR30) on the endoplasmic reticulum, causing a release of intracellular calcium (Revankar et al. 2005). The same paper reported phosphoinositide 3-kinase (PI3K) generation through estrogen GPR30 and Epidermal Growth Factor Receptor (EGFR) activation, not activation of ER. PI3K leads to membrane localization of phosphatidylinositol 3,4,5-trisphosphate (PIP3), which recruits Akt to the membrane. The caveolar protein activation of membrane-bound ER can also activate PI3K and PIP3. This is a consideration since there is crosstalk between Akt and

Wnt/β-catenin pathway, specifically for the initial pathway activation in response to loading (Bonivtch et al. 2007b). Other studies have indicated non-nuclear signaling in OVX mice treated with estradiol and estrogen-dendrimer conjugate (EDC), an estradiol derivative that cannot enter the nucleus. OVX mice treated with EDC prevented cortical bone loss, attenuated the loss of bone strength and prevented the OVX-induced increase in osteoclastogenesis and osteoblastogenesis. (Bartell et al. 2013). All of these findings show the importance of estrogen in overall cellular function and the potential impact estrogen loss has on that function.

Estrogen is not the only agent capable of binding to and activating estrogen receptors. Selective Estrogen-Receptor Modulators (SERMs) lack the chemical steroidal structure of estrogen, but possess a tertiary group, allowing them to bind to the estrogen receptor. SERMs exert specifically agonistic or antagonistic effects, depending upon target tissue. While many SERMs are available clinically, only one, Raloxifene, is recommended for the treatment and prevention of osteoporosis (Morello et al. 2002), specifically spinal osteoporosis. Despite their potentially beneficial uses in the treatment of many diseases, the associated risks with SERMs (increased risk of thromboembolism, stroke, and uterine cancer) could hinder their use in certain populations of patients. Finding a SERM that is useful for strictly osteoporosis but without negative side effects in other tissue is an on-going area of research (Gennari et al. 2007).

Statement of Purpose

As the population continues to age, numerous physiologic changes occur that may lead to detrimental effects on an individual's health and quality of life. An aging skeleton does not respond to load as effectively as a young skeleton, especially in post-menopausal women. This leads to challenged skeletal integrity due to an imbalance in bone generating and resorbing processes. These studies provide understandings of how estrogen, or more importantly the lack of estrogen, regulates the Wnt/β-catenin pathway in osteocyte cell signaling, which in turn could begin to foster better potential treatments for osteoporosis.

Central Hypothesis and Specific Aims

The hypothesis of this dissertation is that estrogen is a critical factor in the responsiveness of the osteocyte to mechanical loading via regulation of the Wnt/β-catenin pathway; and in the absence of estrogen, osteocytes will have a decreased activation upon mechanical loading. The hypothesis was addressed through the following specific aims:

Specific Aim 1: Determine the effects of ovariectomy on the ability of the osteocyte to activate the Wnt/β-catenin pathway in response to mechanical loading.

Rationale: Rapid bone loss occurs at menopause coinciding with the loss of estrogen. The Wnt/β-catenin pathway is known to be activated by mechanical loading. While both of these phenomena are well established, this estrogen deprivation induced attenuation of signaling through this pathway has never been investigated as a possible mechanism for the decline of bone properties during the peri-menopausal and post-menopausal years. These *in vivo* studies will determine whether the lack of estrogen changes the intrinsic ability of osteocytes to respond to load or whether estrogen loss results in architectural changes in the lacunar-canalicular system, which subsequently affects the ability of the osteocyte to transmit the load signal and activate β-catenin signaling.

Specific Aim 2: Determine the role and relative importance of estrogen on the activation of the Wnt/β-catenin pathway *in vitro* in response to mechanical load.

Rationale: Estrogen is among many steroidal gonadal hormones produce by females; however, during post-menopausal years, the amount declines, while other sex steroid hormone levels, testosterone and progesterone, do not fluctuate or deteriorate as severely. These *in vitro* studies will elucidate the role estrogen plays in the activation of the Wnt/β-catenin pathway in response to mechanical loading in osteocytes.

Chapter 2

METHODS AND MATERIALS

In Vivo Mouse Model

Forearm Loading and Tissue Harvesting

Female TOPGAL (wild-type) mice (CD-1 background)[1] (n=20) were utilized for this study. These mice carry a β-catenin reporter transgene comprised of the *lacZ* gene encoding β-galactosidase under the control of the TCF/LEF β-catenin promoter (DasGupta and Fuchs 1999). Staining for β-galactosidase provides a visual register of cells that have activated the Wnt/β-catenin pathway. At 16 weeks of age, mice underwent an ovariectomy (OVX) (n=10) surgery or a sham (n=10) surgery. Four weeks post-surgery, a single session of mechanical loading on the right forearm was performed using a loading device[2]. The loading used a global strain of 2200 microstrain (με) for 100 cycles at 2 Hz. The left forearm of each animal serves as a control, non-loaded arm. During the loading, mice were anesthetized with 3.5% isoflurane[3]. Mice were sacrificed at 1 hour or 24 hours post-load. Twenty-four hours post-load has been shown to represent peak activation of the Wnt/β-catenin pathway (Bonewald and Johnson 2008b; Lara-Castillo et al. 2015). Five mice per treatment group were sacrificed per time-point, for a total of 20 mice. All animal procedures are approved by UMKC IACUC protocol #1129.

At sacrifice, each animal was weighed and the ulnae, tibiae, femurs and uterus were removed. The uterus was weighed and fixed in 4% paraformaldehyde (PFA). Loaded (right) and non-loaded (left) ulnae were stained for β-galactosidase to assess the TOPGAL gene activation. The right femur was wrapped in phosphate buffered saline (PBS) soaked gauze and stored at -20°C and used for micro-computed tomography (micro-CT) (for a 3-dimensional reconstruction of cortical and cancellous bone) and biomechanical testing. The right tibia was fixed in 4% PFA, embedded in plastic, and utilized for numerous tests, including histology to determine osteoclast number and surface and osteoblast number by TRAP staining and VonKossa-Tetrachrome staining, respectively. The right tibia was also used for

[1] Jackson Laboratories, 600 Main Street, Bar Harbor, ME 04609
[2] Bose ElectroForce 3220, Medical Device Testing Services, 5929 Baker Road, Suite 430, Minnetonka, MN 55345
[3] Cat. No. 07-893-2375, Patterson Veterinary, 822 7th Street, Greely, CO 80631

backscatter scanning electron microscopy (SEM) and high-resolution Xradia microXCT scanning. Both of these technologies allow for visualization of the osteocyte lacunae on a 2- and 3-dimensional level and give evidence of any changes in the micro-architecture of the bone, as a result of estrogen loss. A summary table of tissues harvested, their experimental use, processing and data collected is in table 1.

TABLE 1

SUMMARY OF TISSUE UTILIZATION FOLLOWING SACRIFICE

Tissues Harvested	**Experimental Use**	**Processing**	**Data Collected**
RT Ulnae (loaded) LT Ulnae (non-loaded)	β-galactosidase staining for osteocyte activation	PFA fixed and Embedded in Paraffin	Activation of β–catenin signaling in osteocytes
Femur	Micro-CT 3-point bending	Wrapped in PBS soaked gauze at stored at -20 ^{o}C	Standard Micro-CT measures per ASBMR recs (Parfitt et al. 1987) and Biomechanical Properties
Tibiae	-TRAP staining -VonKossa staining -Backscatter SEM -Xradia microXCT	PFA fixed and Plastic Embedded	-Osteoclast parameters -Osteoblast parameters -Lacunar volume and area -Lacunar number, density, volume
Uterus	Weight (to confirm OVX)	Weigh and PFA fix	Effect of OVX on uterine weight

β-Galactosidase Staining

Following sacrifice, the loaded (right) and non-loaded (left) forearms were dissected by cutting the humerus at mid-shaft and removing the skin/muscle from the bone, while keeping the periosteum intact. Skin/muscle were removed from the forearms, cutting at the wrist radius/ulna joint. Whole bone β-galactosidase staining was performed using freshly prepared ice cold 4% PFA from Alfa Aesar[4] (16% w/v aqueous solution, methanol free). Stock PFA was diluted with 10X PBS[5] (pH 7.4) for a final concentration of 4% PFA in 1X PBS. 0.2M solutions of $K_3Fe(CN)_6$[6] and $K_4Fe(CN)_6 \cdot 3H_20$[7] (K3 and K4

[4] Cat. No. 43688, Alfa Aesar, 2 Radcliff Road, Tewksbury, MA 01876
[5] Cat. No. AM9625, Fischer Scientific, Life Technologies, Ambion Inc., Invitrogen™, 5781 Van Allen Way, Carlsbad, CA 92008
[6] Cat. No. P8131, Sigma-Aldrich, 3050 Spruce Street, St. Louis, MO 63103
[7] Cat. No. P9387, IBID

solutions, respectively) were made fresh each time. The X-Gal buffer (1ml of 1 M $MgCl_2$[8], 100 µl of NP-40 substitute[9] and 0.05 gm of sodium deoxycholic acid[10] and brought to 500 ml final volume with Direct-Q deionized water was pre-made and stored for several months at room temperature. The X-Gal powder[11] was placed into solution at 40mg/ml in DMF[12], creating X-Gal solution and was made fresh each time. The Staining Buffer was made fresh each time and contained 19 ml of X-Gal buffer, 0.5 ml each of 0.2 M K3 and K4 solutions, 200 µl of 1M Tris-HCl[13] (pH 8.0) and 0.5 ml of X-Gal solution.

Prior to staining, forearms were fixed in ice cold 4% PFA for a minimum of 60 minutes but no longer than 90 minutes on ice with gentle rocking, followed by 3 washes with 1X PBS for 5 minutes. Individual forearms were placed in X-Gal staining solution (12 ml in 15 ml tubes) and left in the dark for 36-40 hr at 32°C without shaking. Staining progress was checked routinely until adequate color had developed (30-36 hours).

Following staining, forearms were washed 3 times in 1X PBS, for 5 minutes each wash and then post-fixed in 4% PFA (as above) overnight at 4°C, then washed 3 times in 1X PBS and placed in 15 ml of Immunocal[14] until bone decalcification (up to 3 days with changes into fresh Immunocal each day). After decalcification, bones were washed several times (minimum 5 times) in deionized water and stored in 70% ethanol until paraffin processing and embedding (usually 1-2 days). Prior to paraffin embedding, processing was performed[15] with the following steps and times: graded ethanol (70%, 80%, 95% twice) for 1 hour each; 100% ethanol-glycerol (95 ml 100% ethanol + 5 ml glycerol) twice for 2 hours each; three times in Xylene for 1 hour each; twice in paraffin for 1 hour each followed by two more paraffin steps for 90 minutes each. Bones were then placed in paraffin blocks[16] for sectioning.

[8] Cat. No. AM9530G, Fischer Scientific, Life Technologies, Ambion Inc., Invitrogen™, , 5781 Van Allen Way, Carlsbad, CA 92008
[9] Cat. No. 74385, Fisher Scientific, Fluka™, 300 Industry Drive, Pittsburgh, PA 15275
[10] Cat. No. D6750-10G, IBID
[11] Cat. No. 15520-018, Fisher Scientific, Invitrogen™, , 5781 Van Allen Way, Carlsbad, CA 92008
[12] Cat. No. D4551-250ML, IBID
[13] Cat. No. 22638, USB Corporation, 26111 Miles Road, Cleveland, OH 44128
[14] Product No. 1414, Decal Chemical Corporation, Po Box 916, Tallman, NY 10982
[15] Tissue-Tek®VIP®, Sakura Finetek, USA, Inc., 1750 West 214th Street, Torrance, CA 90501
[16] Microm 350-1, ThermoFischer Scientific, 168 3rd Avenue, Waltham, MA 02451

Starting at the olecranon, 10 micron thick sections were sliced[17] and sections taken over a 2mm region that was ±1mm of the mid-shaft of the ulna. A minimum of 16 sections per animal were analyzed.

Immunohistochemistry

Four sections of forearm were collected on SuperFrost positive charged slides[18] and allowed to dry. Removal of the paraffin was accomplished by sequential dips in xylene and rehydrated through graded washes of water and ethanol and finally 1X PBS. Sections were incubated overnight at 4°C in blocking solution (2.5% Bovine Serum Albumin (BSA)[19], 1% donkey serum[20] in 1X PBS). The next day, 3 sections/slide were incubated with primary antibody against Sclerostin[21] (1:100 dilution in blocking solution) and 1 section/slide was incubated with isotype matched non-immune IgG[22] (1:500 dilution in blocking solution), as a negative control. Incubation was allowed for 4 hours at room temperature, followed by 3 washes with 1X PBS for 5 minutes each, with shaking in a Coplin jar. A total of 4 slides/animal were stained. Sections were then incubated for 1 hour at room temperature (covered with foil or in a drawer or dark room) with Cy3 conjugated donkey anti-goat secondary antibody[23] (1:200 dilution in blocking solution) and DAPI[24] (1:250 dilution in blocking solution). Sections then washed 4 times (10 minutes each) with 1X PBS in Coplin jars with gentle shaking. Glass cover-slips[25] are added with 9:1 glycerol:PBS with n-propyl gallate[26], avoiding bubbles. Isotype matched non-immune IgG are used at negative control for all immunostaining. Sections were stored at 4°C until quantification.

[17] Leica RM2125, Leica Biosystems Inc., 1700 Leider Lane, Buffalo Grove, IL 60089
[18] Cat. No. 6776214, Fisher Scientific, 300 Industry Drive, Pittsburgh, PA 15275
[19] Cat. No. 9048-46-8, Research Products International Corporation, 410 North Business Center Drive, Mt. Prospect, IL 66056
[20] Cat. No. D9663, Sigma-Aldrich, 3050 Spruce Street, St. Louis, MO 63103
[21] Cat. No. AF1589, R&D Systems, 614 McKinley Place NE, Minneapolis, MN 55413
[22] Cat. No. AB-108-C, IBID
[23] Cat. No. 705-165-147, Jackson ImmunoResearch Laboratories, Inc., 872 West Baltimore Pike, West Grove, PA 19390
[24] Cat. No. D9542-5MG, Sigma-Aldrich, 3050 Spruce Street, St. Louis, MO 63103
[25] Cat. No. 94-2450-10, Premiere®, Gorilla Scientific, 14689 Lee Highway #797, Gainesville, VA 20156
[26] Cat. No. P3130, Sigma-Aldrich, 3050 Spruce Street, St. Louis, MO 63103

TOPGAL β-catenin Quantification

Sections were imaged with a light microscope[27] equipped with a high-resolution digital camera[28] at 20X objective for both bright field and fluorescent microscopy. Bright field images were exposed for 20ms, while Sclerostin and DAPI fluorescent images were exposed for ranges of 2000-6000ms (5000ms most often) and 20-100ms (100ms most often). Images were analyzed (above and below the medullary cavity) using a MatLab program that allows for easy and quick quantification of total, sclerostin positive and β-galactosidase positive osteocyte cell numbers. A secondary confirmation of these numbers was performed manually using ImageJ and Microsoft Photo Viewer.

Micro-CT

Following harvesting, femurs were cleaned of excess tissue, wrapped in PBS soaked gauze and stored at -20°C. For scanning, bones were placed in 15 ml Eppendorf plastic tubes[29] filled with PBS and sponge foam to prevent movement during scanning. Tubes were mounted vertically with the cap being secured to the scanning stage using dental wax.

Individual right femurs were imaged using a micro-CT scanner[30] using a 0.5mm aluminum filter, 9.6 μm scanning size, 0.4 rotation step, frame average of 1, 800μA current and 50kV voltage. Standard micro-CT measures were taken per ASBMR recs (Parfitt et al. 1987). Reconstruction was carried out with a modified Feldkemp2 algorithm using SkyScan™ NRecon software. Gaussian smoothing, ring artifact reduction and beam hardening correction were applied. Global thresholds were selected by visual matching with greyscale image and the same global threshold values were applied to all femur samples. The threshold levels for cortical bone were from 55 to 255, and threshold levels for trabecular bone were from 47 to 255.

Trabecular data was collected at 1mm region (100 slices) of secondary spongiosa of distal femur proximal to the growth plate and cortical data collected at 0.5mm region (50 slides) distal to the 3rd trochanter (fig. 4). 3D and 2D morphometric parameters were calculated for trabecular and cortical

[27] Nikon Eclipse E800, Nikon Instruments, Inc., 1300 Walt Whitman Road, Melville, NY 11747
[28] Nikon Eclipse DXM 1200, IBID
[29] Cat. No. C15R, MidSci, 280 Vance Road, St. Louis, MO 63088
[30] Bruker Skyscan 1174, 40 Manning Road, Billerica, MA 01821-3915

bone selected regions of interest using CT Analysis Software. Surface rendering 3D models of trabecular and cortical bone were constructed using CT Vox software.

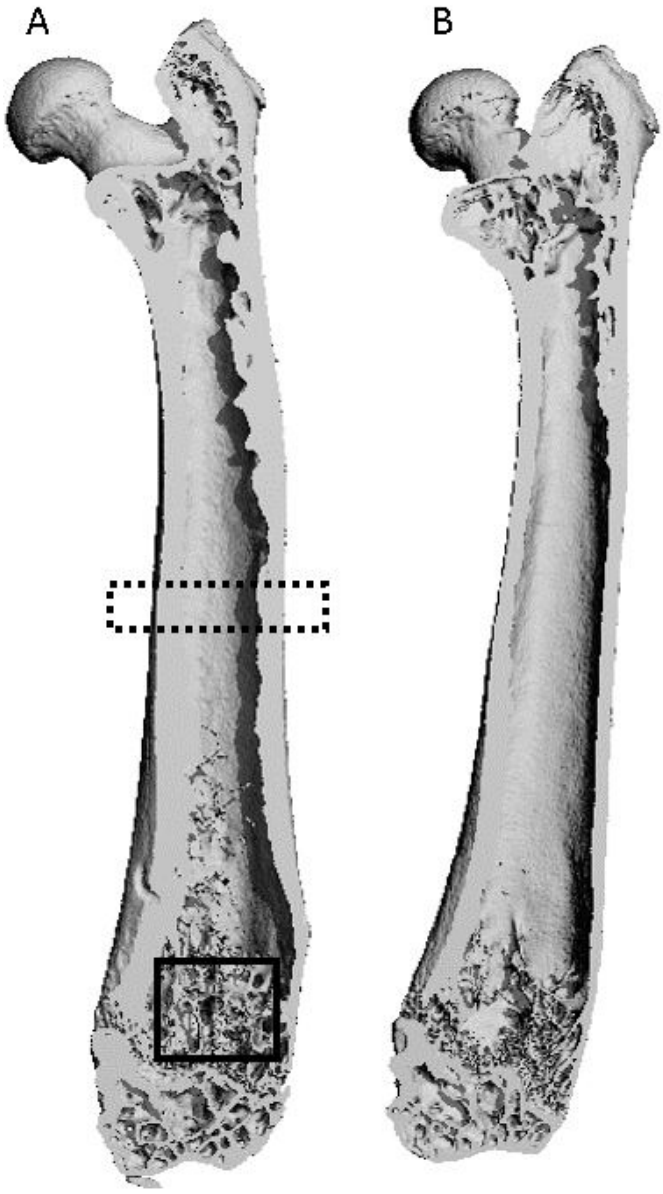

Figure 4. Reconstructed femur regions of interest (ROI) for micro-CT. Dashed box denotes cortical ROI. Solid box denotes trabecular ROI A = Sham; B = OVX.

Three-dimensional analysis was preformed to determine cortical bone volume/total volume (BV/TV), thickness, periosteal, endosteal and total perimeter; trabecular BV/TV, separation, number and thickness; and bone mineral densities (BMD) (cortical and trabecular) (comparison to hydroxyapatite standard), along with creating a 3-dimentional structural picture of the overall bone quality.

Biomechanical Testing

Following Micro-CT analysis, right femurs were utilized for three-point bending to failure tests[31] to characterize biomechanical properties. Femurs were kept at -20°C in PBS soaked gauze until testing. Prior to testing, the samples were allowed to thaw to room temperature, and kept hydrated during testing. Femurs were oriented in the anterior/posterior direction *in vivo*, with a crosshead span of 8.8mm and the bone centered on the fixture so right and left side overhang was approximately equal. Crosshead displacement of 0.1 mm/sec was used, with a -0.5N load preset. Pre-test measurements of span (distance between props holding the bone), bone length, right and left overhang (distance of bone past props), minimum and maximum caliper distance at mid-shaft and femur weight were recorded. Post-test measurements of left and right fracture location were also taken. From the 3-pt bending tests, stiffness, ultimate force, moment of inertia, work to failure and Young's Modulus was calculated using realigned micro-CT scans and the BoneJ plug-in for ImageJ.

Plastic Embedding Tibiae

Following harvest, right tibiae were fixed in 4% PFA (as previously described) overnight at 4°C. After 24 hours, bones were switched into 70% ethanol and remained at 4°C until plastic embedding. Tibiae were dehydrated[32], followed by a five-day infiltration process with infiltration solution and acetone[33]. Infiltration solution consists of 84% methylmethacrylate (MMA)[34], 14% Dibutyl phthalate[35],

[31] Bose ElectroForce 3230, Medical Device Testing Services, 5929 Baker Road, Suite 430, Minnetonka, MN 55345
[32] Tissue-Tek®VIP®, Sakura Finetek, USA, Inc., 1750 West 214th Street, Torrance, CA 90501
[33] Cat. No. A18-P-4, Fisher Scientific, 300 Industry Drive, Pittsburgh, PA 15275
[34] Cat. No. M55909, Sigma-Aldrich, 3050 Spruce Street, St. Louis, MO 63103
[35] Cat. No. 524980, IBID

1% PEG400[36] and 1% benzoyl peroxide (BPO)[37]. Specimens were put in 20 ml glass vials, with shaking over the 5 day period. The five day infiltration procedure is: day 1 = 8 ml acetone; day 2 = 1:1 acetone/infiltration solution; day 3 = 1:2 acetone/infiltration solution; day 4 and 5 = infiltration solution. A 20 ml glass vial (one for each specimen) with 8 ml of pre-polymerized embedding solution in the bottom (same as infiltration solution with addition of 0.33% N,N-dimethyl p-toludine (DMT)[38] was prepared on the first day of infiltration and polymerized in -20°C. One day before embedding, the pre-polymerized vial was brought to 4°C. 10 ml of embedding solution was added to each vial, specimens were transferred to each vial and oriented, and vials were then stored at -20°C for 3-5 days for full polymerization.

Sectioning Tibiae

Plastic blocks were trimmed with a water-cooled diamond saw[39]. Specimens were mounted on a microtome[40], oriented vertically, and trimmed, until reaching the desired area of interest, approximately mid-way through bone. While cutting, specimen cut face kept wet with cutting solution (70% ethanol, distilled water, and soap). At area of interest, 5 µm thick sections were gathered and mounted to slides[41] (2 sections/slide) coated with gelatin[42], glycerol[43] and distilled water. Specimens were covered with plastic film, rolled flat, then stacked together, clamped and allowed to incubate at 55°C for 1 day. 6 sham and 6 OVX animals were analyzed. A minimum of 15 slides were collected, with 3 slides being used for VonKossa-Tetrachrome staining and another 3 being used for TRAP staining.

[36] Cat. No. 25322-68-3, EMD Millipore Corporation, 290 Concord Road, Billerica, MA 01821
[37] Cat. No. 179981, Sigma-Aldrich, 3050 Spruce Street, St. Louis, MO 63103
[38] Cat. No. D189006, IBID
[39] IsoMet® 1000, Precision Saw, Buehler Limited, 41 Waukegan Road, Lake Bluff, IL 60044
[40] HM 355S Automatic Mictotome, Thermo Scientific, 3747 North Meridian Road, Rockford, IL 61101
[41] Cat. No. 6776214, Fisher Scientific, 300 Industry Drive, Pittsburgh, PA 15275
[42] Cat. No. G7041, Sigma-Aldrich, 3050 Spruce Street, St. Louis, MO 63103
[43] Cat. No. GX0185-6, EMD Millipore Corporation, 290 Concord Road, Billerica, MA 01821

VonKossa and TRAP Staining

VonKossa staining was utilized for visualization of osteoblasts on the bone trabecular surface. A total of 4 solutions were utilized for staining. Slides were stained with solution 1 (5% silver nitrate[44] in distilled water) for 15 minutes in the dark, followed by 4, 1 minute distilled water rinses. Staining with solution 2 (5% sodium carbonate[45], 25% formaldehyde[46] in distilled water) was for 2 minutes (time sensitive), then 4, 1 minute distilled water rinses. Solution 3 consists of 2 separate solutions that must be combined: solution 3a = 10% sodium thiosulfate[47] in distilled water; solution 3b= 10% potassium ferricyanide[48] in distilled water. Solutions were combined (50 ml 3a + 2.5 ml 3b) just before using and slides were stained for 20 seconds followed by rinsing for 20 minutes under running tap water. Slides were then stained with solution 4 (3% tetrachrome[49] in distilled water, or MacNeal's tetrachrome[50]), followed by 3, 1 minutes distilled water rinses. Slides were sequentially dehydrated with: 70% ethanol (1 minute), 95% ethanol (1 minute), 100% ethanol (1 minute, 3 times); followed by xylene for 2 minutes, 3 times. Slides were covered with glass coverslips[51] and sealed with Permount[52].

TRAP staining was utilized for visualization of osteoclasts (multi-nucleated, TRAP positive cells) on bone trabecular surfaces. Fifty ml of buffer I (0.92% sodium acetate anhydrous[53], 2.3% 100mM L-(+) Tartaric Acid [sodium tartrate dibasic dehydrate][54], 0.28% glacial acetic acid[55], and 95% distilled water) was heated for 20 minutes at 37°C. Next, 100 µl of buffer II (2% naphthol AS-BI phosphate[56] in ethylene glycol monoethyl ether[57]) was added to heated buffer I, followed by submersion of the slides. Slides were then incubated at 37°C for 45 minutes. Another 50 ml of buffer I was prepared at room

[44] Cat. No. S6506, Sigma-Aldrich, 3050 Spruce Street, St. Louis, MO 63103
[45] Cat. No. S263-500, Fisher Scientific, 300 Industry Drive, Pittsburgh, PA 15275
[46] Cat. No. F79-500, IBID
[47] Cat. No. S446-500, IBID
[48] Cat. No. P232-500, IBID
[49] Cat. No. 02783-5, Polysciences Inc., 400 Valley Road, Warrington, PA 18976
[50] Cat. No. S-MNTI, DHM Inc., 135 Home Avenue, Villa Park, IL 60181
[51] Cat. No. 22X50-1.5, Fisher Scientific, 300 Industry Drive, Pittsburgh, PA 15275
[52] Cat. No. SP15, IBID
[53] Cat. No. S210-500, IBID
[54] Cat. No. T-6521, Sigma-Aldrich, 3050 Spruce Street, St. Louis, MO 63103
[55] Cat. No. A6283, IBID
[56] Cat. No. N-2125, IBID
[57] Cat. No. E-2632, IBID

temperature. One ml of buffer III (4% sodium nitrate[58] in distilled water) and 1 ml of buffer IV (5% pararosaniline chloride [basic fuchsine][59] in distilled water and HCl[60]) were mixed for 30 sec and allowed to sit for 2 minutes before adding to the room temperature buffer II. After slide incubation (previous steps), slides were transferred to room temperature buffer II for 10 minutes or until color developed. Slides were then washed with distilled water and a counter stain of methyl green[61] was added for 30 min at 37°C. Following counterstaining, slides were rinsed 3 times for 30 sec each in distilled water. Slides were then sequentially dehydrated with: 95% ethanol (30 seconds, 2 changes), 100% ethanol (30 seconds, 1 change), 100% ethanol (1 minute, 2 changes), then xylene (1 minute, 3 changes). Slides then cover slipped[62] as above and sealed with Permount[63].

All histological sections were analyzed with a light microscope[64] at 20X objective and Osteomeasure Software[65]. Six adjacent fields (2 rows of 3, each field = 500 μm^2) were counted 150 μm below the proximal growth plate, to avoid primary spongiosa. Measurements obtained were osteoblast/clast number, number of osteoblast/clast to bone perimeter, and osteoblast/clast surface to bone surface.

Backscatter Scanning Electron Microscopy

Following the sectioning of the right tibiae, 3 animals from each group (Sham and OVX), were utilized for backscatter scanning electron microscopy to analyze lacunar area. Specimens were coated with Au-Pd alloy[66] for 60 seconds. Images were acquired at high vacuum mode[67]. Experimental conditions were accelerating voltage = 15 kV, spot size = 4, working distance = 15 mm, and magnifications of 40X (for reference images) or 300X (for analysis images). Analysis images were taken

[58] Cat. No. S-2252, Sigma-Aldrich, 3050 Spruce Street, St. Louis, MO 63103
[59] Cat. No. P-3750, IBID
[60] Cat. No. 7647-01-0, Acros Organics, Thermo Scientific, 500 American Road, Morris Plains, NJ 07950
[61] Cat. No. 198080, Sigma-Aldrich, 3050 Spruce Street, St. Louis, MO 63103
[62] Cat. No. 22X50-1.5, Fisher Scientific, 300 Industry Drive, Pittsburgh, PA 15275
[63] Cat. No. SP15, IBID
[64] Nikon Eclipse E800, Nikon Instruments, Inc., 1300 Walt Whitman Road, Melville, NY 11747
[65] Osteometrics, Inc., 1240 Clairmont Road Suite 100, Decatur, GA 30030
[66] Leica EM SCD050, Leica Biosystems Inc., 1700 Leider Lane, Buffalo Grove, IL 60089
[67] Phillips XL30-ESEM-FEG, FEI Company, 5350 Northeast Dawson Creek Drive, Hillsboro, Oregon 97124

1 mm proximal to the end of the medullary cavity, 3 images anterior and 3 images posterior. Images were then de-identified for lacunar size analysis via ImageJ, with particle size 10-250 μm^2, excluding lacunae on edges of images, but including holes. Total lacunae areas were averaged per bone, along with the top 20% largest lacunae per bone.

High-Resolution MicroXCT

The 4 Sham and 4 OVX plastic embedded right tibiae that were not utilized for histological sectioning, were utilized for high-resolution microXCT (Xradia)[68], courtesy of Dr. Mohammad Akhter at Creighton University. Specimens were cut into 300 μm thick sections with a water-cooled diamond saw[69], 3 mm proximal to the tibia-fibula joint. Measurements were taken on the medial and lateral side of the bone. Measurements obtained were lacunar volume, lacunar-void-volume, and lacunar-void-volume/bone tissue. Averages were determined for each specimen for each measurement, along with top 20% of largest lacunar void volume.

Statistical Analysis

An unpaired t-test ($p < 0.05$) was used to compare OVX to Sham groups (when data was normally distributed). Normal data distribution was determined by the Shapiro-Wilk normality test. If data was not normally distributed, then a Mann-Whitney U test ($p < 0.05$) was used, reporting medians and interquartile range. Normally distributed data is reported with means ± standard deviation. All graphs utilize Whisker-Box plots, showing medians and ranges.

[68] MicroXCT-200, Zeiss, 1 Zeiss Drive, Thornwood, NY 10594
[69] Leica SP1600, Leica Biosystems Inc., 1700 Leider Lane, Buffalo Grove, IL 60089

In Vitro Cell Culture Model

Basic Cell Growth Protocol

MLO-Y4 (Kato et al. 1997) and TOPflash-MLO-Y4 osteocyte-like cell lines were cultured in regular growth media (Kato et al. 1997) (α-MEM[70] supplemented with 2.5% fetal bovine serum (FBS)[71] and 2.5% calf serum (CS)[72] and 1% Penicillin/Streptomycin (P/S)[73]) at 37°C @ 5% CO_2 on rat type I collagen[74] coated plates[75]. All experiments used media supplemented with 1% P/S, even if not directly stated. Phenol red free α-MEM media[76] was used during experimentation (since phenol red is a weak estrogen mimic) (Berthois et al. 1986) supplemented the same as above. Charcoal[77] stripped serums were also used (charcoal stripping of serums accomplished following Sigma-Aldrich protocol). For experimentation, cells were plated at a density of 2500-5000/cm^2 (depending on experiment) on rat type I collagen coated slides[78], or culture well plates[79]. Media was changed every 2-3 days on growing cells.

Characterization of MLO-Y4 in Charcoal Stripped Serum

Three experiments were utilized to characterize the morphology MLO-Y4 cells in charcoal stripped serum. The first experiment consisted of 3 slides (rat type I collagen coated, as described previously) of MLO-Y4 cells were plated at a density of 2500/cm^2 with 2.5% of each stripped serum in phenol red free media and left for 48 hours without media change. After 48 hours, one slide was harvested, the other two slides were changed to phenol red free media with 0.1% of each stripped serum. One slide was then harvested after 1 hour and the final slide was harvested at 2 hours. Slides

[70] Cat. No. 10-022-CV, Corning Inc., MediaTech Inc., Manassas, VA 20109
[71] Cat. No. S11195, Lot. No. A15002, Atlanta Biological, 4172 Industry Way, Flowery Branch, GA 30542
[72] Cat. No. SH30072.03, Lot. No. AMB15489, GE Healthcare Life Sciences, HyClone Laboratories, 925 West 1800 South, Logan, UT 84321
[73] Cat. No. 30-002-CI, Corning Inc., MediaTech Inc., Manassas, VA 20109
[74] Cat. No. 354236, Corning Inc., Discovery Labware Inc., 2 Oak Park, Bedford, MA 01730
[75] Cat. No. 430599/430293, Corning Inc., 1 River Front Plaza, Corning, NY 14831
[76] Cat. No. 41061-029, Gibco, Life Technologies, Grand Island, NY 14072
[77] Cat. No. C9157, Sigma-Aldrich, 3050 Spruce Street, St. Louis, MO 63103
[78] Cat. No. 6776214, Fisher Scientific, 300 Industry Drive, Pittsburgh, PA 15275
[79] Cat. Nos. 3598/3527/3512/3506, Corning Inc., 2 Alfred Road, Kennebunk, ME 04043

were fixed in 10% formalin[80] for 10 minutes, then stained with 0.1% crystal violet[81] in 1X Dulbecco's Phosphate-Buffered Saline (DPBS)[82]. Slides were imaged[83] at 5 areas along the edge and middle of the slide.

For the second experiment, MLO-Y4 cells were tested to assess optimal combinations and percentages of stripped serums. Cells were plated at a density of 2500/cm^2 in either regular α-MEM media or phenol red free media, with 3 slides per treatment groups. Treatment groups were regular α-MEM media with 2.5% of each stripped serum, phenol red free media with 2.5% of each serum, 2.5% of stripped FBS or CS only, 2.5% of one stripped serum and 1% of the other stripped serum, or 1% of stripped FBS or CS only. Slides were collected at 4, 24, and 48 hours (with media changes each time), fixed and processed as previously described.

The final experiment used MLO-Y4 cells plated at a density of 5000/cm^2, grown for 24 hours in phenol red free media with 2.5% of stripped FBS and CS each, then changed to new media with stripped serum concentrations of 2.5%, 1%, 0.5%, or 0.1% for 15 minutes, then put back into their original growth media and harvested after an additional 15 minutes. Three slides were used per treatment group, with 1 harvested for crystal violet staining and imaging as previously described and 2 harvested for western blot.

Slides for western blot were washed with cold 1X DPBS, treated with extraction buffer (1% protease inhibitor[84] and 1% phosphatase inhibitor[85] in RIPA buffer[86]), and cell lysates were recovered by centrifugation. Protein concentration was determined following Pierce® BCA Protein Assay Kit[87] instructions. Lower resolving gel (3 ml lower buffer solution (1.5M Tris[88] and 0.4% Sodium Dodecyl

[80] Cat. No. 23-245-685, Fisher Diagnostics, Fisher Scientific Company, 4481 Campus Drive, Kalamazoo, MI 49008
[81] Cat. No. 3886, Sigma-Aldrich, 3050 Spruce Street, St. Louis, MO 63103
[82] Cat. No. 21-031-CV, Corning, Cellgro, Mediatech Inc., Manassas, VA 20109
[83] Nikon Eclipse E800, Nikon Instruments, Inc., 1300 Walt Whitman Road, Melville, NY 11747
[84] Cat. No. P8340, Sigma-Aldrich, 3050 Spruce Street, St. Louis, MO 63103
[85] Cat. No. P2850, IBID
[86] Cat. No. R0278, IBID
[87] Product No. 23225, Pierce® BCA Protein Assay Kit, Thermo Scientific, 3747 North Meridian Road, Rockford, IL 61101
[88] Cat. No. 77-86-1, Research Products International Corporation, 410 North Business Center Drive, Mt. Prospect, IL 60056

Sulfate (SDS)[89], pH 8.8), 4.05 ml of 30% acrylamide[90], 4.95 ml distilled H_20 (dH_20), 10% ammonium persulfate (APS)[91] and 6 µl of TEMED[92]) was made and loaded into a 12-well cassette[93] and allowed to polymerize. Following polymerization, upper stacking gel (0.75 ml upper buffer (0.5M Tris-HCl[94] pH 6.7-6.8, 0.45 ml of 30% acrylamide, 1.8 ml dH_20, 9 µl APS, 3 µl TEMED) was made, added atop the resolving gel, and allowed to polymerize. A final concentration of 5ug of sample was loaded (with RIPA buffer to equilibrate volume) with 5X loading buffer (250mM Tris-HCl, 500mM Dithiothreitol (DTT)[95], 10% (SDS), and 0.5% Bromophenol Blue[96], and 50% Glycerol[97]) into the gel. Molecular weight standards were prepared using SeeBlue® pre-stained standard[98], MagicMark™[99] and RIPA buffer added for a final volume equal to the sample volume and loaded into the gel. Electrophoresis was run[100],[101] at 100V for 10 minutes, then 180V for 50 minutes in 1X running buffer (3g Tris, 14.4g Glycine[102], 1g SDS and 1L dH_20). Protein was then transferred to a nitrocellulose[103] membrane at 60V for 2 hours in 1X transfer buffer (5.8g Tris, 2.9g Glycine, .37g SDS and 1L dH_20).

Following transfer, the membrane was blocked with 5% non-fat dry milk in 1X TBST (10X TBST = 80g NaCl[104], 2g KCl[105], 30g Tris, 5 ml Tween-20[106] in 800 ml dH_20) on a rocker plate for 1 hour. Following blocking, primary antibody for phosphorylated Akt[107] (pAkt) was diluted 1:2000 in 3% BSA in

---

[89] Cat. No. 161-0302, BioRad, 2000 Alfred Nobel Drive, Hercules, CA 94547
[90] Cat. No. EC-890, Protogel, National Diagnostics, 305 Patton Drive, Atlanta, GA 30336
[91] Cat. No. EC-504, IBID
[92] Cat. No. EC-503, IBID
[93] Cat. No. 345-9901, Criterion™ Empty Cassettes, BioRad, 2000 Alfred Nobel Drive, Hercules, CA 94547
[94] Cat. No. 7674-01-0, Acros Organics, Thermo Scientific, 500 American Road, Morris Plains, NJ 07950
[95] Cat. No. EC222-468-7, Fisher Scientific, 300 Industry Drive, Pittsburgh, PA 15275
[96] Cat. No. 115-39-9, Sigma-Aldrich, 3050 Spruce Street, St. Louis, MO 63103
[97] Cat. No. IB15760, IBI Scientific, 9861 Kapp Court, Peosta, IA 52068
[98] Cat. No. LC5625, Invitrogen™, 29851 Willow Creek Road, Eugene, OR 97402
[99] Cat. No. LC5602, IBID
[100] Product No. 043BR26470, PowerPac™ HC, BioRad, 2000 Alfred Nobel Drive, Hercules, CA 94547
[101] Product No. 560BR17267, Criterion™ Blotter, IBID
[102] Cat. No. IB70194, MidSci, 280 Vance Road, St. Louis, MO 63088
[103] Cat. Nos. 10-4858-289/10-401-196, IBID
[104] Cat. No. S9888, Sigma-Aldrich, 3050 Spruce Street, St. Louis, MO 63103
[105] Cat. No. P9541, IBID
[106] Cat. No. 9005-64-5, Fisher Scientific, 300 Industry Drive, Pittsburgh, PA 15275
[107] Cat. No. 4060, Cell Signaling Technology, 3 Trask Lane, Danvers, MA 01923

1x TBST and the membrane was incubated with 3 ml of the primary antibody solution overnight at 4°C on a rocker plate. The next day, the membrane was washed with 3 times with 5 ml of 1X TBST for 5 minutes each. Secondary antibody[108] (anti-rabbit IgG) was diluted 1:3000 in 3% BSA in 1X TBST and the membrane was incubated with 3 ml of the secondary antibody solution covered with foil, at room temperature, for 1 hour with rocking. After 1 hour, the membrane was washed 3 times with 5 ml of 1X TBST for 10 minutes each. Membrane was incubated with SupraSignal[109] for 3-5 minutes on rocker plate to allow oxidation of substrates (horseradish peroxidase via hydrogen peroxide), resulting in the release of light as a byproduct. Bands were visualized using the Luminescent Image Analyzer LAS 400 (Fuji)[110] with high resolution chemiluminescence and incremental and precision exposure time.

Following visualization, membrane was stripped with Restore™ PLUS Western Blot Stripping Buffer [111] for 5-15 minutes, rinsed 3 times with 5 ml 1X TBST for 5 minutes each. Control antibody (against β-actin)[112] was diluted 1:25000 in 5% non-fat dry milk in PBST (0.1% Tween-20 in PBS). The membrane was incubated with 3 ml of control antibody for 2 hours at room temperature with rocking, then washed 3 times with 5 ml 1X TBST for 10 minutes each. Membrane was again incubated with SupraSignal as previously described and imaged as previously described. Bands were quantified using Multi-Gauge Software[113].

TOPflash-MLO-Y4 Luciferase Assay and DNA Quantification Protocol

TOPflash-MLO-Y4 cells are MLO-Y4 cells that have been stably transfected with pGL4.49 [*luc2P*/TCF-LEF/Hygro] vector[114] (obtained from Dr. Nuria Lara-Castillo, unpublished). As a result, these cells express luciferase when β-catenin signaling is activated. Activation of β-catenin signaling in

[108] Cat. No. AB-105-C, R&D Systems, 614 McKinley Place NE, Minneapolis, MN 55413
[109] Product No. 37071, SuperSignal® West Dura Trial Kit, Thermo Scientific, 3747 North Meridian Road, Rockford, IL 61101
[110] Luminescent Image Analyzer LAS 400 (Fuji), 41 Farnsworth Street, Boston, MA 02210
[111] Product No. 46430, Restore™ PLUS Western Blot Stripping Buffer, Thermo Scientific, 3747 North Meridian Road, Rockford, IL 61101
[112] Cat. No. A3854, Sigma-Aldrich, 3050 Spruce Street, St. Louis MO 63103
[113] Fuji Film Multi-Gauge Software, Fuji Photo Company, 41 Farnsworth Street, Boston, MA 02210
[114] Cat. No. E4611, Promega Corporation, 2800 Woods Hollow Road, Madison, WI 53711-5399

TOPflash-MLO-Y4 cells was quantitated by the amount of luminescence given by the cells following treatment using a Luciferase Assay Kit[115].

Harvesting of cells for luciferase assay was performed as follows: 1X DPBS, 1X cell lysis buffer (CLB) and Luminescence Assay Reagent (LAR) were brought to room temperature. Media was removed from the cells, and cells were washed 2 times with room temperature 1X DPBS. Cells were lysed using the luciferase cell culture lysis reagent (30-50 µl/well; 120 µl/slide). From this lysate, 20 µl was removed and placed into white, flat bottom 96-well plate[116]. A minimum of 2 replicates were taken. A reading of the plate to determine blank, background luminescence, which was then subtracted from the final reading. Luciferase substrate was then added to each well (100 µl) and luciferase activity was read[117] for 10 seconds and recorded as counts per second (CPS).

The remaining cell lysate was utilized for DNA quantitation. High Salt Buffer (HSB) (10X PBS, 10 mM EDTA[118], 2M NaCl[119]) was added to the lysate in a 1:100 fashion. This solution then went through 2 freeze/thaw cycles. DNA standard[120] was diluted to 100µg/ml. Ten µl of the DNA standard was added to 20 µl of 10X fluorescent assay buffer[121] and 170 µl of 1:10 (CLB:HSB) solution. This gave a final solution of 5 ng/µl DNA solution that was used to prepare a standard curve (0, 5, 10, 15, 20, 30 ng/µl) when mixed with 1:10 (CLB:HSB). DNA standards and samples were transferred to a black, flat bottom 96-well plate[122] (20 µl/well; in triplicate). BisBenzimide H 33258[123] stock (1 mg/ml) was diluted to a 0.1 µg/ml solution in 10X fluorescent assay buffer and nanopure water. Then, 200 µl of the bisBenzimide solution was added per well. The plate was covered with foil and incubated in the dark

[115] Cat. No. E1501, Promega Corporation, 2800 Woods Hollow Road, Madison, WI 53711-5399
[116] Cat. No. 6005680, Perkin Elmer Inc., 940 Winter Street, Waltham, MA 02451
[117] Product No. 1420-011, Wallac Victor 2 Multii-label, IBID
[118] Cat. No. 15694, USB Corporation, 26111 Miles Road, Cleveland, OH 44128
[119] Cat. No. AM9760G, Fischer Scientific, Life Technologies, Ambion Inc., Invitrogen™, 5781 Van Allen Way, Carlsbad, CA 92008
[120] Cat. No. D4810, Sigma-Aldrich, 3050 Spruce Street, St. Louis, MO 63103
[121] Cat. No. F7171, IBID
[122] Cat. No. 07-200-627, Corning™, Fisher Scientific Company, 4481 Campus Drive, Kalamazoo, MI 49008
[123] Cat. No. B1155, Sigma-Aldrich, 3050 Spruce Street, St. Louis, MO 63103

for 24 hours. After 24 hours, DNA amount was determined spectrophotometrically[124] using 360 nm for excitation, 460 nm for emission, with no shaking. The average of 6 readings was recorded. DNA in the samples was determined by comparing against a DNA standard curve. The DNA amount was calculated for 20 µl of the starting lysate for comparison to the luciferase CPS reading. Final luciferase assay activity was measured as CPS/DNA(ng).

TOPflash-MLO-Y4 Response to Wnt and Estrogen in Stripped Serum and Phenol Red Free Media

TOPflash-MLO-Y4 cells were seeded onto collagen coated 96-well plates at a density of 3000/well in either regular α-MEM or phenol red free media supplemented with either 2.5% stripped FBS and CS or 2.5% of regular, non-stripped serums, ± 10ng/ml Wnt3a[125], and ± 10^{-6} M 17β-estradiol. All conditions were run in triplicate. Cells were allowed to incubate in their media (100µl/well) overnight (12-18 hours) and were harvested the next day according to the luciferase protocol as previously described. Only luciferase counts per second (CPS) were recorded, without DNA quantification. All experiments were repeated at least 3 times.

TOPflash-MLO-Y4 Estrogen Receptor (ER) α/β Polymerase Chain Reaction (PCR)

TOPflash-MLO-Y4 cells were grown in 6 well plates at a density of 2800/cm^2 with phenol red free media and 2.5% FBS and CS each. Cells were harvested for PCR at time 0, 4, 8, 24, hours after initial plating. At 24 hours, 17β-estradiol[126] (10^{-6} M final) was added to the cells, and cells were harvested for PCR at 4, 8, and 24hours post-estrogen addition. A total of 2 ml of treatment media was used per well.

Cells for PCR were harvested by the addition of Trizol[127] and collected. RNA was isolated and yield determined[128] according to Trizol protocol provided by Ambion. RNA was converted into cDNA

[124] SpectraMax M5E Multi-Mode Microplate Reader, Molecular Devices, 3860 North First Street, San Jose, CA 95134
[125] Cat. No. 1324-WN, R&D Systems, 614 McKinley Place NE, Minneapolis, MN 55413
[126] Cat. No. E2758, Sigma-Aldrich, 3050 Spruce Street, St. Louis MO 63103
[127] Cat. No. 15596018, Fischer Scientific, Life Technologies, Ambion Inc., Invitrogen™, 5781 Van Allen Way, Carlsbad, CA 92008
[128] Cat. No. ND-2000, NanoDrop 2000, Thermo Scientific, 3747 North Meridian Road, Rockford, IL 61101

using and following protocol for a high-capacity cDNA reverse transcription kit[129] and thermal cycler[130]. Following cDNA amplification, Real-time PCR was performed. A solution of 5 µl of master mix[131], 0.5 µl of gene array (ERα[132], ERβ[133], β-actin[134], or 18S[135]) and nuclease-free water[136] to a final volume of 7.5 µl for each sample was made, enough to be run in triplicate. A volume of 7.5 µl was pipetted into the required number of wells on a 96 well plate[137] and 2.5 µl of 10ng/ml cDNA was added to each well. A no reverse transcriptase cDNA and well of nuclease-free water were included as controls. The plate was sealed[138] and centrifuged at 1000 rpm for 1 minute and then placed into the OneStepPlus™ RT-PCR System[139]. Samples were heated at 50°C for 2 minutes, then denatured for 10 minutes at 95°C, followed by forty cycles of 95°C for 15 seconds and 60°C for 1 minute.

TOPflash-MLO-Y4 Estrogen and ER Inhibitor (ICI)

TOPflash-MLO-Y4 cells were plated in phenol red free media supplemented with 2.5% FBS and CS each, at a density of 3000/well in a 96-well plate for 24 hours prior to treatment. Cells treated with ±10ng Wnt 3a, 10^{-6} M 17β-estradiol, and 100nM Fulvestrant[140] (anti-estrogen receptor ICI 182,780 here forth referred to as just ICI) and combinations of each. DMSO[141] (100nM) was used as a control in the Wnt negative groups. Each treatment was run in triplicate wells. Each well received 100 µl of treatment media and were incubated overnight. Cells were harvested for Luciferase and DNA assays as previously described.

---

[129] Cat. No. 4368814, Applied BioSystems™, ThermoFisher Scientific, 850 Lincoln Centre Drive, Foster City, CA 94404
[130] Model 5345, Eppendorf 5345 EPGradient-S MasterCycler, 102 Motor Parkway, Hauppauge, NY 11788
[131] Cat. No. 4370048, TaqMan™ Gene Expression Master Mix, Applied BioSystems™, ThermoFisher Scientific, 850 Lincoln Centre Drive, Foster City, CA 94404
[132] Cat. No. 4331182, Mm00433149_m1, IBID
[133] Cat. No. 4331182, Mm00599821_m1, IBID
[134] Cat. No. 4331182, Mn00670739_s1, IBID
[135] Cat. No. 4331182, Hs99999901_s1, IBID
[136] Cat. No. P119, Promega Corporation, 2800 Woods Hollow Road, Madison, WI 53711-5399
[137] Cat. No. AB19800-EU, EU Fast Cycler PCR Plate, MidSci, 280 Vance Road, St. Louis, MO 63088
[138] Cat. No. TS-RT2RR-100, Thermal Seal, IBID
[139] Cat. No. 4376600, OneStepPlus™ RT-PCR System, Applied BioSystems™, ThermoFisher Scientific, 850 Lincoln Centre Drive, Foster City, CA 94404
[140] Cat. No. ab120131, Abcam, 1 Kendall Square, Suite B2304, Cambridge, MA 02139-1517
[141] Cat. No. 68-67-5, Fisher Scientific, 300 Industry Drive, Pittsburgh, PA 15275

TOPflash-MLO-Y4 ICI Pretreatment without Fluid Flow Sheer Stress (FFSS)

Two experiments were utilized to determine effects of pretreatment with ICI followed by secondary treatments with 17β-estradiol and Wnt3a. For both experiments TOPflash-MLO-Y4 cells were plated in phenol red free media supplemented with 2.5% FBS and CS each, at a density of 3000/well in a 96-well plate for 24 hours prior to treatment. ICI was then added 24 hours prior to treatments. ICI negative treatments with DMSO (100nM) were used as controls. Treatments were left on cells for 24 hours before harvesting for Luciferase and DNA assays as previously described. The first experiment utilized treatments groups of: ±10ng Wnt 3a and +Wnt3a along with 17β-estradiol at concentrations of 10^{-6}, 10^{-7}, 10^{-8}, and 10^{-9} M for 24 hours to determine appropriate 17β-estradiol concentration following ICI pretreatment. The second experiment had treatment groups of ±10ng Wnt 3a, ± 10^{-6} M 17β-estradiol, and ± 100nM ICI, and combinations of each to determine effects of these treatment combinations prior to running the same conditions with FFSS.

ICI pretreatment was also used for PCR to determine ERα/β mRNA levels. TOPflash-MLO-Y4 cells were plated in phenol red free media supplemented with 2.5% FBS and CS each, at a density of 3000/cm^2 in a 6-well plate for 24 hours prior to treatment. ICI was then added at a concentration of 100nM 24 hours prior to treatments. After 24 hours, the ICI negative treatment and pretreatment were harvested for PCR as previously described. Other wells received either 10^{-6} M 17β-estradiol, 10 ng/ml Wnt3a, 10^{-6} M 17β-estradiol and 10 ng/ml Wnt3a in combination, or a fresh media change with DMSO (100nM). After 24 hours in treatment, cells were harvested for PCR as previously described.

TOPflash-MLO-Y4 with FFSS

Two separate experiments were performed with TOPflash-MLO-Y4 cells receiving FFSS. The FFSS system[142,143,144] simultaneously applies flow to 6 slides. For both experiments, TOPflash-MLO-Y4 cells were plated in phenol red free media supplemented with 2.5% FBS and CS each, at a density

[142] Cat. No. 77200-60, MasterFlex® L/S™, Cole-Parmer®, 625 East Bunker Court, Vernon Hills, IL 60061
[143] Cat. No. 07550-30, Easy-Load II®, IBID
[144] LabVIEW™ Run-Time, National Instruments™, 11500 North Mopac Expressway, Austin, TX 78759-3504

of 3000/cm^2 on collagen coated slides for 24 hours prior to treatment. After 24 hours, FFSS was run at 2 dynes/cm^2 for 30 minutes at 5% CO_2 and 37°C (Kamel et al. 2010a), in fresh media with the same supplements as listed. At the same time, static slides were moved into identical media for 30 minutes to replicate the movement of slides from the media into the FFSS chamber. After 30 minutes, all slides were put back into their growth media with the addition of 10ng/ml of Wnt3a or Wnt negative controls. For the first experiment, cells were then harvested for Luciferase and DNA assay as previously described at 2, 4 and 24 hours post-FFSS. For the second experiment, cells were incubated with or without 100nM of ICI for 24 hours prior to FFSS. FFSS was performed under the same conditions as listed above, with DMSO (100nM) serving as a control for ICI negative treatments. Cells were incubated for 24 hours post-FFSS in the original 24 hour incubation media ±10ng/ml Wnt 3a and then harvested for Luciferase and DNA assays as previously described.

Statistical Analysis

If data was not normally distributed, then a Mann-Whitney U test (for comparisons between two treatment groups) or a Kruskall-Wallis test (for comparisons within groups) was used (both $p < 0.05$), reporting medians and interquartile range. If differences were seen within treatment groups, a post-hoc Bonferroni test was performed. Normally distributed data is reported with means ± standard deviation, using a 2 sample t-test or ANOVA.

Chapter 3

RESULTS

In Vivo Mouse Model

Body and Uterus Weight

Body and uterus weight (fig. 5) were taken post-sacrifice. While body weight was not significant between the two groups ($p = 0.3241$), the uterus weight was significantly less in the OVX group ($p < 0.0001$).

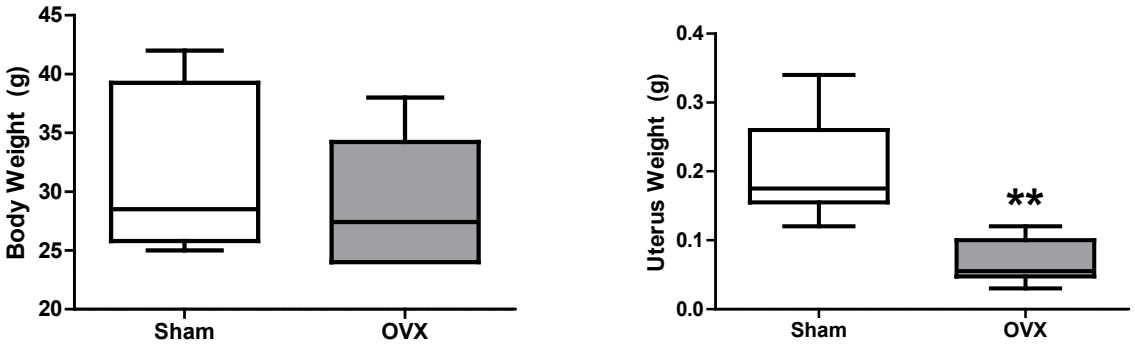

Figure 5. Uterus weight but not body weight is altered after OVX. Body weight (A) was not significantly different between Sham and OVX, but uterus weight was significantly decreased in the OVX group. (**$p < 0.0001$; $n = 10$).

β-galactosidase Counting and Immunohistochemistry

To determine the activation of the Wnt/β-catenin pathway following a single session of mechanical loading, β-galactosidase positive cells were counted anterior and posterior of the medullary cavity using a MatLab based software developed by Dr. Ganesh Thiagarajan (UMKC School of Computing and Engineering), along with a secondary confirmation through visual counting using Image J and Microsoft Photo Viewer. Data was analyzed for normal distribution, which was not met, so a Mann-Whitney U test was used, reporting medians and interquartile ranges (IQR) 25%-75%. The 1 hour OVX mice had a slightly lower (0.8286; IQR = 0.7558-0.9772) number of β-galactosidase positive osteocytes than the Sham group (0.9292; IQR = 0.7576-1.278); however, this was not significant ($p = 0.6905$). For the 24 hour time point, the OVX group (0.4284; IQR = 0.3696-0.5649) had a significant

decrease (p = 0.0079) in number of number of β-galactosidase positive osteocytes compared to the Sham group (0.8291; IQR = 0.7522-1.333) (fig. 6).

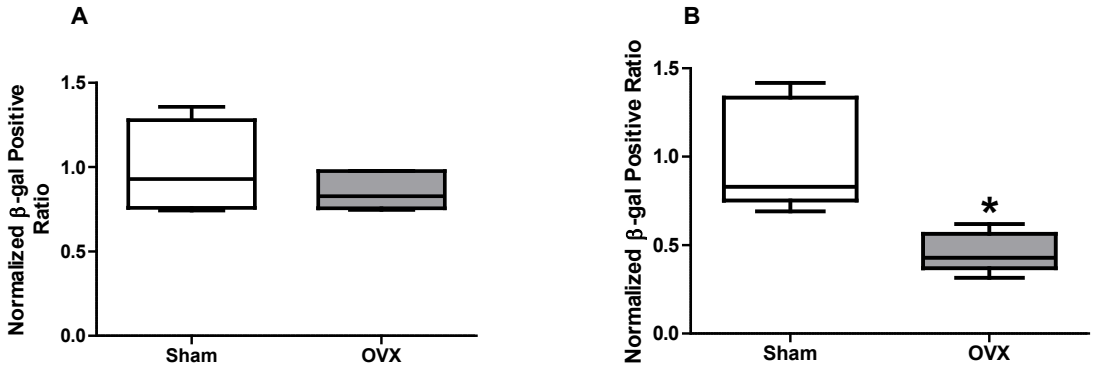

Figure 6. OVX decreases β-galactosidase positive osteocytes following a single session of mechanical loading . After 1 hour (A) OVX mice have a downward trend in responsiveness. At 24 hours (B), which is peak activation of the Wnt/β-catenin pathway, there is a significant (p = 0.0079) decrease in osteocyte activation. Ratio determined by (RT/LT)/Sham average.The box plots show the median as a line within the box. (*p < 0.05; n = 5).

Micro-CT

Micro-CT was used to analyze potential changes in the cortical and trabecular parameters of the bone, due to OVX. Cortical parameters measured were BMD, BV/TV, thickness; periosteal, endosteal and total perimeters. All parameters met the normal distribution test and were analyzed with an unpaired t-test, reporting means ± standard deviation (SD), except for BV/TV, which was analyzed with a Mann-Whitney U test and reporting the median with IQR.

Cortical thickness was the only parameter to show a significant change (p = 0.0435) between the Sham and OVX groups, with the OVX group having a lower thickness. While the periosteal perimeter did not show a significant decrease (p = 0.0503) from the Sham to OVX group, it did indicate a decreasing trend. All cortical results are shown in table 2 and figure 7. Figure 8 shows representations of 3-dimensional reconstructions of Sham and OVX cortical bones.

Trabecular bone showed more significant changes compared to cortical bone. Trabecular bone parameters measured were trabecular BMD, BV/TV, thickness, separation and number. All data showed a normal distribution and are reported with means ± SD. Trabecular BMD was significantly

decreased in the OVX group ($p = 0.0420$), as well as trabecular BV/TV ($p = 0.0097$) and trabecular thickness ($p = 0.0004$). Results of trabecular Micro-CT are shown in table 3 and figure 9. Figure 10 shows representations of 3-dimensional reconstructions of trabecular bone from a Sham and OVX animal.

TABLE 2

CORTICAL MICRO-CT PARAMETERS

	BMD	BV/TV	Thickness*	Periosteal Perimeter	Endosteal Perimeter	Total Perimeter
Sham	1.39±0.088	99.94 (99.92, 99.99)	0.19±0.01	6.29±0.14	3.30±0.14	9.59±0.257
OVX	1.32±0.10	99.93 (99.14, 99.99)	0.18±0.12	6.02±0.37	3.42±0.27	9.44±0.54

*(n = 10; *p < 0.05 between Sham and OVX of same parameter)

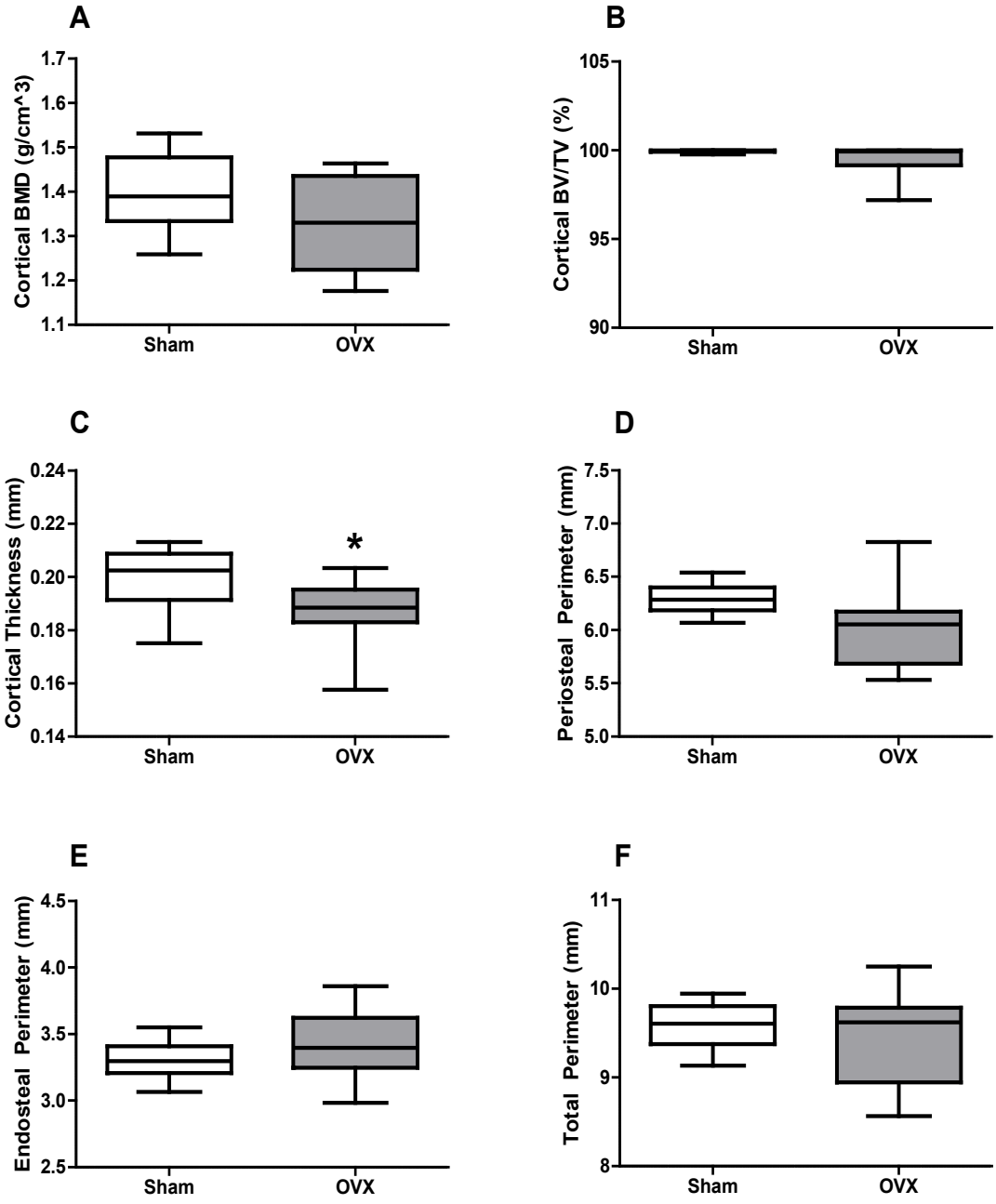

Figure 7. Cortical bone parameters at 4 weeks post-OVX. The only parameter to show a significant decrease in the OVX group was cortical thickness (C). All other parameters, BMD (A), BV/TV (B), Periosteal Perimeter (D), Endosteal Perimeter (E), and Total Perimeter (F), were not significant. (*$p < 0.05$; $n = 10$).

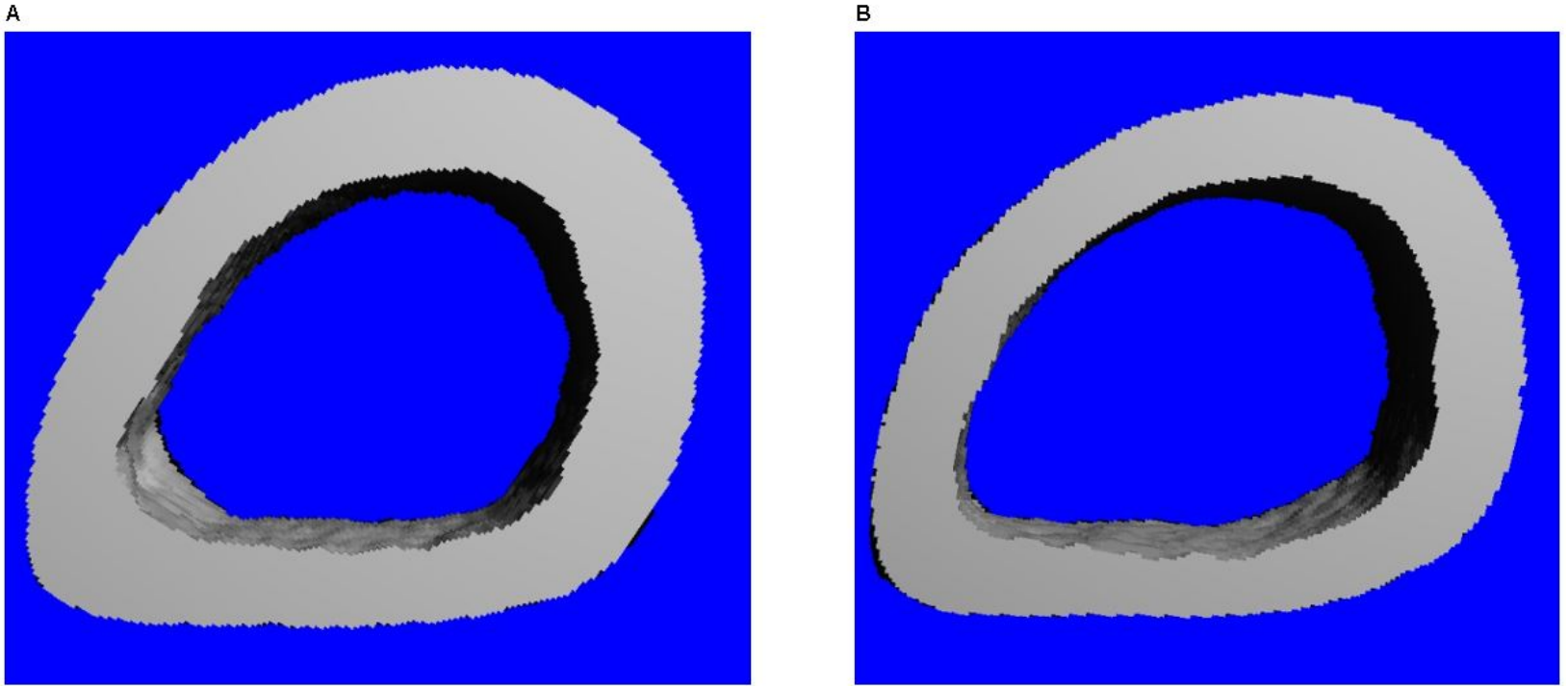

Figure 8. Three-dimensional reconstruction of mouse cortical bone. Cortical thickness was significantly decreased in the OVX (B) (see fig. 7) group compared to the Sham (A) group ($p = 0.0435$).

TABLE 3

TRABECULAR MICRO-CT PARAMETERS

	BMD*	**BV/TV***	**Thickness***	**Separation**	**Number**
Sham	0.96±0.048	16.77±5.31	0.05±0.008	0.25±0.08	2.96±0.88
OVX	0.91±0.042	10.82±3.73	0.04±0.005	0.25±0.05	2.47±0.72

*(n = 10; *p < 0.05 between Sham and OVX of same parameter)

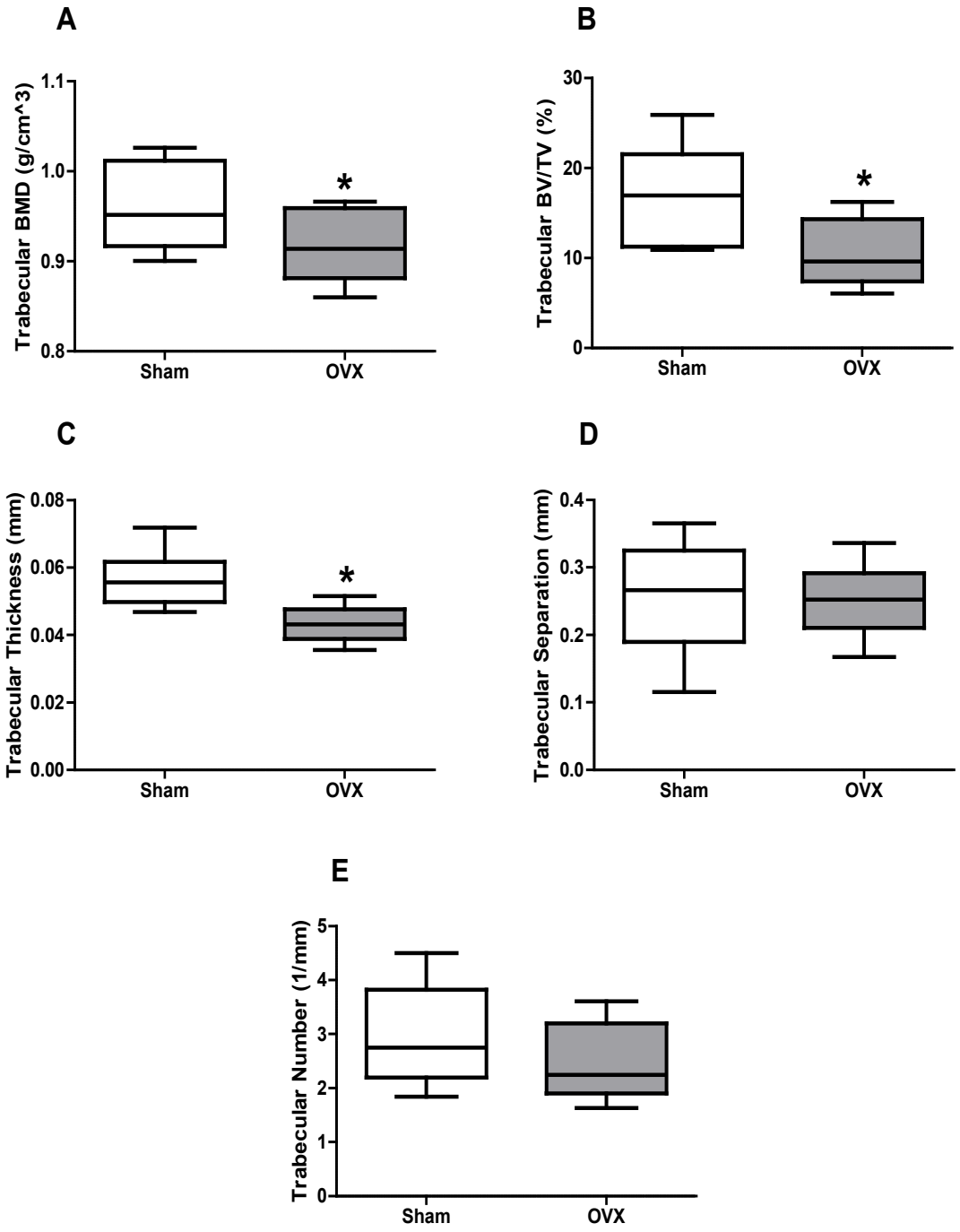

Figure 9. Trabecular bone parameters at 4 weeks post-OVX. Trabecular BMD (A), BV/TV (B) and thickness (C) were all significantly decreased in the OVX group. There was no significance in trabecular separation or number between the two groups. (*$p < 0.05$; $n = 10$).

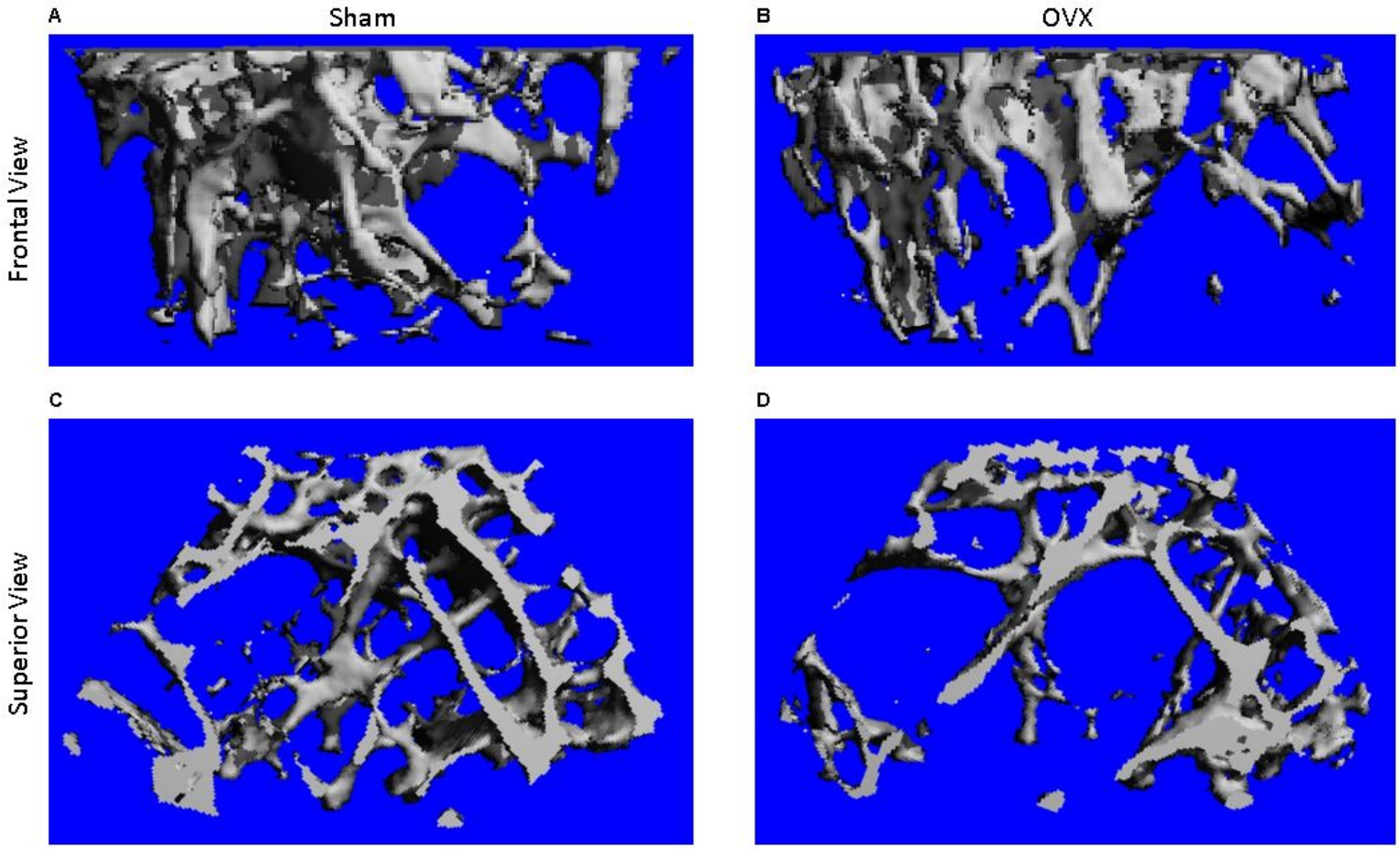

Figure 10. Three-dimensional reconstructions of trabecular bone. Note the dramatic loss of trabeculae following OVX.

Biomechanical Testing

Three-point bending to failure was conducted on the right femurs following micro-CT. Parameters measured were ultimate load (UL), work to failure (WTF), plastic work to failure (PWTF), post yield displacement (PYD), stiffness, elastic work to failure (EWTF), elastic displacement (EDIS), and Young's Modulus (E), all of which had a normal distribution (reported as means ± SD) of data except for stiffness (reported as median with IQR). Statistical analysis revealed no significance for any parameters between the Sham and OVX group. Biomechanical testing results are reported in table 4 and figure 11. A graph of a typical load displacement curve (for both Sham and OVX) is shown in figure 12.

TABLE 4

BIOMECHANICAL TESTING PARAMETERS

	UL	WTF	PWTF	PYD	Stiffness	EWTF	EDIS	E
Sham	15.64±2.43	4.21±1.69	3.08±2.00	2.68±0.04	82.32 (65.59, 84.42)	1.13±0.55	0.18±0.46	4.66±0.83
OVX	14.80±2.95	4.19±3.12	3.01±3.21	2.69±0.09	78.70 (54.01, 93.85)	1.182±0.80	0.18±0.08	4.76±1.48

*(n = 10; No significance in any parameters)

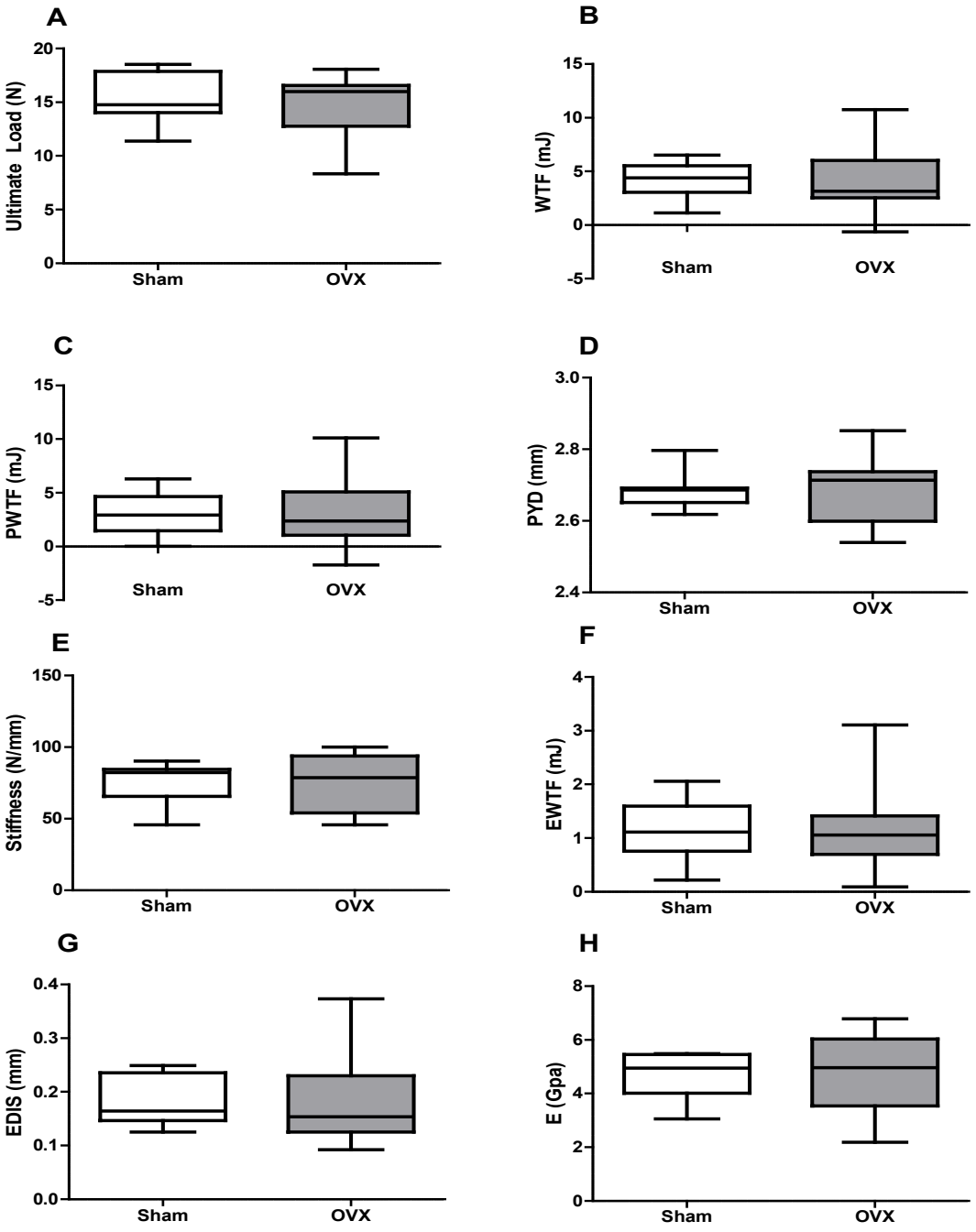

Figure 11. Biomechanical parameters at 4 weeks post-OVX. Parameters measured were ultimate load (A), work to failure (B), plastic work to failure (C), post yield displacement (D), stiffness (E), elastic work to failure (F), elastic displacement (G)and Young's Modulus (H) (n = 10; No significance in any parameters).

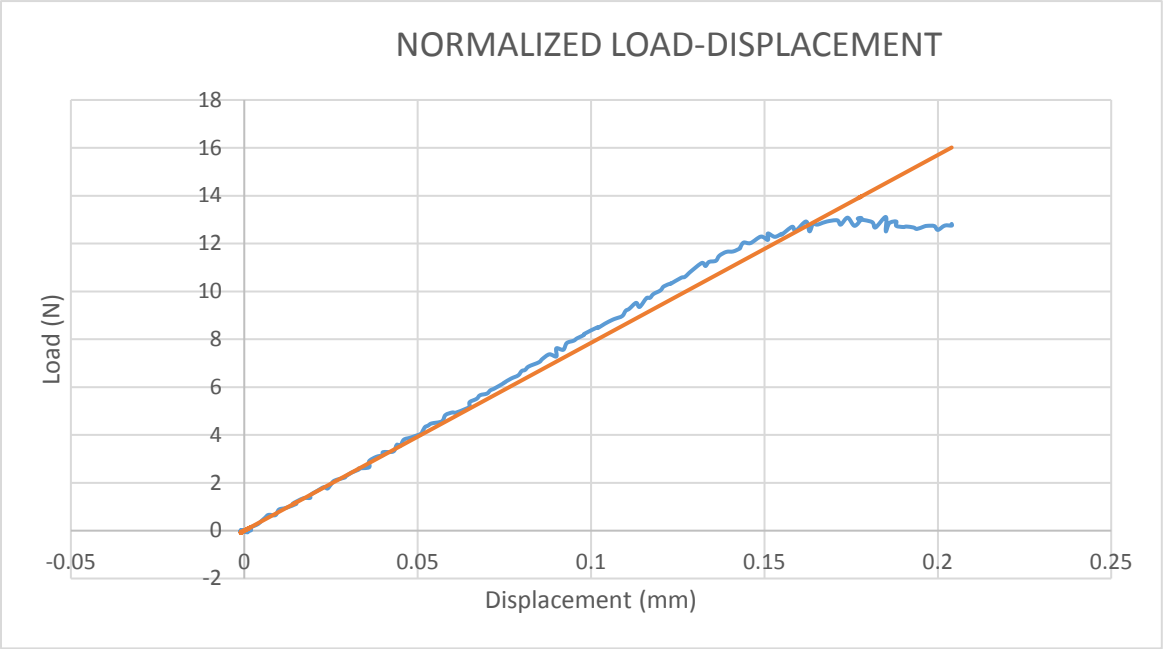

Figure 12. Representation of normalized load displacement curve. The curve was generated using parameters from 3-point bending, micro-CT, and BoneJ plug-in for ImageJ. This represents a typical curve for both Sham and OVX groups.

VonKossa and TRAP Staining

VonKossa staining was used to examine osteoblasts at the trabecular surface of the tibia in the region 150μm distal to the proximal growth plate. Osteoblasts were counted, along with osteoblast surface and total bone surface. From this, total osteoblast number, osteoblast surface/bone surface (OBS/BS) and number of osteoblasts/bone perimeter (N.OB/B.Pm) were derived. All data was tested for normal distribution, which was not met, so a Mann Whitney test was used and values reported are medians and IQR. All parameters measured showed a significant decrease in the OVX group as compared to the Sham group. Osteoblast results are reported in table 5 and figure 13. Figure 14 indicates the 6 adjacent fields measured in the trabecular area of interest, along with a single area with an osteoblast indicated.

TRAP staining was used to examine osteoclasts at the trabecular surface of the tibia in the same region at 150μm distal to the proximal growth plate. Osteoclasts were counted, along with osteoclast surface and total bone surface. From this, the total number of osteoclasts, osteoclasts surface/bone surface (OCS/BS), and number of osteoclasts/bone perimeter (N.OC/B.Pm) were derived. All data was tested for normal distribution. Osteoclast number and N.OC/B.Pm did not meet normalcy and are reported as medians with IQR, while OCS/BS was normal and is reported with means ± SD. All three parameters showed a significant increase in the OVX group as compared to the Sham group. Osteoclast results are reported in table 6 and figure 15. Figure 16 indicates the 6 adjacent fields measured in the trabecular area of interest, along with a single area with an osteoclast indicated

TABLE 5

VONKOSSA STAINING FOR OSTEOBLASTS

	Osteoblast Number*	**OBS/BS***	**N.OB/B.Pm***
Sham	17.50 (6.5, 24.5)	9.07 (5.86, 13.88)	6.93 (4.18, 9.71)
OVX	7.5 (0, 15.25)	4.49 (0, 8.69)	2.95 (0, 6.26)

*(n = 6; *p < 0.05 for Sham and OVX of same parameter)

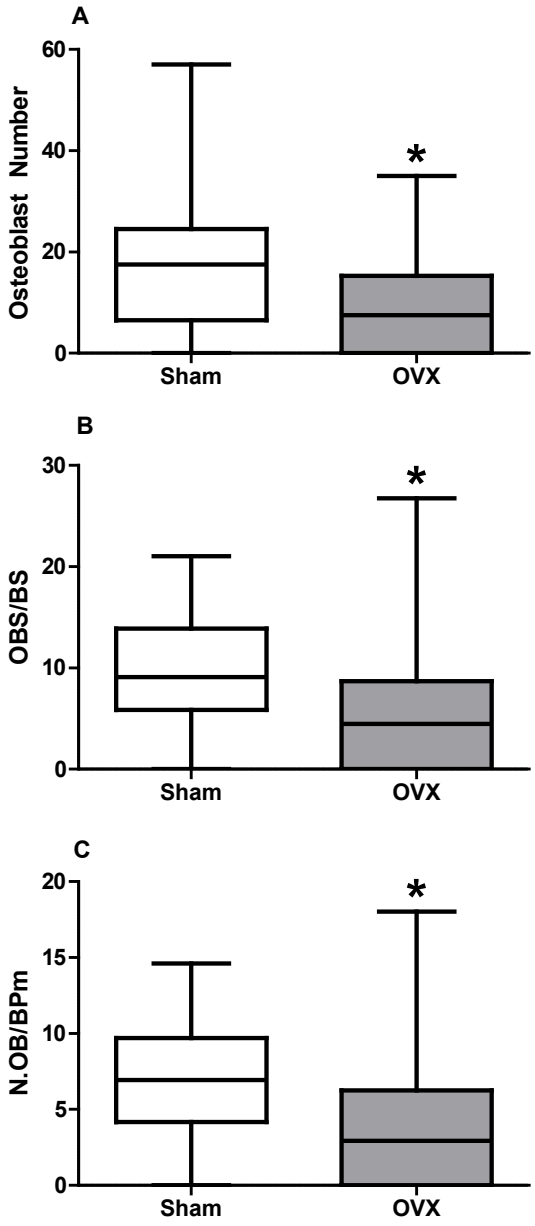

Figure 13. Osteoblast number, surface area and ratio decrease after OVX. Osteoblast number (A), osteoblast surface/bone surface (B) and (C) number of osteoblasts/bone perimeter. (*$p < 0.05$; $n = 6$).

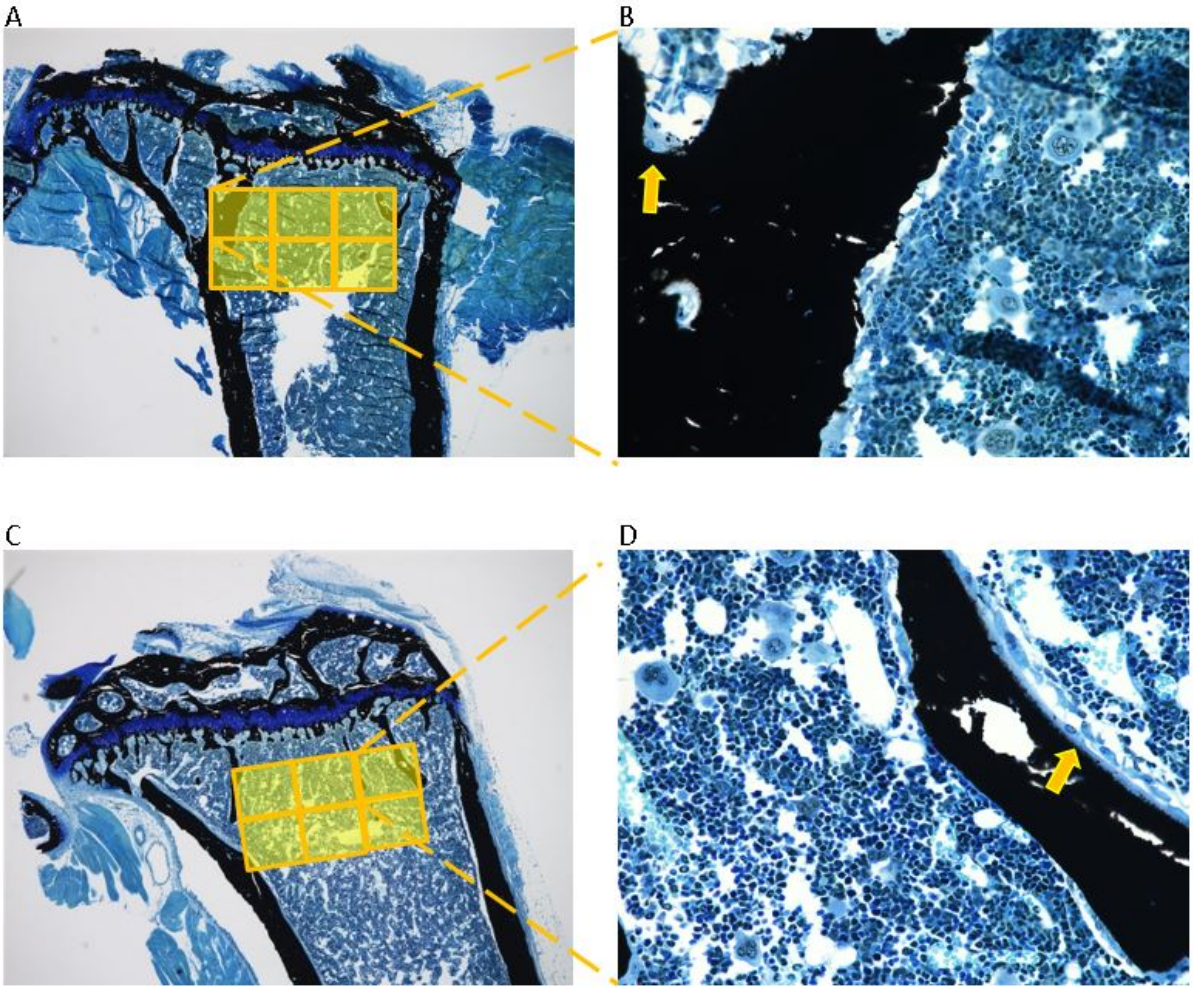

Figure 14. Regions of interest for osteoblasts counting via VonKossa staining. A (Sham) and C (OVX) show the entire area counted (at 4X), which is 150 um distal to the proximal growth plate, marked into 6 areas, each 50 x 50. B (Sham) and D (OVX) show one of the six regions counted (at 20X), with an arrow pointing to an osteoblast.

TABLE 6

TRAP STAINING FOR OSTEOCLASTS

	Osteoclast Number*	**OCS/BS***	**N.OC/B.Pm***
Sham	3 (1, 7)*	3.59±2.68*	1.70 (1.12, 2.57)*
OVX	7.5 (4, 11)*	6.37±3.70*	3.92 (2.24, 5.27)*

*(n = 6; *p < 0.05 for Sham and OVX of same parameter)

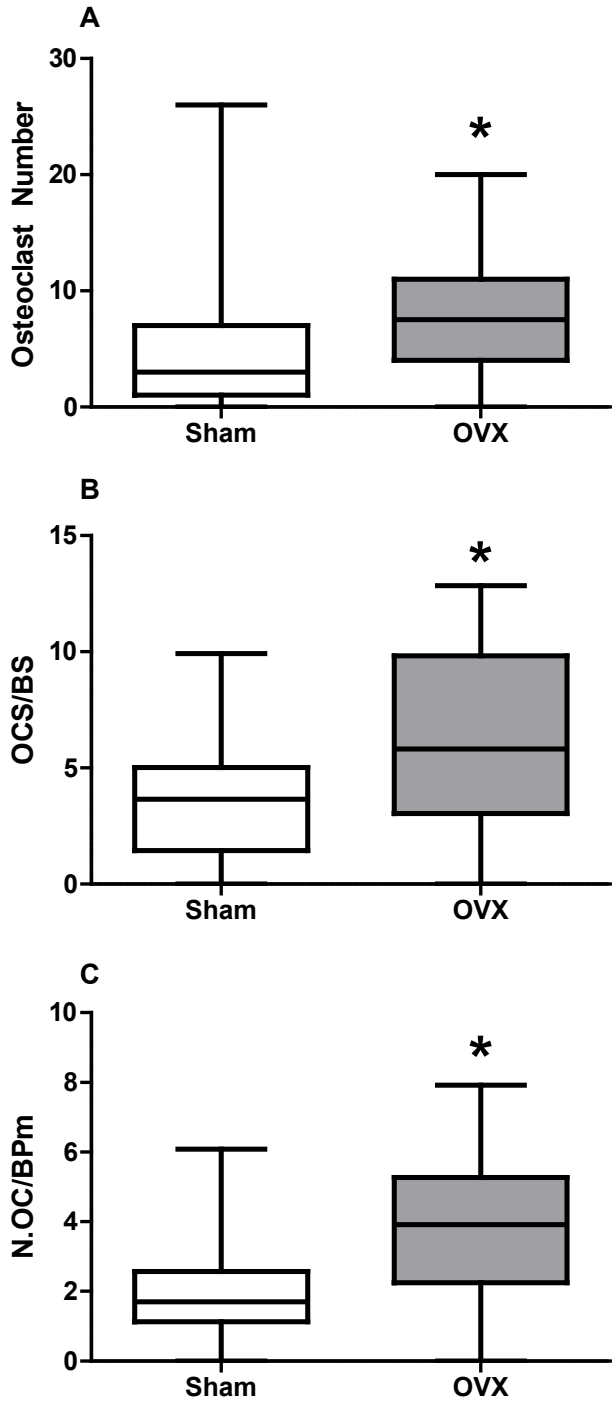

Figure 15. Osteoclast number, surface and ratio increase after OVX. Osteoclast number (A), osteoclast surface/bone surface (B), and (C) number of osteoclasts/bone perimeter. (*$p < 0.05$, $n = 6$).

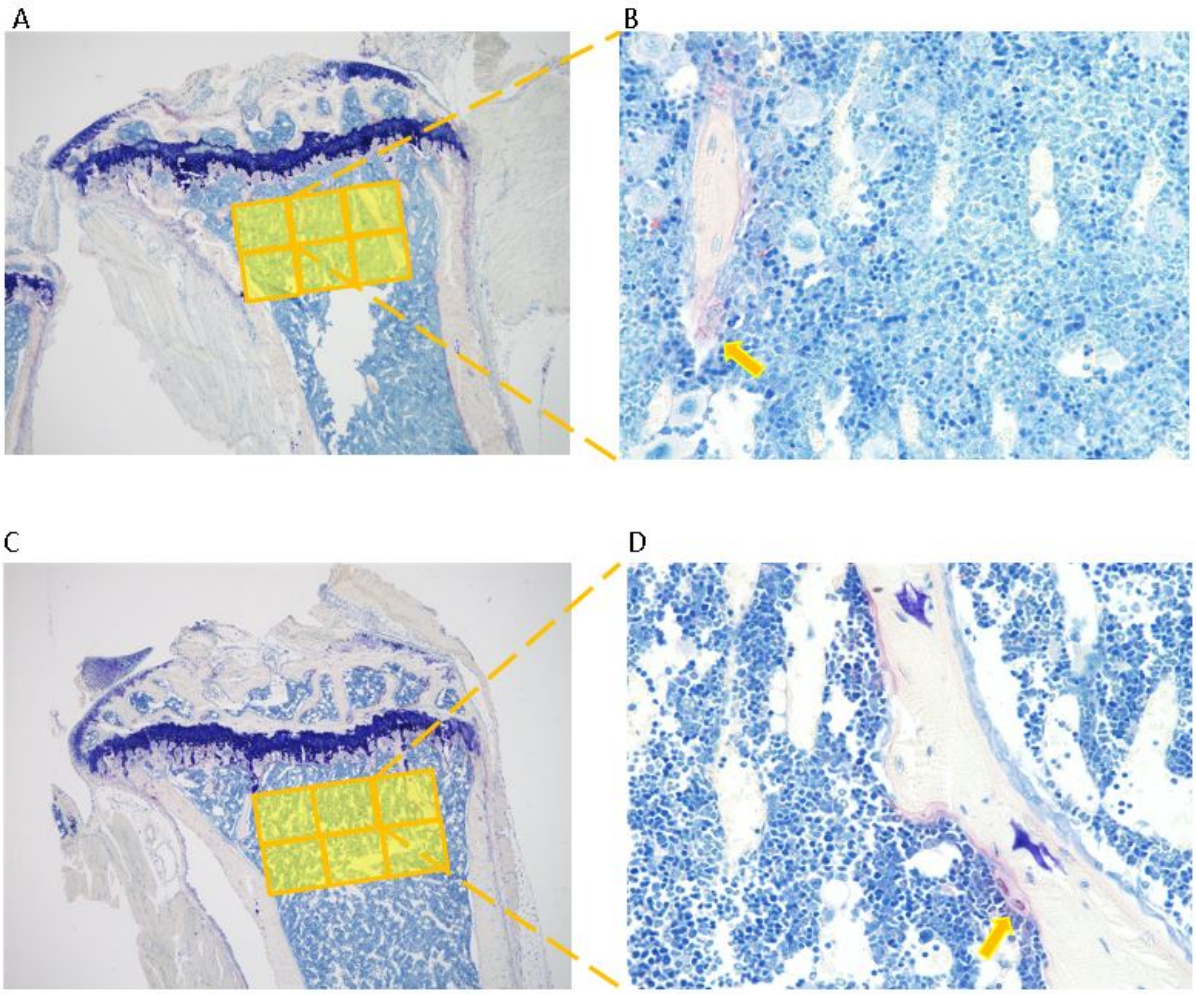

Figure 16. Regions of interest for osteoclast counting via TRAP staining. A (Sham) and C (OVX) show the entire area counted (at 4X), which is 150 um distal to the proximal growth plate, marked into 6 areas, each 50 x 50. B (Sham) and D (OVX) show one of the six regions counted (at 20X), with an arrow pointing to an osteoclast.

Backscatter Scanning Electron Microscopy

Lacunar area was measured following backscatter electron microscopy of the right tibia. Images were taken 100 mm proximal to the end of the medullary cavity. Six images were taken per bone, three consecutive images anterior of the medullary cavity and three consecutive images posterior of the medullary cavity. Total lacunar area was counted using Image J and top 20% largest lacunar area was also figured. Both data sets did not meet normalcy and are reported as medians with IQR. Total lacunar number was consistent between the two groups (Sham = 707; OVX = 684) and total lacunar area (fig. 17A) was not significantly different (Sham = 31.33; 20.33, 43.91; OVX = 29.09; 18.90, 44.44; p = 0.1753). The top 20 percent largest lacunae (fig. 17B) were also tested for significance, but showed none (Sham = 64.55; 55.94, 78.41; OVX = 64.58; 55.85, 75.14; p = 0.6535). A reference image and one of the six images used in counting is in figure 18.

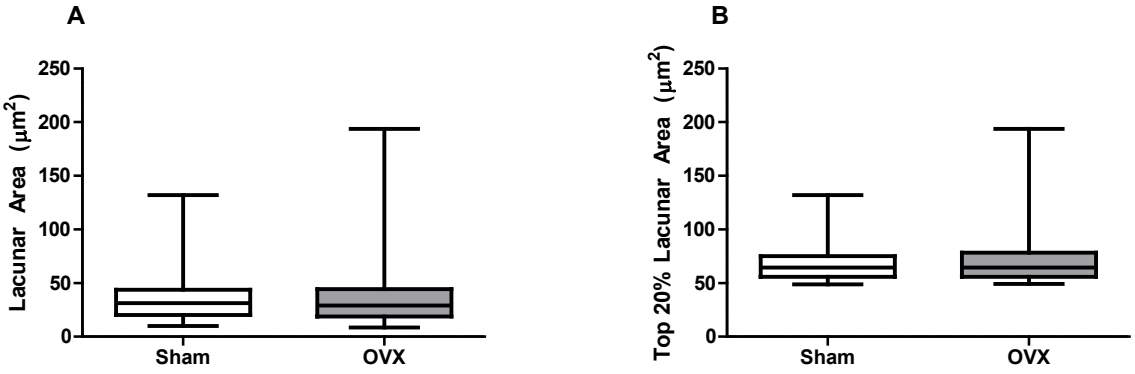

Figure 17. Lacunar area is unchanged after OVX. Total lacunar area (A) and (B) top 20% largest lacunar areas. (n = 3; no significant differences).

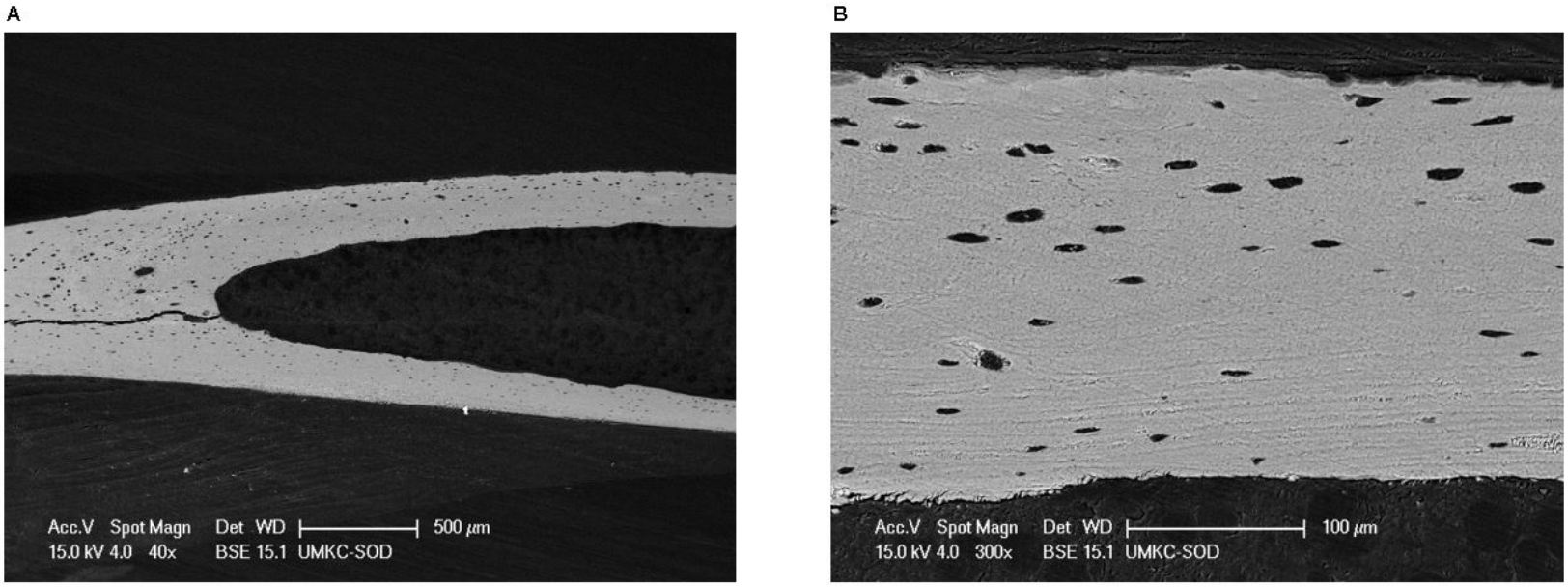

Figure 18. Backscatter scanning electron microscopy of lacunar area. A reference image was first taken (A) and 6 total images were taken 100mm proximal to the end of the medullary cavity, 3 on the anterior side and 3 on the posterior side. A representation of one of those 6 images is in B.

High-Resolution MicroXCT

Plastic embedded right tibiae (4 Sham and 4 OVX) were cut into 300μm thick sections, 3mm proximal to the tibia/fibula junction, and the tibiae were imaged for lacunar volume on both the medial and lateral bone sides. Dr. Mohammad Akhter, at the Creighton University Osteoporosis Research Center, obtained measurements of lacunar volume, lacunar-void-volume, and lacunar-void-volume/bone tissue. The top 20% largest lacunar-void-volumes were also figured. Lacunar number and lacunar-void-volume/bone tissue data had a normal distribution and are reported with means ± SD, while lacunar-void-volume and top 20% are reported with medians and IQR due to non-normal data distribution.

While there was a downward trend for the OVX group in lacunar number and lacunar-void-volume/bone tissue ratio, neither were significant ($p = 0.4127$; $p = 0.6393$). Lacunar-void-volume and the top 20% largest lacunar-void-volumes were slightly higher in the OVX group; however, neither showed a significant difference from the Sham group ($p = 0.4857$; $p = 0.2000$). Results of high-resolution microXCT are reported in table 7 and figures 19 and 20.

TABLE 7

HIGH-RESOLUTION MICROXCT

	Lacunar Number	Lacunar-Void-Volume	Top 20% Lacunar-Void-Volume	Lacunar-Void-Volume/Bone Tissue
Sham	41965±8625	210.9 (139.3-226.0)	444.6 (332.9-474.5)	0.008994±0.001934
OVX	36861±14767	228.1 (204.6-231.4)	474.4 (447.6-480.8)	0.008246±0.003972

*(n = 4; No significance for any parameter)

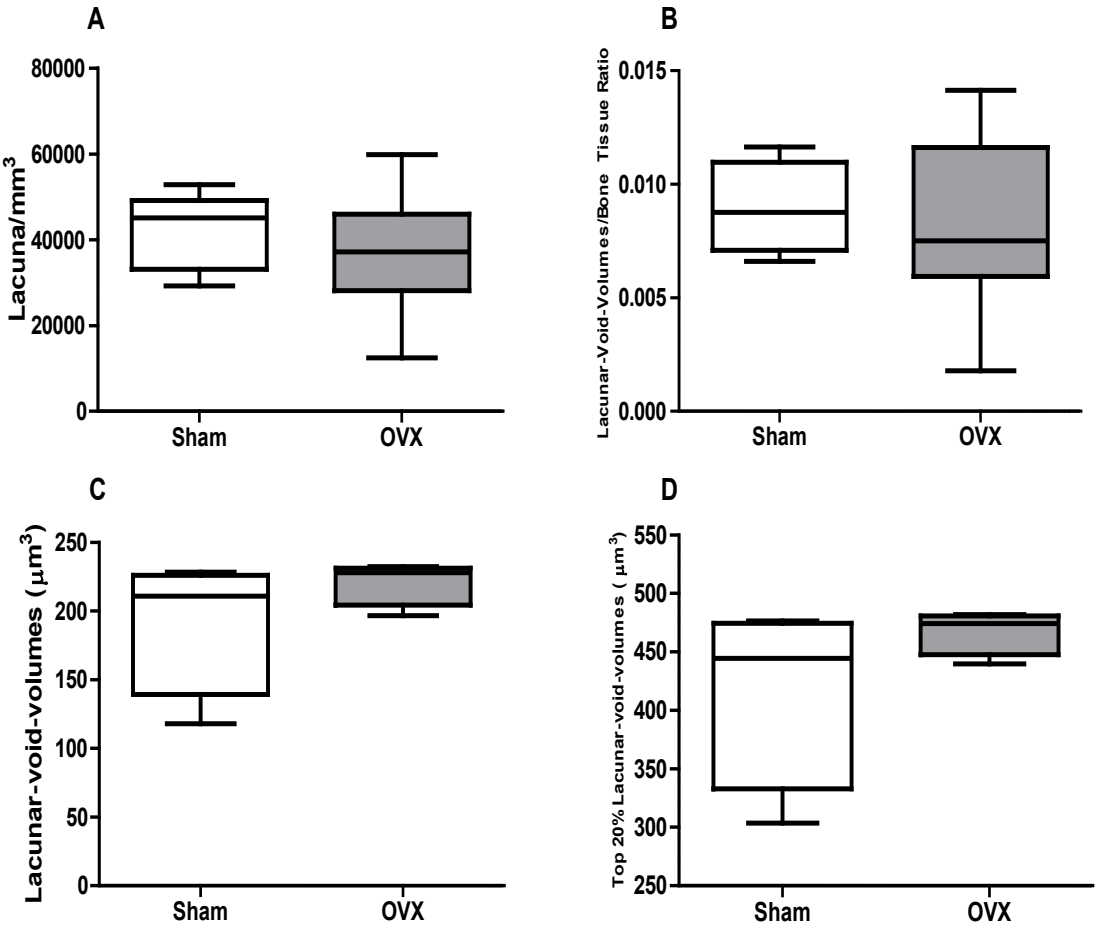

Figure 19. Lacunar number, volume, and density is unchanged after OVX. (No significance for any parameter; n = 4).

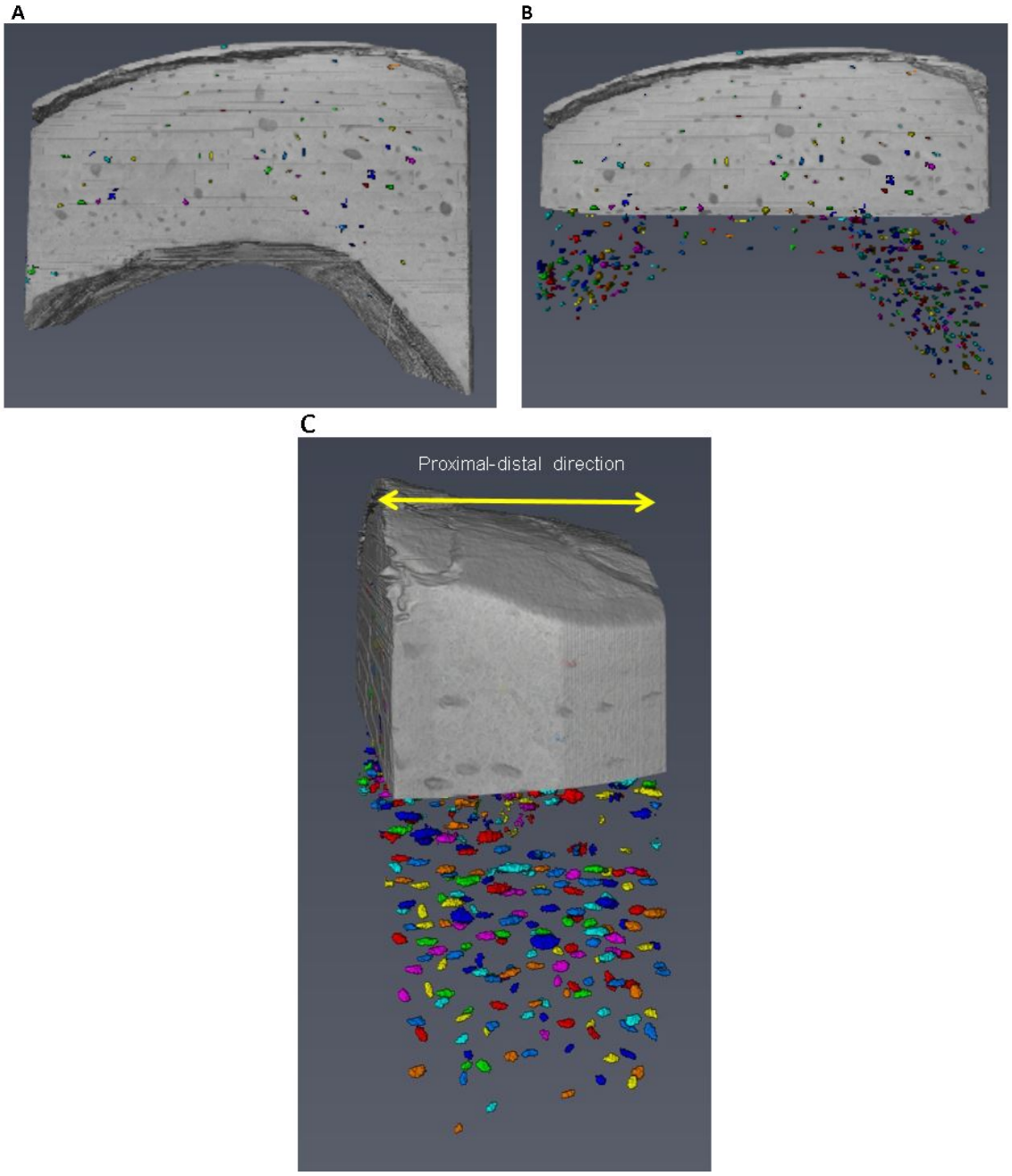

Figure 20. Representative images of high-resolution microXCT. All images taken with Avizo (9.4v) software analysis at 40X with 0.6µm resolution (showing lacunar voids between 50 to 600µm^3, with colors to facilitate viewing voids only). A and B show voids on the medial side of the cortical section, with B having a part of the mineral removed to show lacunar voids only. C also has mineral removed and shows voids on the medial side of the cortical section from a proximal to distal view.

In Vitro Cell Culture Model

Characterization of MLO-Y4 in Charcoal Stripped Serum

Before subsequent experiments with MLO-Y4 cells, I first assessed the growth of these cells when grown in charcoal stripped serums. Three experiments were conducted for this morphologic characterization, as described in the methods section. Typical MLO-Y4 cell morphology consisted of a flattened, expanded cell body with multiple, widened dendritic projections (Kato et al. 1997), while atypical cells had a shriveled, condensed cell body, with multiple, thin dendritic projections. Using crystal violet stains, normal cells typically had a lighter staining cytoplasm with a visible nucleus, while abnormal cells had a darker stained cell body, with no discernable nucleus.

First, cells were plated on collagen coated glass microscopic slides grown in phenol red free media with 2.5% of stripped FBS and CS each for 48 hours. As shown in figure 21A, cells were mostly normal in shape and size when they were grown at a lower cell density (at the edges of the slide); however, cells under the same condition showed more altered morphology in a more dense environment (at the center of the slide) (fig. 21B). The media on cells was changed to 0.1% of stripped FBS and CS each for either 1 hour or 2 hours. Regardless of location on the slide, both time points showed altered cell morphology (fig. 21C-F).

Second, MLO-Y4 cells were examined for their morphology in phenol red free media with different percentages and combinations of stripped FBS and CS serums. Growth and morphology of these cells were compared against MLO-Y4 cells grown in regular media supplemented with 2.5% of both serums, non-stripped. Cell growth was assessed at the periphery and center of the slide at time points of 4, 24 and 48 hours for all percentages and combinations (fig. 22-29). Again, cells in a less dense area were more apt to have normal morphology, especially at the 4 hour time point. Cells in the first 4 hours mostly had typical morphology, regardless of media or serum type/amount. As cell density increased over time, so did the appearance of atypical morphological cells, with more atypical cells appearing at 24 hours and even more in the 48 hour time points. The amount of atypical cells increased

as serum levels decreased and with charcoal stripped serums. Cell morphology was most altered in high density areas with charcoal stripped serums for time periods longer than 24 hours.

Third, MLO-Y4 cells were examined for morphology following incubation in phenol red free media with 2.5% of each stripped serum, then placed into media with stripped serum concentrations ranging from 2.5-0.1% for 15 minutes and then back into the original media for another 15 minutes before harvesting. Cell morphology was analyzed at the edge and center of the slide. As serum concentration decreased, there was an increase in the number of atypical cells, especially at the center of the slide, where there is a higher cell density. Examples of typical and atypical cells are shown in figure 30. Analysis by western blot revealed ratios of pAKT/β-actin band intensity to be relatively equal for the 2.5% (5.69) and 1% (5.33), but decreased by almost half at 0.5% (2.50) and 0.1%.(2.29) at each serum concentration (fig. 31). Since there were not replicates, statistical analysis could not be performed.

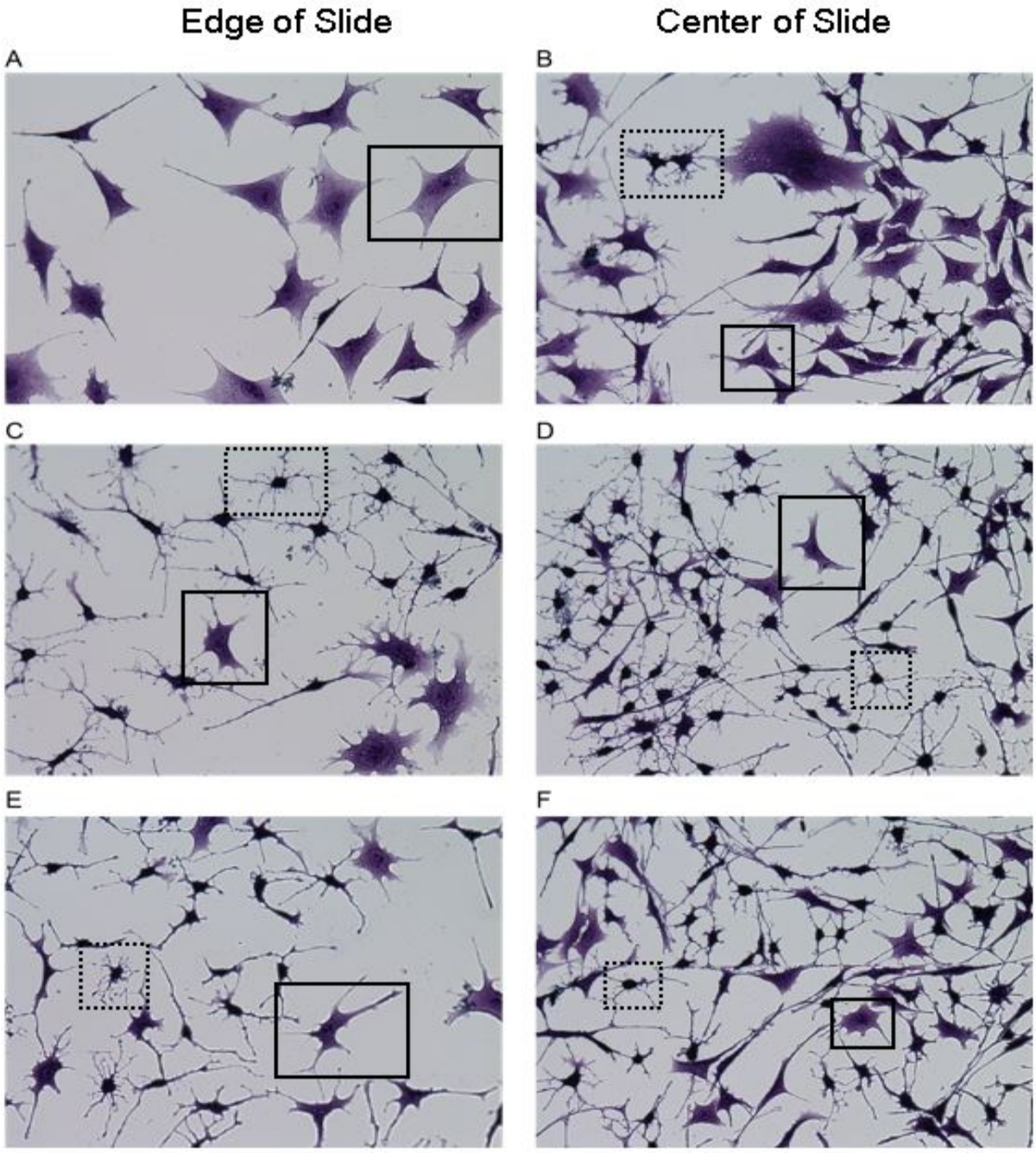

Figure 21. Atypical MLO-Y4 morphology increases in stripped and low growth serums. Cells grown in phenol red free media (PRF) with 2.5% charcoal stripped serums (CSS) for 48 hours (A and B). Media changed to 0.1% CSS and harvested at 1 hour (C and D) or 2 hours (E and F). Images at 20X. Typical cell morphology examples in solid boxes; atypical examples in dashed boxes. Notice the increasing number of atypical cells as cell density increases and as serum concentration decrease

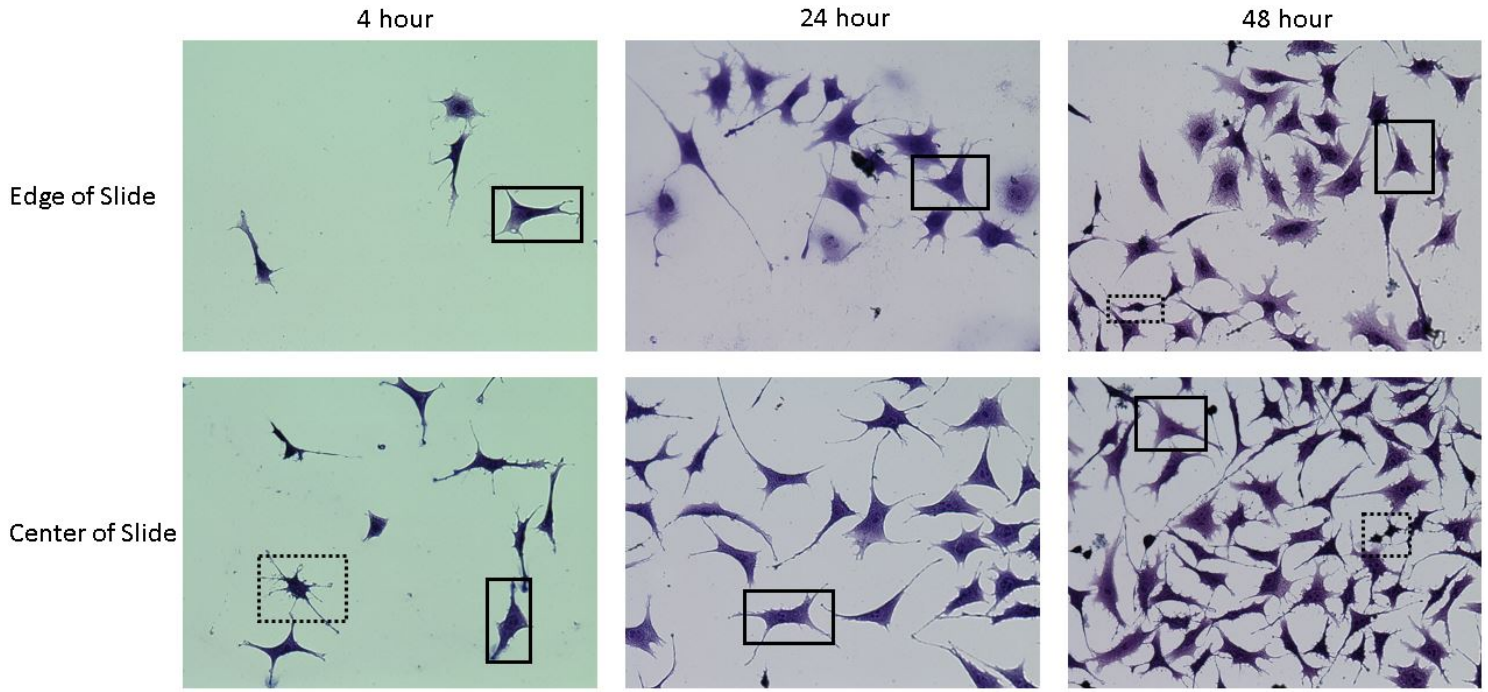

Figure 22. MLO-Y4 have typical morphology in unaltered growth media. Cells grown in regular α-MEM media with non-stripped 2.5% FBS and 2.5% CS. Notice the increased cell density at the center of the slide. Typical morphology cell examples in solid boxes; atypical cells in dashed boxes. All images at 20X.

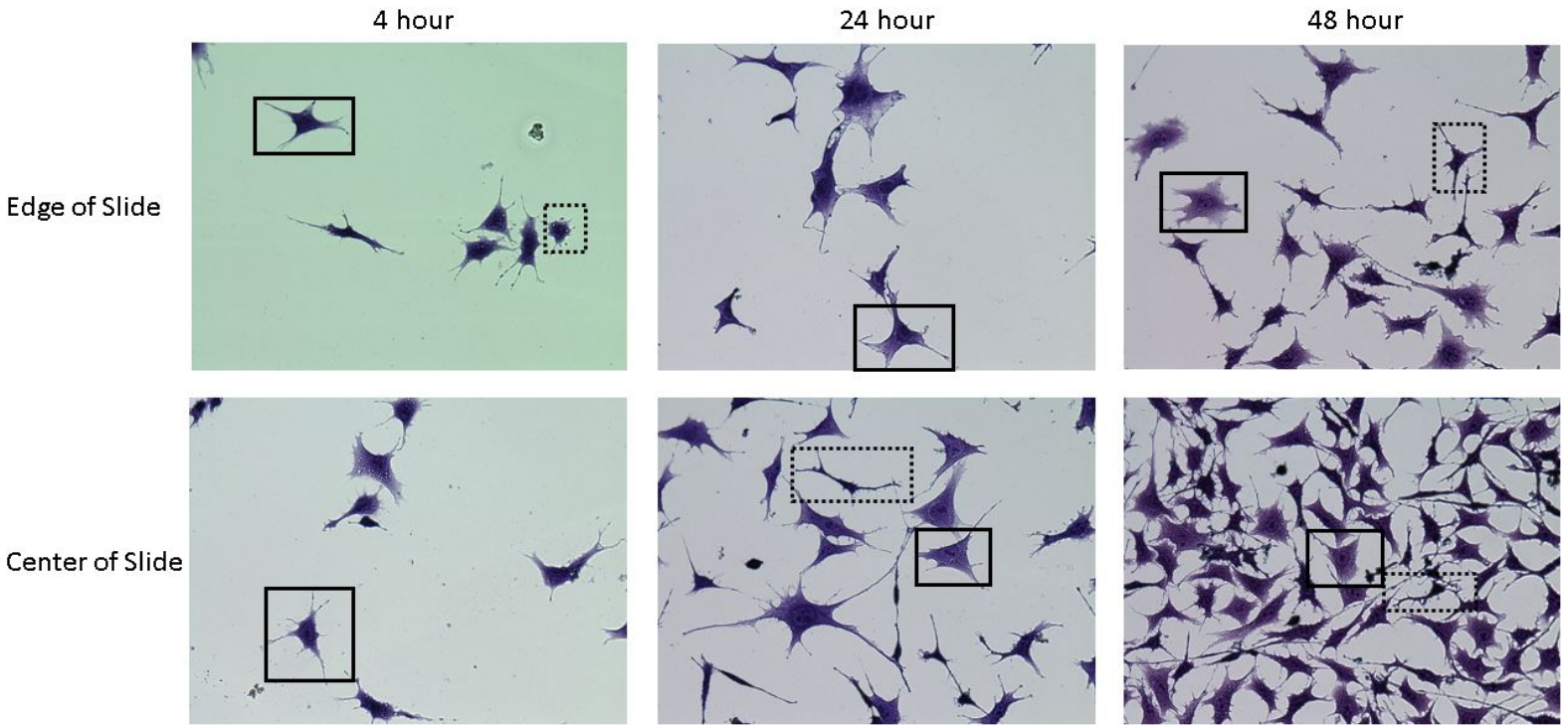

Figure 23. MLO-Y4 morphology begins altering in phenol red free media and 2.5% stripped serums. Media supplemented with stripped 2.5% FBS and 2.5% CS. Notice the increased cell density at the center of the slide. Typical morphology cell examples are in solid boxes, atypical morphology cell examples are in dashed boxes. All images at 20X.

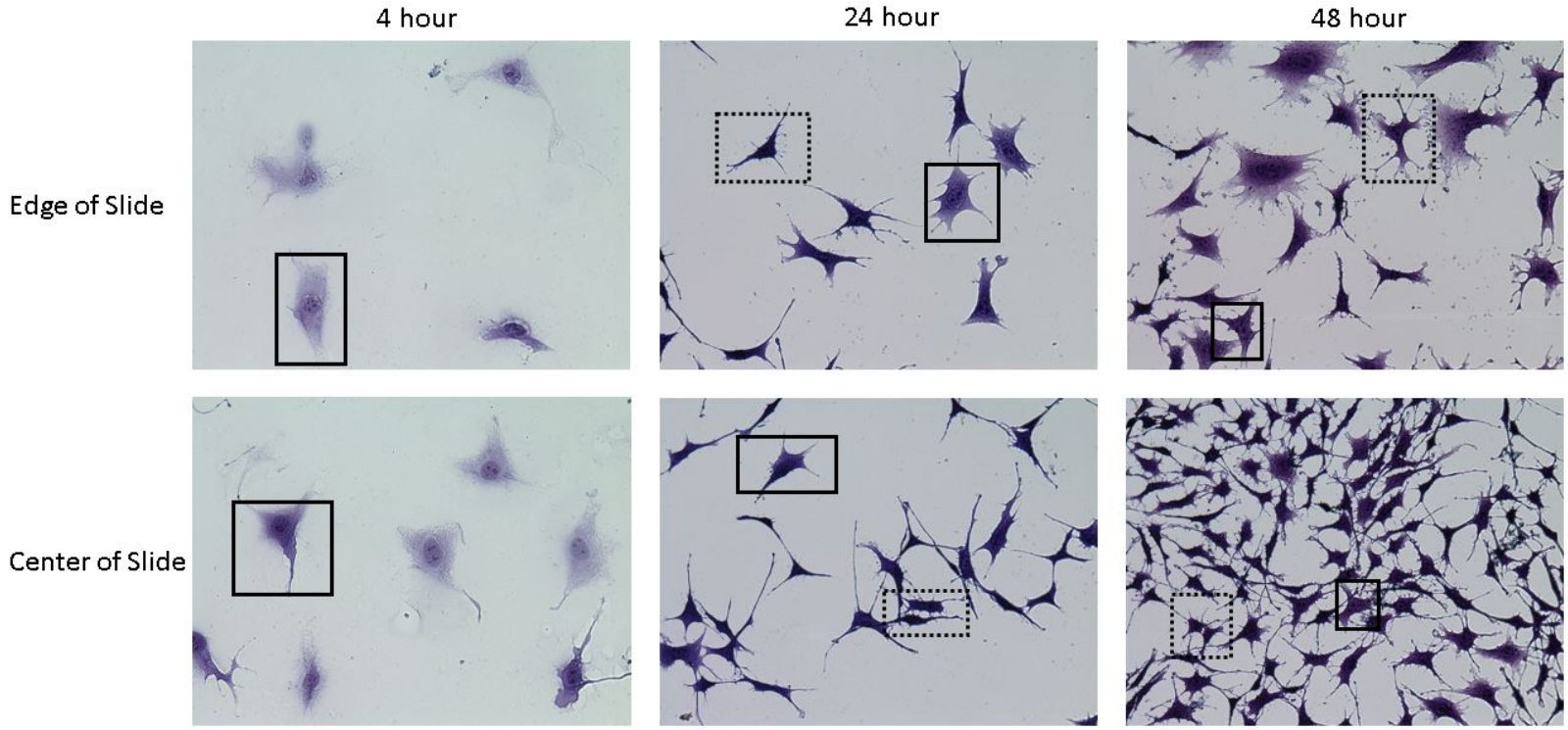

Figure 24. MLO-Y4 morphology alters past 24 hours in phenol red free media with stripped 2.5% FBS and 1.0% CS. Notice the increased cell density at the center of the slide. Typical morphology cell examples are in solid boxes; atypical morphology cell examples are in dashed boxes. Cells at 4 hours may be newly adhered. All images at 20X.

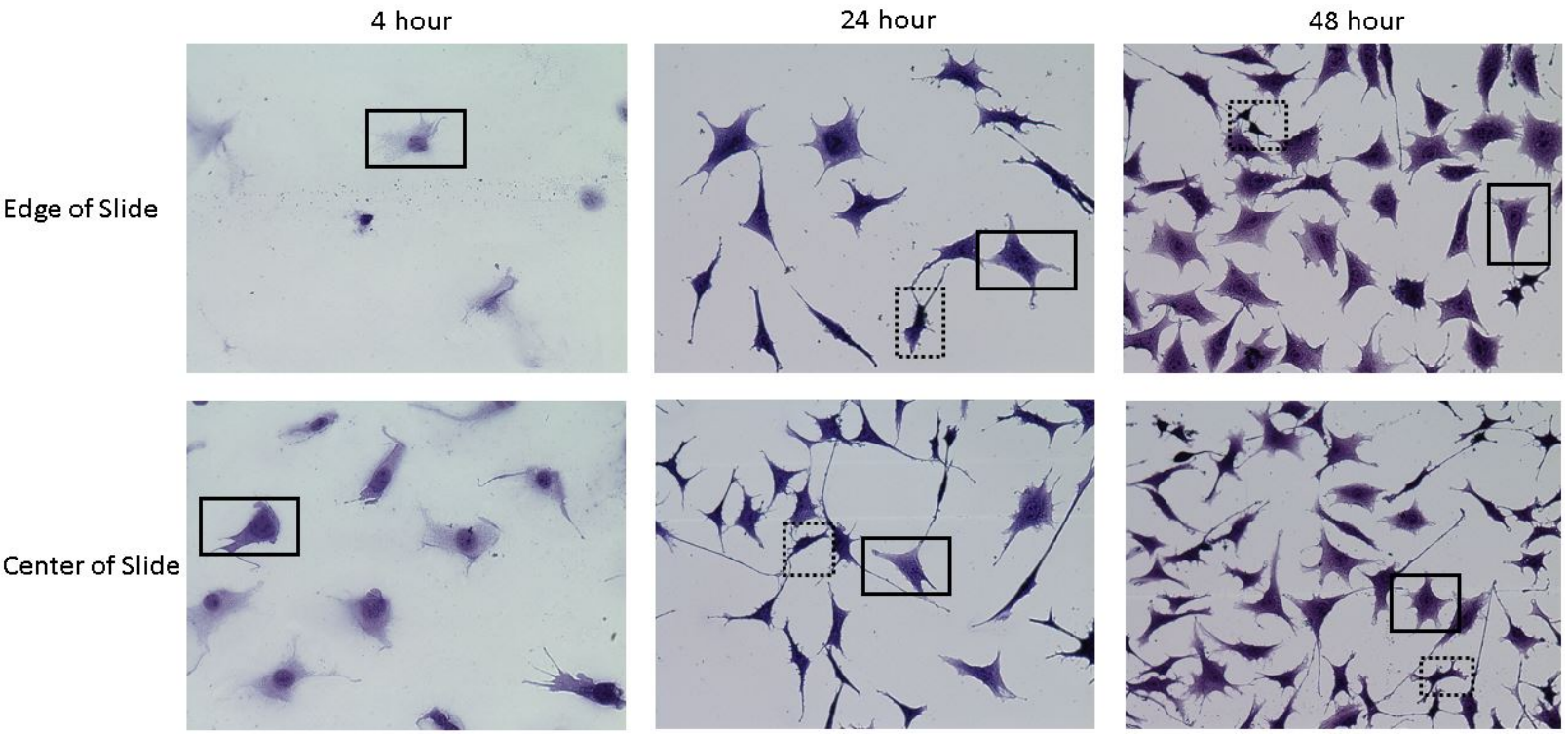

Figure 25. MLO-Y4 morphology alters past 24 hours in phenol red free media with stripped 2.5% CS and 1.0% FBS. Notice the increased cell density at the center of the slide. Typical morphology cell examples are in solid boxes; atypical morphology cell examples are in dashed boxes. Cells at 4 hours may be newly adhered. All images at 20X.

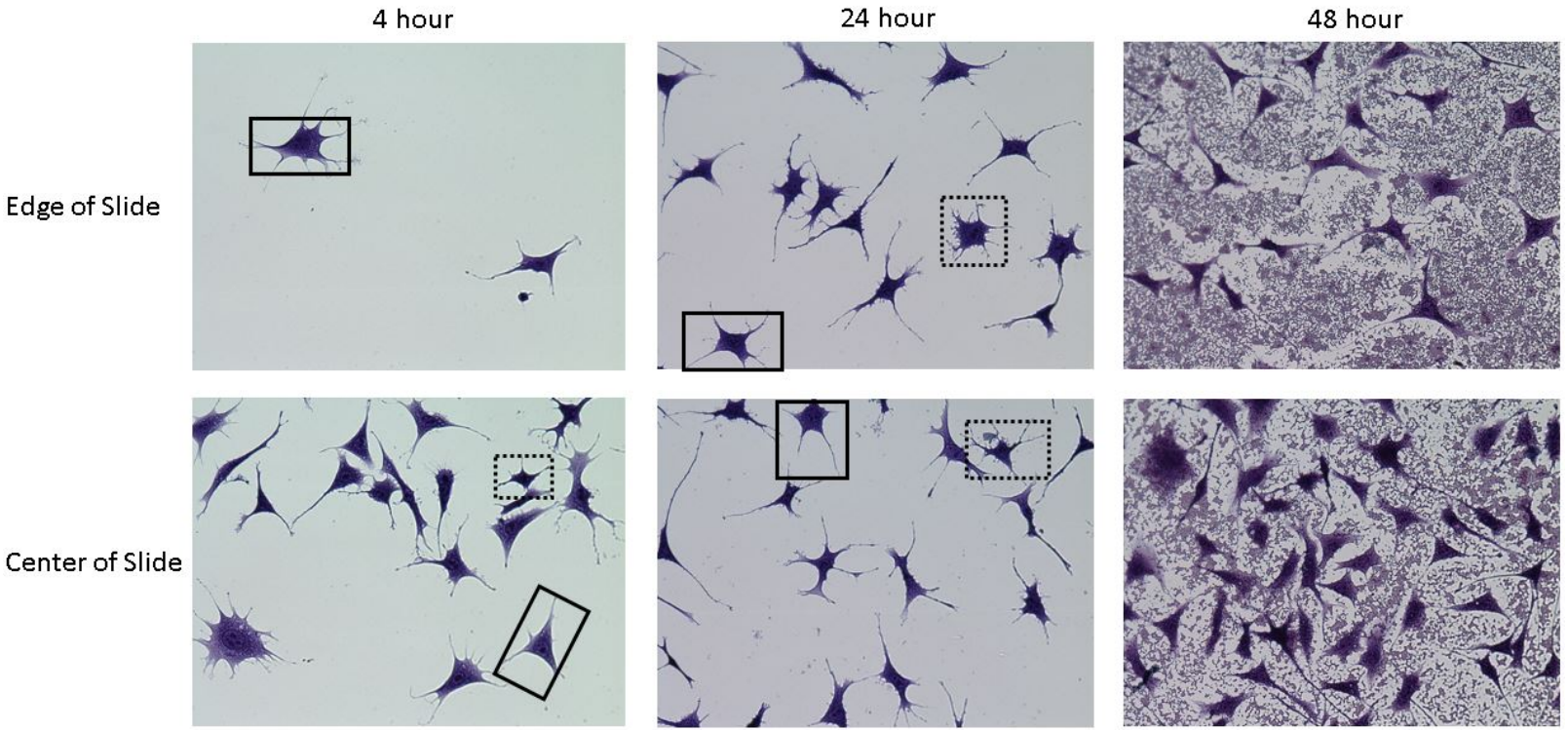

Figure 26. MLO-Y4 morphology alters at 4 hours in phenol red free media with stripped 2.5% FBS only. Notice the increased cell density at the center of the slide. Typical morphology cell examples are in solid boxes; atypical morphology cell examples are in dashed boxes. Both 48 hour slides had possible fungal contamination. All images at 20X.

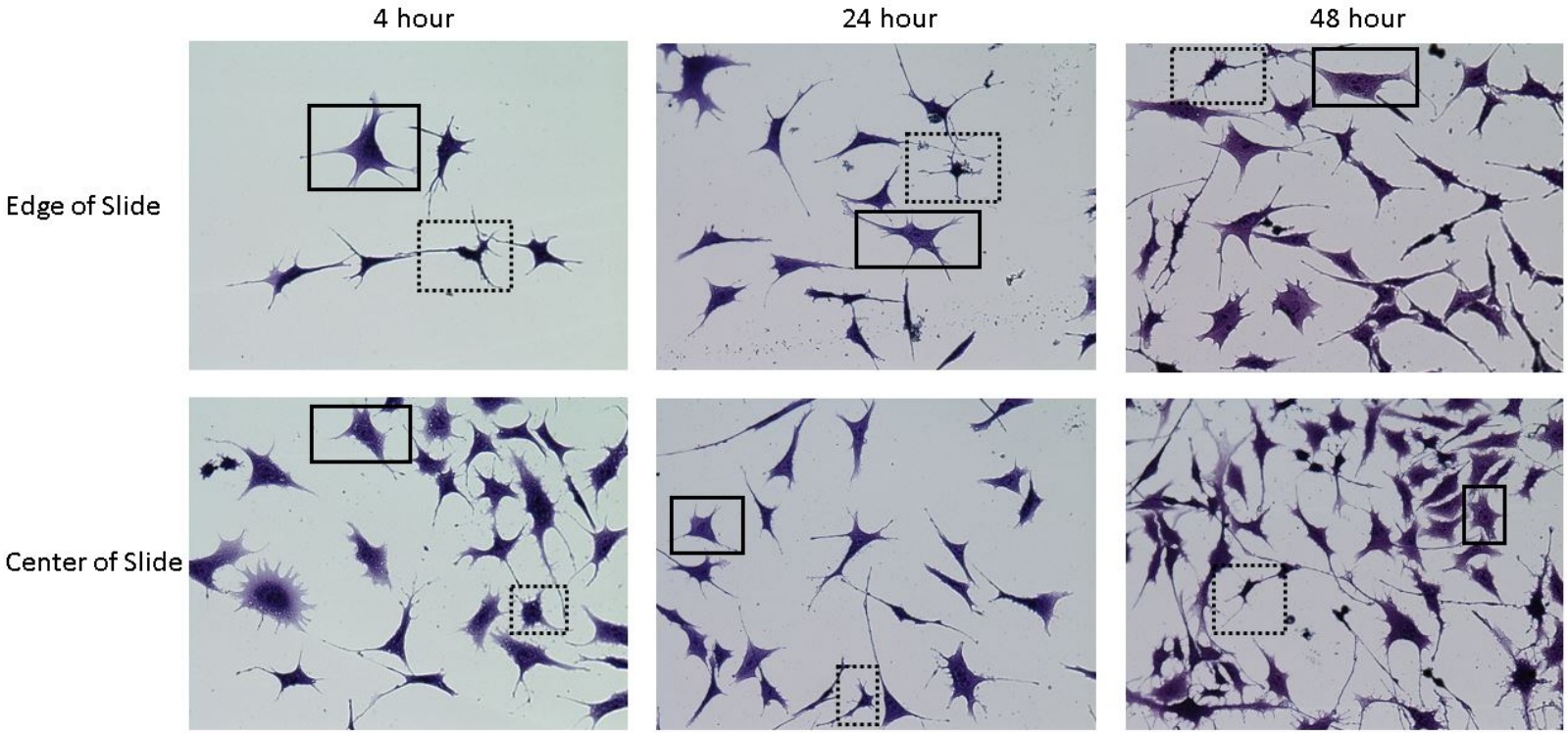

Figure 27. MLO-Y4 morphology alters at 4 hours in phenol red free media with stripped 2.5% CS only. Notice the increased cell density at the center of the slide. Typical morphology cell examples are in solid boxes, while atypical morphology cell examples are in dashed boxes. All images at 20X.

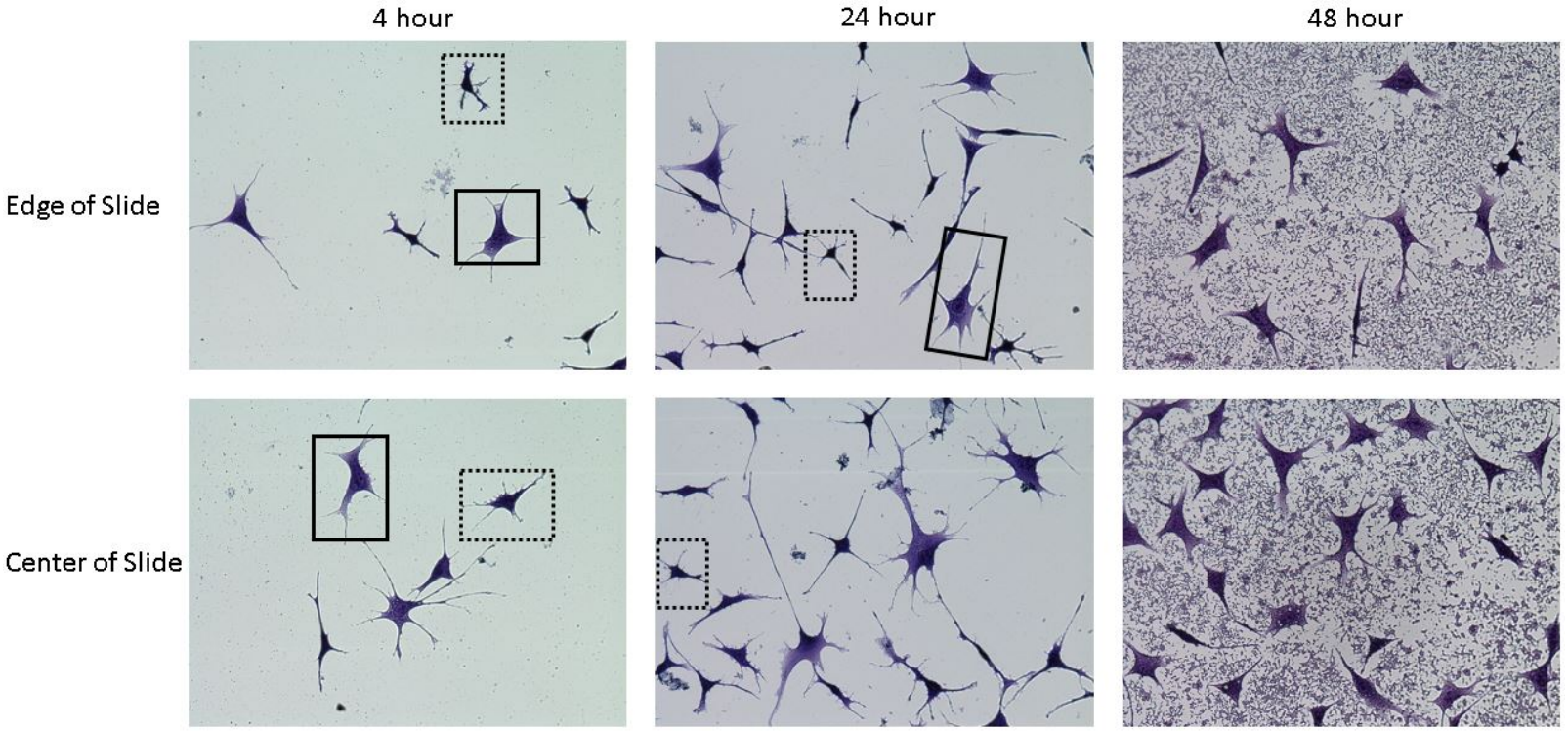

Figure 28. MLO-Y4 morphology alters at 4 hours in phenol red free media with stripped 1% FBS only. Notice the increased cell density at the center of the slide. Typical morphology cell examples are in solid boxes; atypical morphology cell examples are in dashed boxes. Both 48 hour slides had possible fungal contamination. All images at 20X.

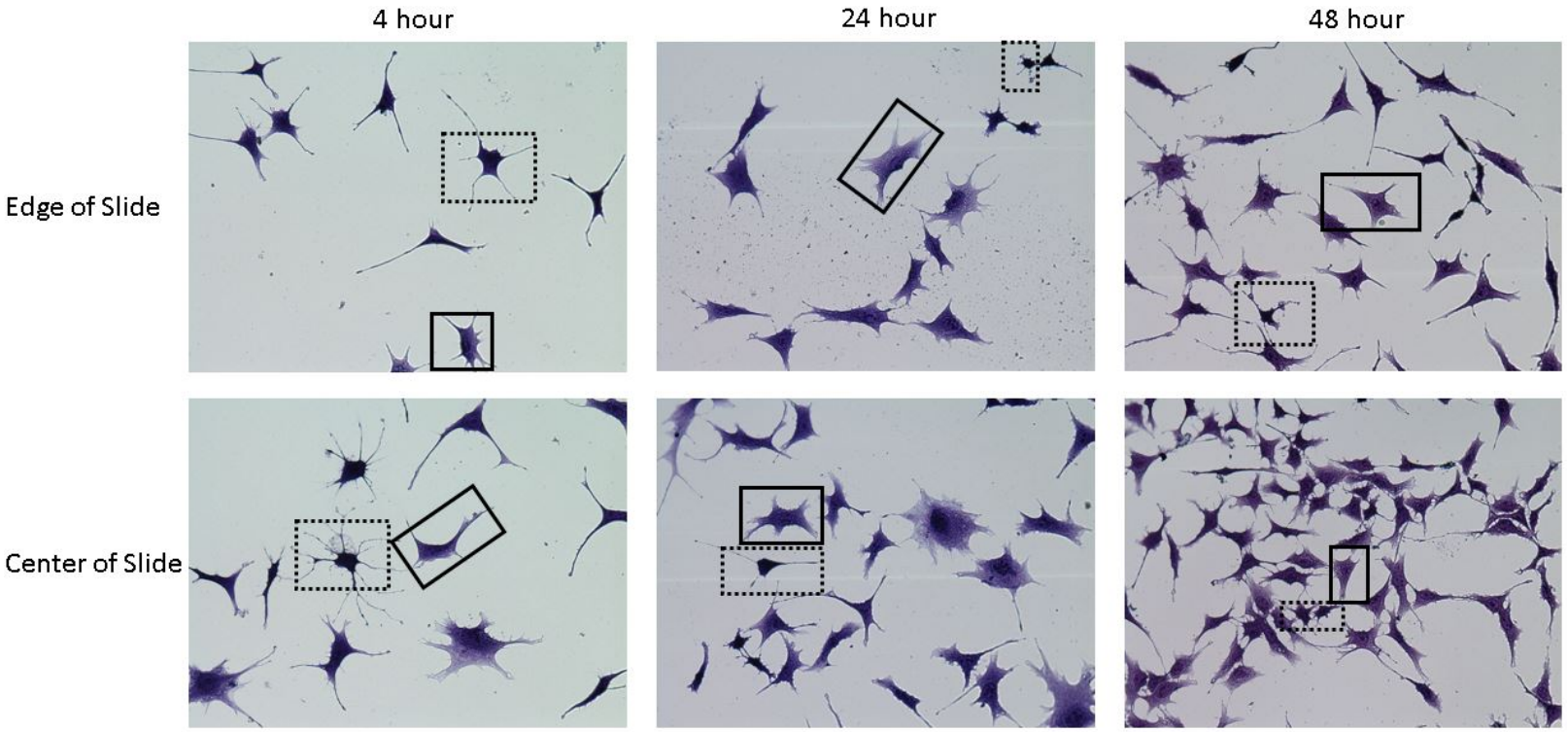

Figure 29. MLO-Y4 morphology alters at 4 hours in phenol red free media with stripped 1.0% CS only. Notice the increased cell density at the center of the slide. Typical morphology cell examples are in solid boxes; atypical morphology cell examples are in dashed boxes. All images at 20X.

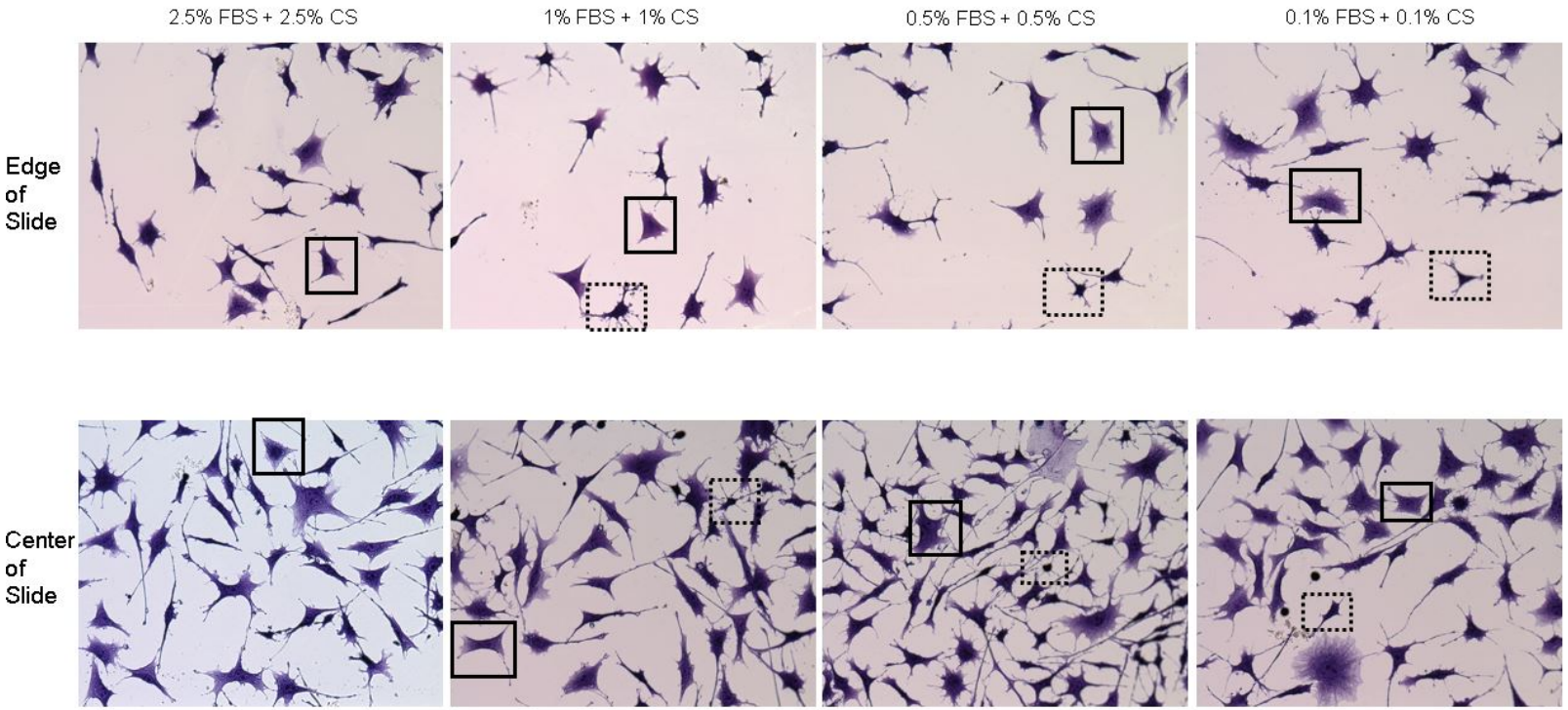

Figure 30. Morphology of MLO-Y4 cells after 15 minute exposure to low concentration stripped serum. All treatments used phenol red free media. Cells grown with 2.5% stripped serums for 24 hours before 15 minute exposure. Cells put back into original media for 15 minutes before harvesting. Examples of typical cell morphology are in solid boxes; atypical cell morphology are in dashed boxes. As serum concentrations decrease, there is a noticeable increase in atypical cells, especially at the center of the slide, where cell density is the highest.

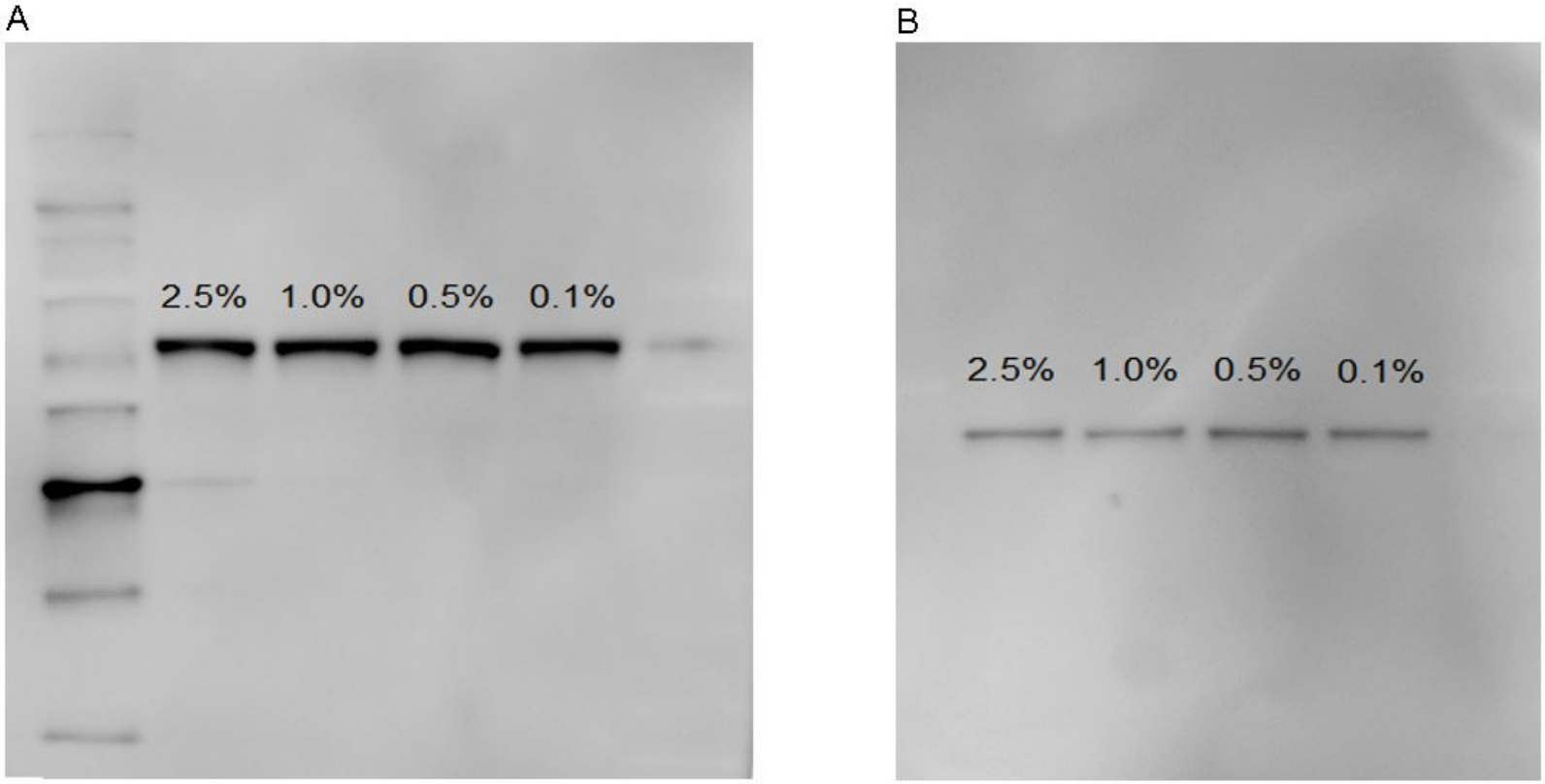

Figure 31. Phosphorylated Akt/β-actin decreases in MLO-Y4 cells after 15 minute exposure to low concentration stripped serum. All treatments used phenol red free media. Cells grown with 2.5% stripped serums for 24 hours before 15 minute exposure. Cells put back into original media for 15 minutes before harvesting. Phosphorylated Akt bands are shown in A, while β-actin bands are shown in B. Band intensity ratios of pAkt/ β-actin remained relatively constant between the 2.5% and 1.0% but decreased by almost half at the 0.5% and 0.1% serum concentrations.

TOPflash-MLO-Y4 Response to Wnt and Estrogen in Stripped Serum and Phenol red Free Media

In response to activation of β-catenin signaling the TOPflash-MLO-Y4 cells express luciferase which will convert an added substrate into light, which is quantitated by luminometry and expressed as counts per second (CPS), therefore the CPS is a reflection of reporter activity following treatment. Treatment groups included regular media or phenol red free media, supplemented with complete serums or stripped serums with ±Wnt3a and ± 17β-estradiol (referred to as E in graphs). TOPflash-MLO-Y4 cells respond to Wnt3a in stripped serum and phenol red free media, although the response is slightly diminished from other groups. The Wnt positive groups showed elevated CPS when normalized to the control group (regular media with complete serums and no Wnt) (fig. 32). When 17β-estradiol was added, in the absence of Wnt, there was a slight increase in β-catenin signaling compared to the Wnt negative groups, but not nearly the response seen by the addition of Wnt alone (fig. 33); however when Wnt and 17β-estradiol were added simultaneously, there was not a synergistic effect on β-catenin signaling (fig. 32). In the +Wnt+E groups, there was a diminished response in both of the stripped serum groups compared to their complete serum counterparts. It was not possible to determine if these changes in CPS were truly statistically significant since the data were not normalized to total number of cells (or total DNA) for each group (equal numbers of cells were initially plated for this experiment, but only counts per second were obtained from the luciferase assay).

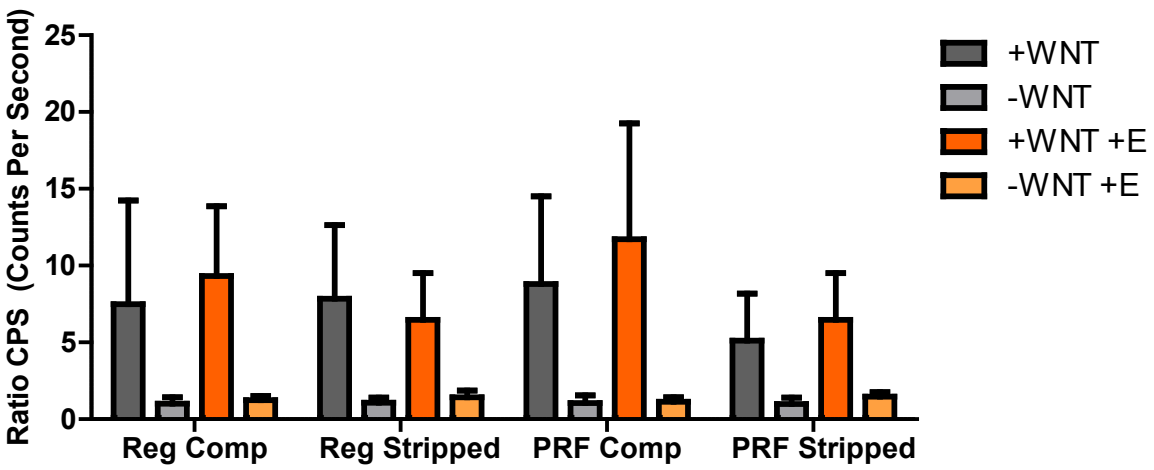

Figure 32. TOPflash-MLO-Y4 respond to Wnt3a but not 17β-estradiol. Cells grown in regular and phenol red free media with complete or stripped serums. Growth with 17β-estradiol and Wnt3a together had no synergistic effect. (n = 9-21 depending on group).

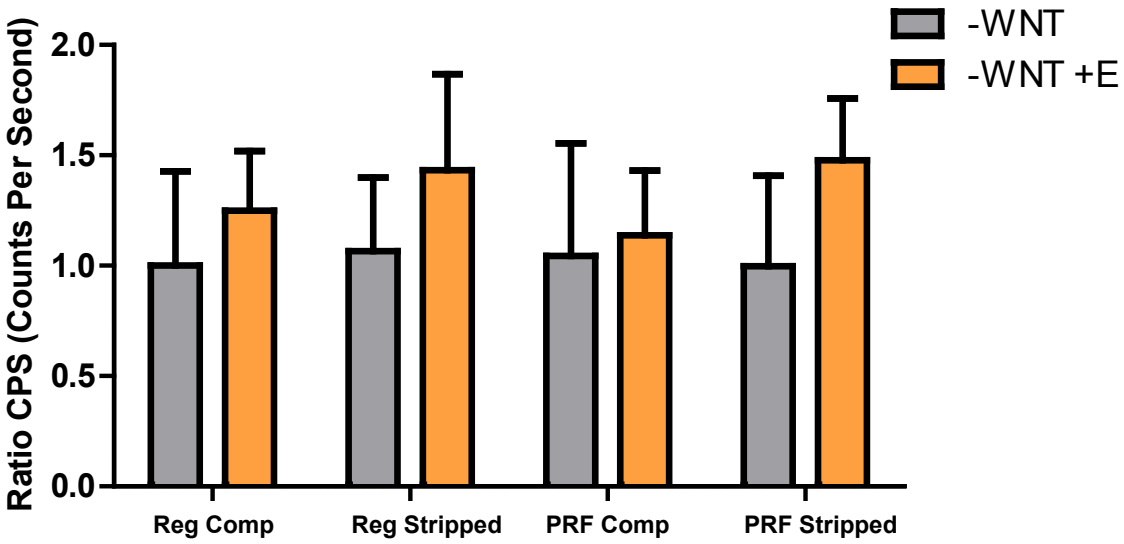

Figure 33. TOPflash MLO-Y4 lack a robust response to 17β-estradiol only. Cells grown in regular and phenol red free media with complete and stripped serums. The addition of 17β-estradiol did not elevated CPS in a similar manner as Wnt3a alone. (n = 9-21 depending on group).

TOPflash-MLO-Y4 Estrogen Receptor (ER)α/β
Polymerase Chain Reaction (PCR)

TOPflash-MLO-Y4 cells were grown in phenol red free media with 2.5% of regular FBS and CS serums each. All cells were plated in 6-well plates at same start time. Cells without 17β-estradiol were harvested at 4, 8 and 24 hours. 17β-estradiol was then added to remaining wells and harvested again at the same time points. Following the first 8 hours after plating, levels of ERα declined. Between the 8 hour and 24 hour time points, ERα levels rapidly increased. Following the addition of 17β-estradiol, levels again declined for the first 8 hours, but then again began increasing (fig. 34A). Levels of ERβ did not follow a similar pattern. Instead, they oscillated for the first 24 hours without 17β-estradiol, but following the addition of 17β-estradiol, levels declined and stayed relatively low (fig. 34B).

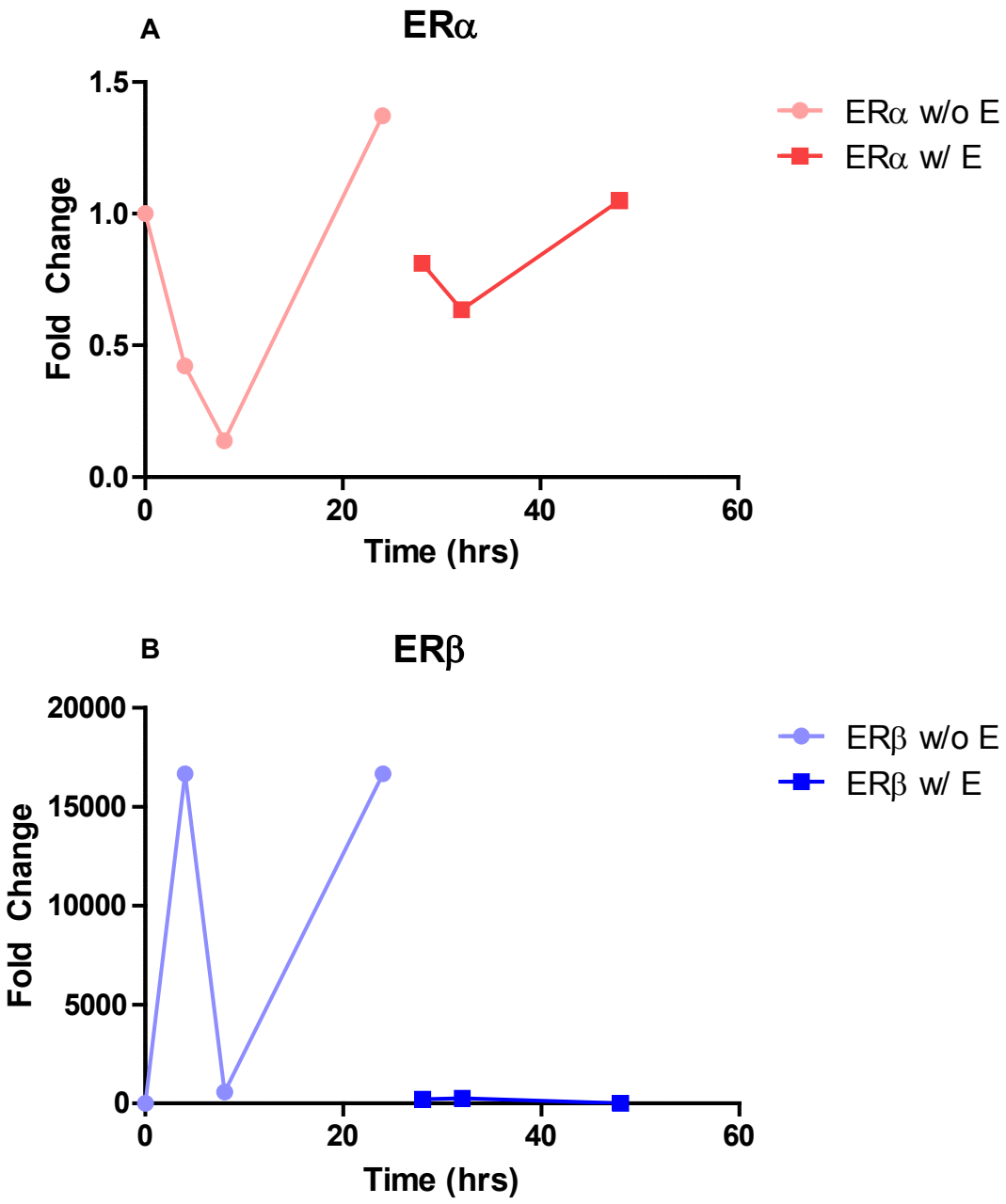

Figure 34. ERα levels increase after 17β-estradiol exposure, but ERβ levels decrease. Replicate wells used at each time point. Cells grown in phenol red free media with regular serums. Hours represent total growth time. Lines with circles represent harvesting times prior to 17β-estradiol addition. Lines with squares represent harvesting times following 17β-estradiol addition.

TOPflash-MLO-Y4 Estrogen and ERα Inhibitor (ICI)

TOPflash MLO-Y4 cells treated with ±Wnt3a, ±ICI, ±17β-estradiol and combinations of each, showed a significant impact of Wnt3a treatment when tested for CPS normalized to DNA amount. There was a significant difference ($p < 0.001$) between all Wnt3a positive groups, regardless of other treatments, (38.63 ± 1.03) versus all Wnt3a negative groups, regardless of other treatments (1.03 ± 0.45) (fig. 35A). There was not a significant difference in the CPS/DNA ratios across the three treatment groups (+17β-estradiol, +ICI, and +17β-estradiol and ICI) in either Wnt3a positive ($p = 0.113$) or Wnt3a negative ($p = 0.837$) groupings (fig. 35B and C).

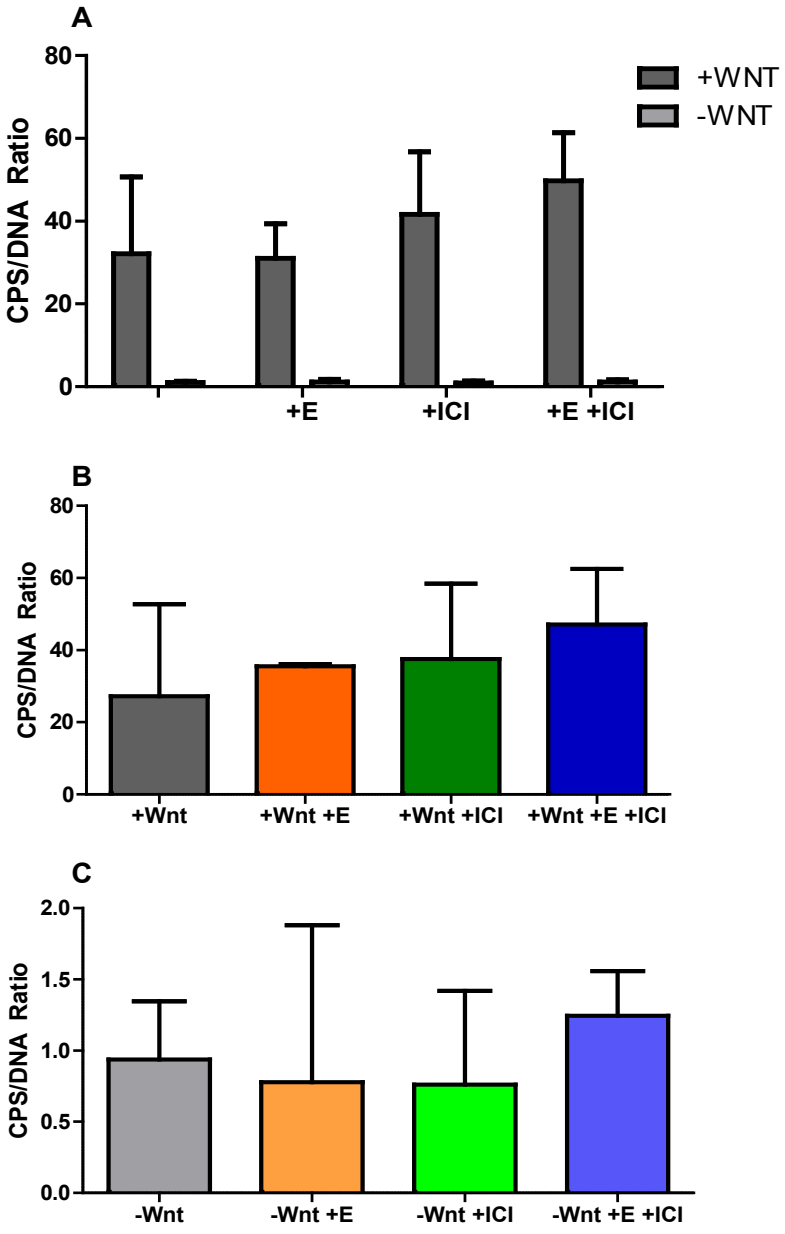

Figure 35. TOPflash-MLO-Y4 cells respond to Wnt3a, but not 17β-estradiol and ICI when applied simultaneously. Combining all Wnt positive groups resulted in a significant difference from all combined Wnt negative groups ($p < 0.001$). However, there were no significant difference between treatment groups within the Wnt positive ($p = 0.113$) or Wnt negative groups ($p = 0.837$). ($n = 3$).

TOPflash-MLO-Y4 ICI Pretreatment without Fluid Flow Sheer Stress (FFSS)

Two experiments were utilized to determine effects of pretreatment with ICI followed by secondary treatments with 17β-estradiol and Wnt3a. The first experiment was used to determine appropriate 17β-estradiol concentrations following ICI pretreatment. The second experiment had ICI pretreatment followed by secondary treatment with groups of ±Wnt 3a, ±17β-estradiol, and ±ICI, and combinations of each to determine effects of these treatment combinations prior to running the same conditions with FFSS.

It was necessary to determine the appropriate concentration of 17β-estradiol to use in the 24 hours following ICI pretreatment. Cells were grown with 100nM ICI in phenol red free media with 2.5% of regular FBS and CS each for 24 hours. Then treatments of ±Wnt3a, and Wnt3a with 17β-estradiol concentrations of 10^{-6}, 10^{-7}, 10^{-8} and 10^{-9} were added to cells for another 24 hours. The only significance between Wnt3a +17β-estradiol treatment groups was between the 10^{-7} and 10^{-9} concentrations ($p = 0.027$). No other concentrations were significantly different from each other or from the Wnt positive group, although 10^{-6}, 10^{-7}, and 10^{-8} had means slightly higher than Wnt alone. Since concentrations of 10^{-6} and 10^{-7} and 10^{-8} were not significantly different from each other, 10^{-6} was chosen for further experiments. All data are reported in figure 36 and table 8.

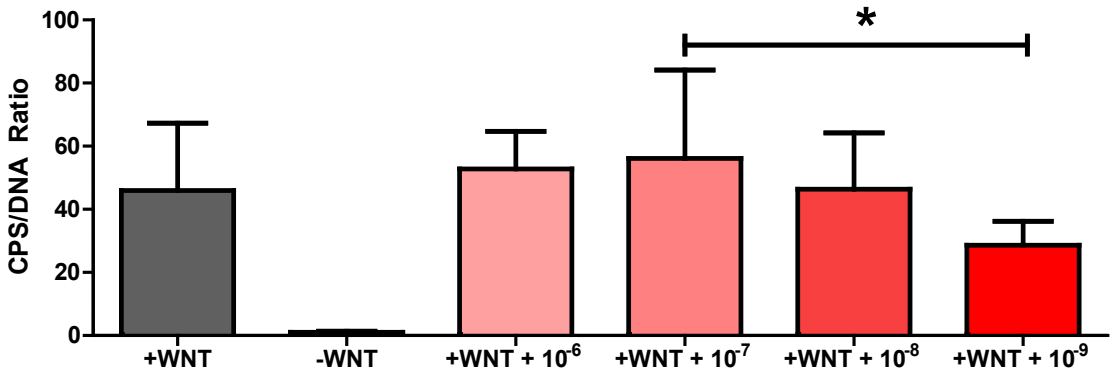

Figure 36. TOPflash-MLO-Y4 respond better to higher 17β-estradiol concentrations. Only 10^{-7} and 10^{-9} concentrations showed a significant difference. (n = 9; *p = 0.027).

TABLE 8

17β-ESTRADIOL CONCENTRATION DOSE RESPONSE

+Wnt	-Wnt	+Wnt +10^{-6}	+Wnt +10^{-7}*	+Wnt +10^{-8}	+Wnt +10^{-9}*
45.96 ±21.34	1.0 ±0.35	52.78 ±11.90	56.09 ±28.04	46.34 ±17.85	28.64 ±7.55

*(n = 9; *p = 0.027)

The final experiment utilized 24 hours of of ICI pretreatment (100nM) followed by 24 hour incubation with combinations of ±Wnt, ±17β-estradiol (10^{-6}) and ±ICI (100nM). Within the ICI pretreatment groups, there was a significant difference between groups; however, those differences only existed between secondary treatments in which one group included Wnt and the other did not ($p < 0.05$) None of the groups that both had Wnt as part of the secondary treatments showed significance between each other. The same is true when looking at the groups that did not receive ICI pretreatment, with the only significance being between secondary treatments in which Wnt was included in one group but not the other ($p < 0.05$). When looking at comparisons between groups in the categories of ICI pretreatment and non-pretreatment, again, the only time significant differences were observed were between groups where one involved Wnt in the secondary treatment and the other did not ($p < 0.05$) (fig. 38). However, while not significant, the ICI pretreatment group with Wnt3a and 17β-estradiol as secondary treatments was lower than its counterpart that did not receive ICI pretreatment. While Wnt had an impact on the responsiveness of the cells, other treatments did not. Since the literature typically uses the pretreatment method, this was adopted for further experiments.

PCR of TOPflash-MLO-Y4 cells following 24 hours of 100nM ICI pretreatment and then 24 hours of incubation in Wnt3a, 17β-estradiol, Wnt3a and 17β-estradiol in combination, or no treatment revealed a decrease in ERα following treatment with ICI along, but increases in levels with pretreatments of ICI followed by Wnt3a, or Wnt 3a and estrogen together. Levels of ERβ are at or below control levels in all groups (fig. 37).

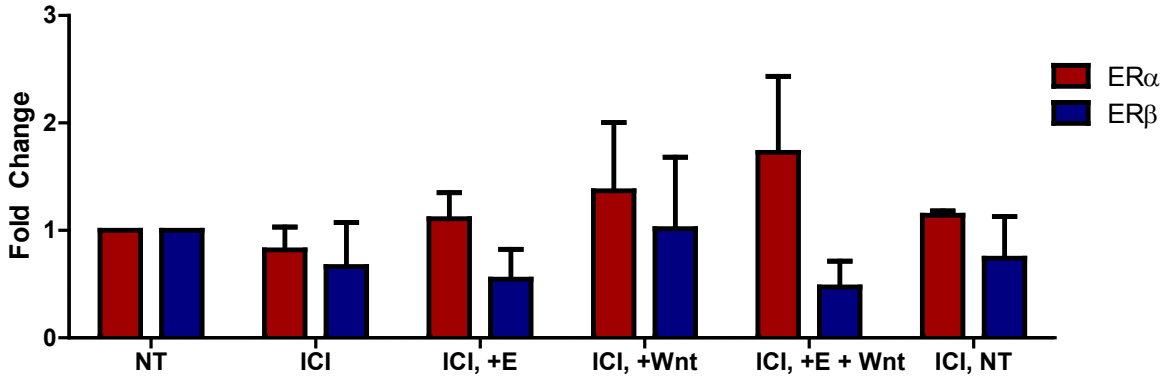

Figure 37. Levels of ERα and ERβ fluctuate dependent on treatments with Wnt3a, 17β-estradiol or ICI. The no treatment (NT) provides a baseline for comparison. Levels of ERα tended to decrease with ICI treatment, but increase for all treatments following ICI pretreatment, even when a secondary treatment is not applied (ICI, NT). Levels of ERβ tended to remain lower than the NT regardless of any pretreatment or secondary treatment. (n = 3).

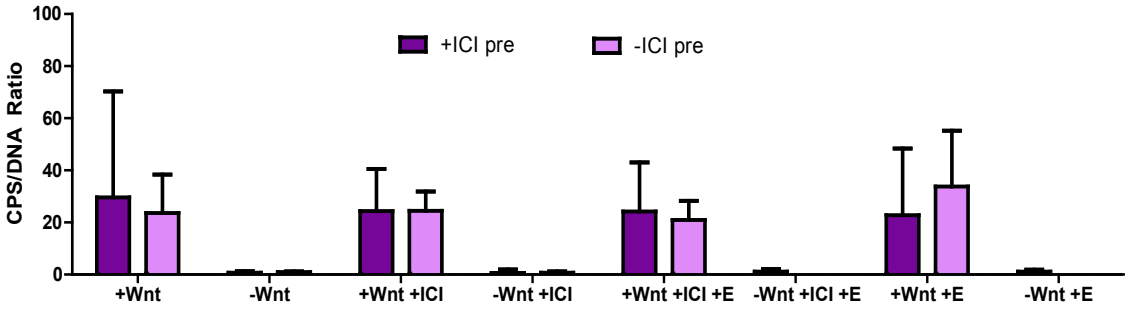

Figure 38. 24 hour static ICI pretreatment (pre) has no impact on second 24 hour treatment with Wnt3a, 17β-estradiol, ICI, or combinations. Wnt was the only significant treatment. At all comparisons, the Wnt groups were significantly higher than their corresponding non-Wnt counterparts. (n = 9-31, depending on group).

TOPflash-MLO-Y4 with FFSS

For FFSS on TOPflash-MLO-Y4 cells, it was necessary to determine the proper harvesting time post-FFSS. Activation of the Wnt/β-catenin pathway could be missed if cells were harvested too early or too late. The first experiment aimed to determine the appropriate harvest time. Cells were grown for 24 hours prior to FFSS in non-ICI pretreated phenol red free media and then subjected to 30 minutes of FFSS at 2 dynes or changed to fresh media for static controls. After 30 minutes, cells were put back into conditioned growth media ± Wnt and then harvested at 2, 4, or 24 hours.

Comparisons at the 2, 4 and 24 hour time point were made within the static group and the FFSS group, not considering different Wnt treatments. This allowed for comparisons of time only in each group. For static, there is a statistically significant difference in values between the 3 time points ($p = 0.035$). However, after adjustments for multiple comparisons, there were no significant differences, even though the 2 hour median value (0.42) was lower than the 24 hour median value (9.21) ($p = 0.055$). For the FFSS, the 2 hour median value (0.44) was statistically lower than the 24 hour median value (17.59) ($p = 0.001$). The overall trend for both FFSS and static groups were increasing CPS/DNA ratios at each time point (fig. 39). Comparisons were then made between the time points for each of the treatments (FFSS+Wnt, FFSS-Wnt, static+Wnt and static-Wnt). Neither of the Wnt negative treatments showed significance, regardless of FFSS or static. For the FFSS+Wnt, the 2 hour time point was significantly lower than the 24 hour time point ($p = 0.0286$). For the static+Wnt, there was a significant difference between the 2 and 4 hour time points ($p = 0.0286$) and for the 2 and 24 hour time points ($p = 0.0286$) (fig. 40). Because of the increasing trend of the CPS/DNA ratios in both the FFSS and static groups and the statistically significant differences of the 24 hour harvest time for each of the Wnt positive groups, 24 hours was used as the harvest time for remaining experiments.

The final experiment utilized information gained from all previous experiments. TOPflash-MLO-Y4 cells were pretreated with 100nM of ICI for 24 hours or grown in control media withDMSO. Cells were then subjected to FFSS for 30 minutes at 2 dynes, while static slides were moved to new media

for the same duration. After 30 minutes, cells were moved back to their pretreatment media for another 24 hours, either with or without the addition of Wnt3a, for a total exposure time to ICI of 48 hours.

The addition of Wnt3a was a driving force, with all Wnt positive groups significantly higher in CPS/DNA ratios than all Wnt negative groups. If Wnt3a is present, then the ICI pretreatment has a significant impact, with the ICI positive groups (FFSS and static) lower than the ICI negative groups (FFSS and static). However, if Wnt3a is absent, then ICI does not make a difference (fig. 41).

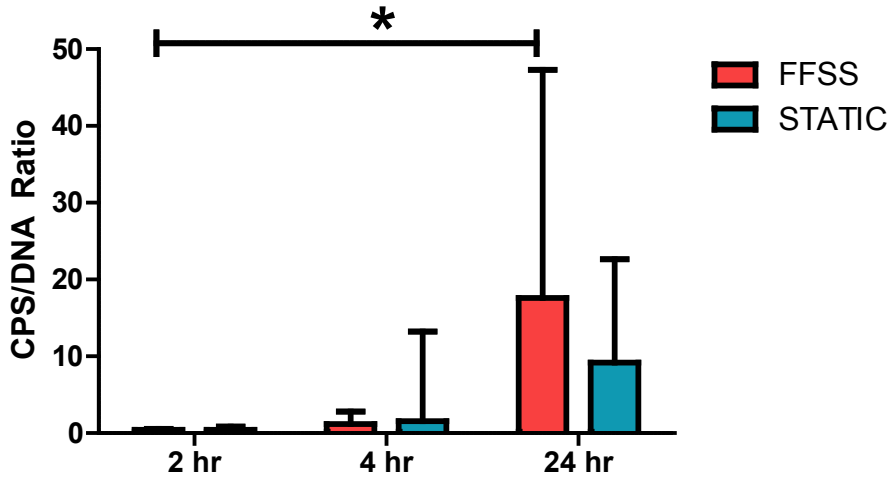

Figure 39. Activation of Wnt/β-catenin signaling increases as time increases regardless of FFSS or static conditions. Cells were subjected to 30 minutes of FFSS or static control and then harvested at either 2, 4, or 24 hours post-FF. Both Wnt positive and Wnt negative treatments were combined at each time point. The 24 hour FFSS group was significantly higher than the 2 hour FFSS group. (n = 7-8;*p < 0.05).

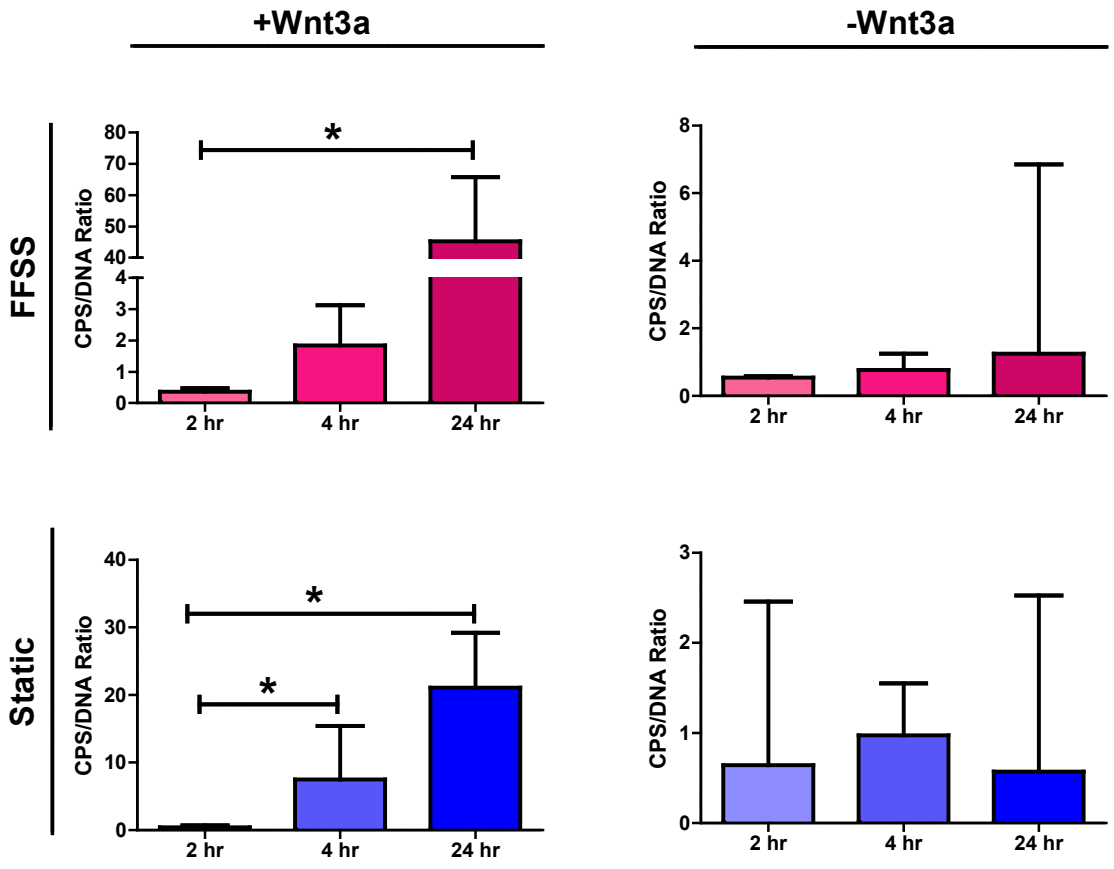

Figure 40. Addition of Wnt3a significantly increases activation of Wnt/β-catenin signaling over a 24 hour period in both FFSS or static conditions. None of the time points were significantly different from each other in the Wnt negative treatments, regardless of FFSS or static. In the Wnt positive groups, there were significant increases as time increases in the FFSS and static treatments. (n = 3-4; *p < 0.05).

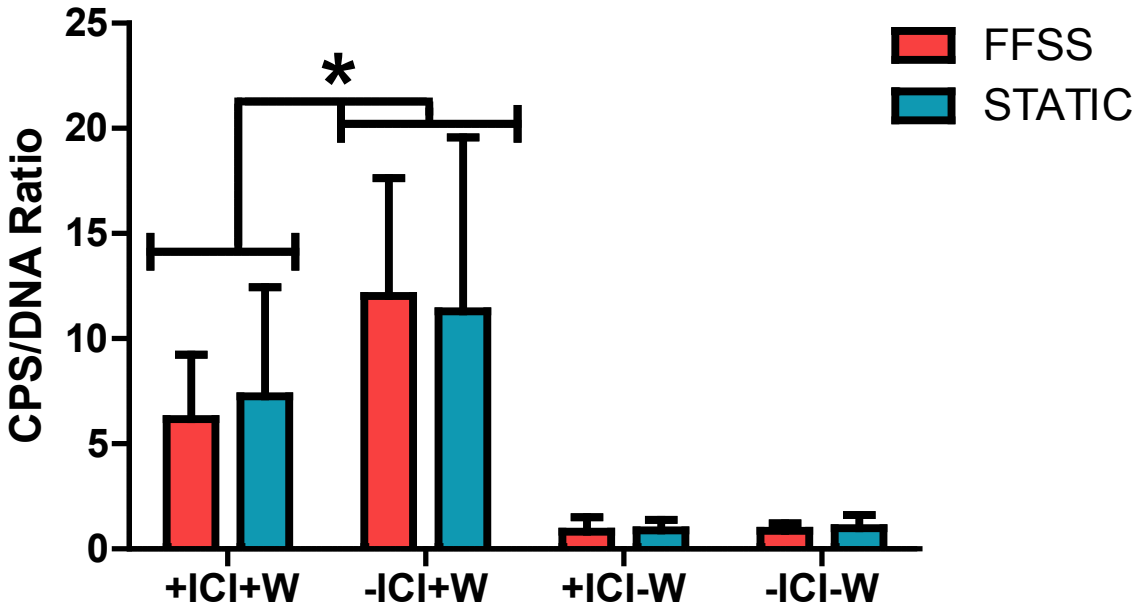

Figure 41. Activation of Wnt/β-catenin signaling is attenuated following ICI pre- and post-treatment when Wnt3a is present regardless of FFSS or static conditions. (n = 6; *p < 0.05).

Chapter 4

DISCUSSION

Ovariectomy and the consequent loss of estrogen resulted in a marked loss of mechanical load-induced activation of β-catenin signaling in osteocytes. Subsequent studies were conducted in an attempt to determine if this surprising observation was the result of altered biomechanical properties resulting in altered strain experienced by the osteocytes in the OVX bone or due to an altered intrinsic ability of the osteocyte to respond to mechanical load or both. Biomechanical properties were tested by 3-point bend to failure and bone architecture was examined through micro-CT, high-resolution microXCT and backscatter SEM. Osteoblast and osteoclast numbers were also determined histologically through VonKossa and TRAP staining, respectively. To assess if estrogen loss altered the intrinsic ability of the osteocyte to respond to mechanical load an *in vitro* cell culture model was used. Cells were exposed to an estrogen receptor inhibitor and then subjected to fluid flow sheer stress (FFSS) or static conditions. Cell activation was assessed using the TOPflash Luciferase reporter. These findings combined with the findings of the *in vivo* experiments gives insight to the role of estrogen in the osteocyte response to mechanical loading.

In Vivo **Mouse Model**

TOPGAL mice were ovariectomized (OVX) or sham operated at 16 weeks of age and used experimentally at 4 weeks post-surgery. In order to confirm successful OVX, uterus weight was recorded for both OVX and Sham groups following sacrifice. A decline in gonadal steroid hormones results in a loss of uterine tissue (Sato et al. 2003), as seen in the OVX group. It has been reported that serum 17β-estradiol levels drop from approximately 20 pmol/l to approximately 12 pmol/l (Modder et al. 2004). Although confirmation of reduced estrogen levels by measurement of blood serum hormone levels was not achieved (due to sensitivity of equipment and cross-reactivity of ELISA's), loss in uterine size and weight is standard by itself for an OVX to be deemed successful. Typical mouse estrogen levels may fluctuate during estrus cycles, but ranges from 50-70 pg/ml (Wood et al. 2007). Body weight

was not altered, either in weight gain or loss, but this may be a function of time post-surgery and animal model as rats can show body weight increase following OVX (Rosales Rocabado et al. 2018).

Previously it has been shown that activation of the Wnt/β-catenin signaling pathway occurs following mechanical loading in osteocytes (Lara-Castillo et al. 2015). The osteocyte has been postulated to be the mechanosensory cell of bone (Aarden et al. 1994) and the proposed model of biomechanical events is dependent on mechanical load to initiate downstream changes (Sawakami et al. 2006; Robling et al. 2008). Prior to sacrifice, mouse right forearms received a single session of mechanical loading at a global strain of 2200 microstrain (με) for 100 cycles at 2 Hz. These single session loading parameters are enough to activate the Wnt/β-catenin pathway (Robinson et al. 2006; Javaheri et al. 2014; Lara-Castillo et al. 2015). Determination of sacrifice times was based on activation of the Wnt/β-catenin pathway following loading with 1 hour during initial activation and 24 hours at peak activation (Lara-Castillo et al. 2015).

At 1 hour post-load, osteocyte activation in the OVX group was lower compared to the Sham group, but not yet significantly. By 24 hours, the OVX group had a significantly lower number of activated osteocytes than the Sham group suggesting these cells were not able to either sense the load (the strain on the osteocytes was below a threshold needed for activation) or respond to the load in the same manner as the Sham group. Older bone perceives strain differently than younger bone (Holguin et al. 2016), needing higher strain to achieve the same activation response (Nicolella et al. 2006). Mice in all groups of this study were the same age, so any changes in activation due to estrogen loss may mimic similar changes occurring in older bone. This leads to the question of what was responsible for the lack of activation in the OVX mice: alterations to the bone biomechanical properties and anatomical structure, on either a whole bone or microarchitecture level or an intrinsic change to the osteocyte itself in terms of its Wnt/β-catenin signaling pathway.

To test whole bone architecture and microarchitecture properties, along with biomechanical properties, micro-CT, high-resolution microXCT, backscatter SEM, and 3-point bending were performed. Micro-CT data provided a gross examination of cortical and trabecular bone, while high-resolution microXCT and backscatter SEM provided 3-dimesional and 2-dimensional perspective,

respectively, at the lacunae of the osteocytes. Three-point bending offered insight to the strength and brittleness of the bone, specifically through the mid-diaphysis.

Most of the micro-CT cortical parameters remained unchanged between the OVX and Sham group, with only cortical thickness being significantly lower in the OVX group. Although the difference is statistically significant, the question remains, is it biologically significant, especially since the decrease is only by -6%. Changes in cortical bone following OVX can be inconsistent (Osterhoff et al. 2016). One study reported no changes to the cortical volume in the mid-shaft region of rat tibia and femur following 4 weeks and 18 weeks post-OVX (Zhang et al. 2007). Another study found an increase in cortical thickness in rats 8 weeks post-OVX (Rosales Rocabado et al. 2018). The loss of cortical bone identified in the OVX mice may be an effect of the animal model and strain (genetic background). A 2005 study found differences in cortical bone loss following OVX between C57BL/6J (B6), A/J and C3H/HeJ (C3H) strains, with B6 and A/J mice losing cortical area and width 18 weeks post-OVX due to marrow expansion and C3H mice losing cortical width and area at 4 weeks post-OVX due to loss of subperiosteal area (Li et al. 2005). This dissertation used CD-1 mice. A decrease in cortical thickness was observed at 4 weeks post-OVX, and it is likely this bone loss would have continued if the study had included other groups sacrifice at longer time periods post-OVX. It is not clear if the observed thinner cortex would dramatically alter the load: strain relationship in the OVX bones. Stern et al. demonstrated that long-term OVX in the rat resulted in a change in the modulus of the perilacunar matrix that changed the strain fields around the osteocyte as predicted by finite element (FE) analysis (Stern et al. 2018). Further studies are needed to determine if this might occur in the short-term OVX studies in this dissertation. Additionally, strain gage studies could be performed to determine the load: strain relationship and if it was significantly altered in the OVX mice. At present, the exact strain experienced by each osteocyte on the compression or tensile side of the bone is unknown.

Trabecular bone showed more changes that are significant in micro-CT parameters than cortical bone. In trabecular bone, OVX mice had significantly lower BMD, BV/TV, and trabecular thickness, which is a reproducible, consistent biological response following OVX (and why this model is used for osteoporosis studies). While trabecular number and separation were lower in the OVX group,

it was not yet to a significant level, which may be a result of the study being 4 weeks post-OVX. Because of its architecture and location in long bones, trabecular bone, specifically in the appendicular skeleton, is ideal for transferring mechanical loads from the articular surfaces to cortical bone. Any potential loss of trabecular bone can thus influence the amount of load sensed by the cortical osteocytes. Trabecular bone has more surface area than cortical bone, leading to a more rapid turnover and subsequently, it is lost first during osteoporosis. Trabecular bone is highly anisotropic, especially with consideration to the connectivity of the lattice-like lamellar plates, which overall has a higher contribution to the biomechanical strength of the bone than trabecular BMD or thickness (Mittra et al. 2008). Although the trabeculae of the OVX mice were overall thinner compared to their Sham counterparts, OVX trabecular number and therefore connectivity remained similar between the two groups (OVX was lower, but not yet to a significant level). Hence, the integrity of the trabecular bone, while potentially compromised, should remain intact along with their biomechanical properties.

Changes to cortical and trabecular bone did not translate to altered breaking forces required during the 3-point bend to failure tests. Despite the significant decline of cortical thickness and loss of trabecular thickness, there were no significant differences in any of the 3 point bending tests, which may be a function of time of sacrifice post-OVX and mouse strain used. Previously it has been shown that B6 mice have a slightly decreased (7-8%) maximum load and stiffness using 4-pt bending at 4 and 8 weeks post-OVX and that decrease almost doubles (14-19%) at 16 weeks post-OVX (Li et al. 2005). Perhaps a longer time span from OVX to sacrifice, i.e. 8 weeks instead of 4 weeks, would allow for a greater loss of cortical and trabecular bone, leading to differences between the biomechanical properties of the OVX and Sham groups. Because 3-point bending is conducted on the horizontal, non-loading axis of the long bone, any alterations to trabecular or cortical bone would impact this weak axis first and be observed in the work to failure.

Osteocyte lacunae of the tibiae were measured for 2-dimensional analysis via backscatter SEM and for 3-dimensional analysis via high-resolution microXCT following OVX. Previously, it has been shown that osteocytes have the ability to remodel their perilacunar matrix through reversible osteocytic osteolysis, specifically during times of lactation, to maintain blood calcium levels (Qing et al. 2012) and

this increase in lacunar size during lactation can lead to reduced tissue-level elastic modulus (Kaya et al. 2017). Although perilacunar remodeling can be seen during lactation times of the reproductive cycle, it may also be a mechanosensitive process (Yee et al. 2019). The perilacunar area can also change its microenvironment, leading to either a hypo- or hyper-mineralized state. In 2007, it was reported that perilacunar tissues with an increased modulus experienced a decrease in maximum strain (Bonivtch et al. 2007a). Frost and colleagues (1997) postulated a stiffened perilacunar matrix in estrogen deficient conditions, and potential for fewer mechanical signals, under loading conditions, leading to favorable situations for bone resorption and loss. Other studies have also noted changes to rat lacunae with mechanical loading (Ferreyra et al. 2000; Bozal et al. 2001). Typically, average, local perilacunar strains are greater than macroscopically applied strains (of bovine tibia) (Nicolella et al. 2006). In human bone tissue that is osteoporotic, there is an increase in hypermineralized osteocyte lacunar number density (Carpentier et al. 2012), which may result in the attenuation of mechanical signaling to embedded osteocytes. However, in rat, nanoindentation did not reveal a significant difference in Young's Modulus of the perilacunar area between OVX and Sham groups (Stern et al. 2018). Changes to the lacunar-canilicular system, specifically larger porosity, can be seen in cortical and trabecular bone in the proximal tibia metaphysis following OVX in rats, with little changes in diaphysis cortical bone (Sharma et al. 2012). Sharma and colleagues found this increase in porosity was not due to changes in lacunar density, number of canaliculi per lacuna or lacunar size, but canalicular size. In this dissertation, the physiochemical nature of the perilacunar matrix was not tested, nor was canilicular size or density (only lacunar size, lacunar density, and total lacunar number were measured), so it is unknown whether the perilacunar matrix of these animals underwent alterations that lead to a lower strain being sensed by the osteocyte. Whether this was the case may be elucidated with the cell culture experiments, since the cell line used is not surrounded by a matrix, meaning all cells would experience the same strain levels, regardless of estrogen's presence or absence.

Backscatter SEM and high-resolution microXCT showed similar results, in that no parameters had significant differences. Osteocyte lacunar number, area, and volume remained unchanged following OVX, suggesting that estrogen does not play a role in osteocytic osteolysis and remodeling

at the perilacunar matrix. However, it cannot be ruled out that estrogen may affect the physiochemical nature of the perilacunar matrix, resulting in alterations to the perceived strain translated to the osteocyte during mechanical loading.

Typical bone remodeling (not osteocytic osteolysis) is accomplished through two bone cells with opposing functions: osteoblasts, which laydown bone matrix and osteoclasts, which reabsorb bone matrix. Normally, osteoclasts remove bone in an area called bone remodeling compartments, followed by osteoblasts secreting new matrix in the same area. This delicate balance of bone turnover seems to be mediated, at least in part, by estrogen. It is well established that estrogen deficiency, like seen following menopause or OVX, is associated with bone loss and osteoporosis (Albright et al. 1941); estrogen is a regulator of bone metabolism in both women and men (Khosla et al. 2008; Khosla et al. 2011); and estrogen can prevent bone loss following OVX (Lindsay et al. 1976). However, despite the knowledge that estrogen is critical for bone, it is difficult to define the exact mechanisms or pathways estrogen uses to regulate bone metabolism. Treatment of postmenopausal women with estrogen caused a sustained lowering of bone resorption markers in the urine and serum, while bone formation markers saw a short increase, followed by a decrease (Hannon et al. 1998), indicating that in the presence of estrogen, bone resorption is halted, while bone formation is likely to not increase.

Since the osteocyte is key to regulating bone remodeling, it is likely that estrogen deficiency first targets the osteocyte, which is then translated to altered control of osteoblast and osteoclast activity and numbers. Osteocyte apoptosis increases following estrogen deficiency in both humans (Tomkinson et al. 1997) and in cortical and trabecular bone of rat tibia (Tomkinson et al. 1998). The addition of estrogen following OVX prevents osteocyte apoptosis (Tomkinson et al. 1998). Research has shown that treatment of MLO-Y4 cells with 17β-estradiol prevents etoposide-induced apoptosis by activating the nitric oxide/cGMP/cGMP-dependent protein kinase cascade leading to phosphorylation of Bcl-2 associated death promoter (BAD), a pro-apoptotic protein (Marathe et al. 2012). With a diminished osteocyte population due to estrogen loss, the response to load would be attenuated; however, total osteocyte number was counted in the ulna slices during β-gal activation counting, and no difference was seen. In addition, lacunar number counted during backscatter SEM and high-resolution microXCT

was not significantly different either, although it was not determined if these lacunae housed an osteocyte or were empty. This suggests that the regulation of bone turnover following OVX was not due to direct loss of osteocytes but instead due to their lack of response to load and signaling to osteoclasts and osteoblasts.

Along with osteocytes, osteoclasts can be a direct target for estrogen. Deletion of ERα in osteoclasts results in decreased trabecular bone mass, partially due to increased osteoclast lifespan (Nakamura et al. 2007; Martin-Millan et al. 2010). Estrogen reduces osteoclast differentiation through actions of Receptor Activator of Nuclear Factor Kappa B Ligand (RANKL) (Srivastava et al. 2001). In mouse models, estrogen can control levels of interleukin-1 (IL-1), IL-6, macrophage-colony stimulating factor (M-CSF), tumor necrosis factor-alpha (TNF-α), and prostaglandins (Manolagas and Jilka 1995). This dissertation did not look at lifespan of osteoclasts, nor regulation of cytokines and receptors known in osteoclast function and differentiation. It has been suggested that osteocytes can inhibit osteoclast function, but not number, through secretion of transforming growth factor-beta (TGF-β) and this inhibition affect is enhanced following treatment with 17β-estradiol (Heino et al. 2002). This suggests that as long as estrogen is present, osteocytes inhibit osteoclast function, but during estrogen withdraw the inhibition is lifted and osteoclast bone resorption can increase. However, that study used conditioned media from MLO-Y4 cells (mouse derived) added to rat osteoclasts, while the current study utilized an *in vivo* mouse model, so it may be difficult to say whether the osteocytes and TGF-β are behaving in a similar manner. All of the previous work shows that estrogen can both directly or indirectly affect osteoclasts and bone resorption. The results of the current study, following OVX, osteoclast number increased, as did trabecular bone loss, suggesting the amount of osteoclasts present is directly related to the amount of bone resorption occurring; however, osteoclast function was not measured, so the specific mechanism used to accomplish this bone loss can only be speculated.

Osteoblasts showed a decrease in number following OVX, suggesting a potential lack of bone building occurring. Estrogen can, potentially, directly or indirectly alter osteoblast function by multiple mechanisms. Recently, semaphorin D (Sema4D) has been shown to be expressed by osteoclasts and negatively regulate bone formation by binding to its receptor on osteoblasts, subsequently inhibiting

insulin-like growth factor-1 (IGF-1) and modulating osteoblast motility (Negishi-Koga et al. 2011). This means when osteoclast number is high (as seen during post-OVX), osteoblast function and potentially number are negatively affected. This correlates to the opposing levels of osteoclasts and osteoblasts seen following OVX. Estrogen can stop osteoblast apoptosis and increase osteoblast lifespan by activating Scr/Shc/ERK signaling pathway and downregulating JNK (Kousteni et al. 2001). Estrogen deficiency may also influence bone formation through mechanisms involving oxidative stress, which can antagonize Wnt signaling (Manolagas and Almeida 2007). Nuclear Factor kappa-B (NF-κB) may also play a role in bone loss. During estrogen deficient times and times of bone loss, NF-κB levels are elevated in osteoblastic cells, and inhibition of NF-κB leads to a reduction in bone loss following OVX though increasing expression of a transcription factor known to play a role in bone matrix formation (Chang et al. 2009). This suggests that increases in NF-κB in osteoblastic cells may cause a decrease in the osteoblastic cells' ability to successfully deposit bone matrix, leading to an imbalance in bone formation and bone resorption. The results of the current study show a decrease in osteoblast number following OVX, which correlates to the bone loss (or lack of bone addition); however, it did not look at osteoblast function or any associated marker of function, so the specific mechanism of osteoblast inhibition and decrease in number can only be speculated.

In Vitro Cell Culture Model

While the *in vivo* mouse model provided insight into the dynamics of how the osteocyte responds to load in the absence of estrogen in the whole animal, it cannot fully answer the question of how the osteocyte intrinsically responds to the load. It is necessary to look at the osteocyte in a cell culture model to assess its workings without influence from other body systems. Primary osteocytes from the OVX mice could have been used for cell culture experiments, but the low yield of cells and inability to obtain pure populations limited the use of primary osteocytes. Also, the "history" of the osteocyte exposure to estrogen in the whole animal would not be possible to ascertain. For these reasons, the MLO-Y4 osteocyte-like cell line was chosen (Kato et al. 1997). These cells are murine lone bone-derived and it is easy to manipulate their growing conditions for experimental use.

During initial establishment of the MLO-Y4 cell line, growth parameters included α-MEM media supplemented with 5% of FBS and 5% CS or 10% FBS by itself (Kato et al. 1997). However, since phenol red, used in α-MEM media as a pH indicator, is a known estrogen mimetic (Berthois et al. 1986) and serums contain low, though potentially biologically relevant, levels of steroid hormones, the regular growth parameters may present an environment that has enough estrogen (or estrogen mimetics) to potentially influence results. While few previous research methods have adopted the approach of providing an estrogen free environment with charcoal stripped serums and phenol red free media (Marathe et al. 2012; Ren et al. 2013), most have not (Zaman et al. 2006; Aguirre et al. 2007; Brennan et al. 2014; Deepak et al. 2017). However, the experiments that used an estrogen free environment did not characterize the growth and morphology of MLO-Y4 cells in that environment. It has been reported that estrogen withdraw increases MLO-Y4 apoptosis (Brennan et al. 2014), but cell morphology was not reported. Before providing further experimentation, it was necessary to ensure that MLO-Y4 cells could sustain normally in phenol red free media supplemented with altered, charcoal-stripped serums.

Charcoal stripping serums is a common method to remove endogenous compounds like steroid, peptide and thyroid hormones, and lipids; however, this approach may also strip other serum contents that may be vital for cell growth and health. A 2009 study looked at the effects of resin and charcoal stripping on FBS and bovine calf serum (BCS) (Cao et al. 2009). They found that charcoal stripping removed all, or almost all, of cortisol and estrogen from FBS and BCS, along with the majority of testosterone, progesterone, thyroid hormones T3 and T4, vitamin B_{12}, and a small amount of folic acid. Other entities had various degrees of removal from serums following stripping: alkaline phosphatase, α-amylase, aspartate aminotransferase, lactate dehydrogenase, calcium, chloride, cholesterol, creatinine, creatine kinase, glucose, magnesium, phosphorus, potassium, total bilirubin and uric acid. While the 2009 study provided information into the stripped components of the serums, it did not look at the potential impact the loss of these elements would have on any given cell line.

In addition to looking at the effects of charcoal stripped serums, it was necessary to assess the impact of reduced serum concentrations on cell morphology. Previously, low concentration (0.1%) serums were utilized during FFSS since the presence of fresh serum may activate signaling pathways

and mask MLO-Y4 response (Lara-Castillo et al. 2015). While the time in reduced serum concentration was brief (15 minutes), is it a long enough exposure time, in conjunction with the nature of the stripped serums, to alter cell properties such as growth and function?

MLO-Y4 cells showed altered morphology in charcoal stripped serums under a variety of circumstances: at areas of high density, for durations longer than 24 hours, when serum concentration was under 2.5% for either serum, or when both serums were not simultaneously used. Ultimately, this is not surprising, considering the myriad of components removed during the stripping process. Although cells were grown in phenol red free media and charcoal stripped serum, the stripped serums had a larger impact on cell morphology. Remarkably, although cell morphology was altered, the levels of pAKT (when normalized to β-actin) remained consistent when 2.5% or 1% of both charcoal stripped serums were used. At 0.5% or 0.1%, normalized pAKT levels diminished by close to half the amount. Due to lack of replicates, this reduction was not tested for statistical significance; however, this decline may indicate that cell function, specifically concerning Wnt signaling, along with morphology is compromised periods in conditions of low concentration of stripped serums.

At this time, a switch was made from using MLO-Y4 cells to TOPflash-MLO-Y4 cells. The TOPflash-MLO-Y4 cells were created by Dr. Nuria Lara-Castillo in Dr. Mark Johnson's lab. They are MLO-Y4 cells that have been stably transfected with the pGL4.49 vector containing the luciferase gene under the control of the TCF/LEF promotor that drives β-catenin expression in a cell. This reporter is used to quantitate β-catenin signaling in the transfected cells, which express luciferase in response to pathway activation. Luciferase converts an added substrate into light, which is easily quantitated and can act as a reporter of activity following treatments. While luciferase has been used previously in MLO-Y4 cells and cultures (Mulcahy et al. 2011; Baek et al. 2014; Kringelbach et al. 2014), it has not been in the capacity of reporting β-catenin signaling. Because of this, it was necessary to ensure luciferase response in stripped serums, phenol red free media and with the addition of 17β-estradiol and Wnt3a.

The addition of Wnt3a is a powerful stimulator of β-catenin signaling, as Wnt can bind the LRP5/6 and FZ receptors, causing subsequent increase in cytoplasmic β-catenin, which can then translocate to the nucleus. The TOPflash-MLO-Y4 cells showed a robust response to Wnt3a treatment

(compared to the non-Wnt treatments), although the response was slightly diminished in phenol red free media and stripped serums, it was not to a significant level. The addition of 17β-estradiol to the non-Wnt3a cells showed a slight increase in luciferase activity, but not nearly to the levels as Wnt3a alone, nor was it a statistically significant increase. There were also no synergistic effects of treatment with Wnt3a and 17β-estradiol together, regardless of media and supplementation. Estrogen or loss of estrogen has been shown to regulate many MLO-Y4 functions/molecules. Estrogen deficiency alters mechanosensation in osteocytes by impairing $\alpha_v\beta_3$ integrin (Geoghegan et al. 2019) and fluid flow induced calcium oscillations in osteocytes (Deepak et al. 2017). Estrogen has pro-survival, anti-apoptotic effects (Marathe et al. 2012; Brennan et al. 2014) and can upregulate connexin-43 intercellular gap junctions (Ren et al. 2013). Despite all of these findings, the literature does not provide evidence for direct activation of Wnt/β-catenin pathway by estrogen, either alone or synergistically with Wnt.

Since the charcoal stripped serums were altering cell morphology and not causing significant changes to results of experiments, the decision was made to forgo using stripped serums for the rest of the experiments. Any level of estrogen present in the serums would be considered the baseline and exogenous estrogen of known concentrations would be added to the media for experimentation. Normal levels of 17β-estradiol are 19.8 pg/ml in FBS and 33.7 pg/ml in CS (Cao et al. 2009). Circulating 17β-estradiol levels during mouse estrus fluctuate between 50-70 pg/ml (Wood et al. 2007), so hormone levels in the serums are at the low end of biologically active murine levels, and therefore considered to be “estrogen negative”.

The levels of the estrogen receptors, ERα and ERβ, were examined in TOPflash-MLO-Y4 cells prior to and following treatment with 17β-estradiol. It has been shown that estrogen and strain can cause ERα nuclear translocation, with ERα staying in the nucleus longer with estrogen treatment than with strain (Zaman et al. 2006). The same paper also saw a transient reduction of ERα mRNA levels in MLO-Y4 cells following estrogen exposure, with levels returning to control values at 32 hours post-exposure (Zaman et al. 2006). However, the amount of time the cells were exposed to estrogen was not stated in the paper. Consistent with the literature, mRNA levels of ERα in TOPflash-MLO-Y4 cells

initially dropped following estrogen exposure and then recovered. ERβ did not follow a similar pattern, with levels dropping and staying low following estrogen exposure. This indicates that estrogen levels regulate ERα, but not ERβ, content and that ERα plays a more important role in the osteocyte's responses following estrogen exposure or withdraw.

It has been shown that knocking out ERα *in vivo* impacts osteocyte ability to respond to mechanical load (Zaman et al. 2006). Mice lacking ERα and ERβ do not respond to mechanical loading, and plasma membrane localization of ERα and its interaction with caveolin-1 are required for stretch induced ERK activation and anti-apoptosis in osteocytes (Aguirre et al. 2007). To look for similar actions *in vitro* in TOPflash-MLO-Y4 cells, ICI (Fluvestrant™ ICI 182,780) an anti-estrogen receptor agent was added to treatments to look for interactions in the presence of Wnt3a, 17β-estradiol, and combinations of each.

ICI is a novel agent, designed to be purely antagonistic at the estrogen receptor, unlike its preceptor agents, like Tamoxifen, which can act as partial agonists at certain tissues (Wakeling 1995). ICI downregulates the estrogen receptor, by blocking receptor dimerization and activation of AF1 and AF2 domains, resulting in a quicker degradation and receptor turnover (Wakeling 1995).Clinical trials have found ICI to be as effective as aromatase inhibitors in the treatment of advanced breast cancer following Tamoxifen failure (Howell et al. 2000).

Adding ICI to TOPflash-MLO-Y4 cells did not decrease their response to Wnt3a or to17β-estradiol under static conditions. In fact, the +Wnt3a, +17β-estradiol and +ICI treatment had the highest activity (CPS/DNA) of all groups. However, all of these treatments were applied at the same time. Since ICI and 17β-estradiol were being added simultaneously, was 17β-estradiol binding to the ER before ICI had a chance to bind and cause downregulation? Would adding ICI for a pretreatment duration allow appropriate downregulation and subsequent decrease in osteocyte response? In addition, was 17β-estradiol being used at an appropriate concentration?

To address these questions, ICI pretreatment with 100nM for 24 hours was performed. Some papers have used shorter incubation periods (30 minutes) (Aguirre et al. 2007), while others have used longer (2, 3, or 5 days) (Deepak et al. 2017), but both used the same concentration, 100nM. Estrogen

concentrations used have varied as well in the literature, with concentrations of 10^{-7} (Ren et al. 2013) and 10nM (approx. 10^{-8}) (Marathe et al. 2012; Brennan et al. 2014; Deepak et al. 2017; Geoghegan et al. 2019) being used. While normal levels of estrogen has been established as being anti-apoptotic (Marathe et al. 2012), high doses of estrogen have pro-apoptotic actions (Song and Santen 2003), especially on breast cancer tissue and cells. TOPflash-MLO-Y4 cells exposed to Wnt3a and 17β-estradiol showed similar CPS/DNA ratio responses, with only 10^{-9} being statistically significantly lower than 10^{-7}. Since 10^{-6}, 10^{-7} and 10^{-8} concentrations were relatively similar, 10^{-6} was chosen as the concentration to continue with for further experiments.

Following pretreatment with ICI, ERα and ERβ levels were again assessed through PCR. Again, ER β levels were consistently lower than ERα levels, indicating a more important role for ERα in the interaction of 17β-estradiol and ICI. With only ICI pretreatment, ERα levels dropped, but were elevated with ICI pretreatment followed by secondary treatments with 17β-estradiol, Wnt3a or in combination. Comparing the ICI treatment for 24 hours only to the ICI pretreatment followed by secondary 24 hour treatment, it can be seen that ICI does downregulate ERα content (which is in alignment with the literature) and 24 hours post-ICI exposure, levels of ERα surpass baseline levels.

Beta-catenin pathway activation in response to ICI pretreatment followed by secondary treatments were assessed. One would expect that pretreatment with ICI followed by treatment with 17β-estradiol (with or without Wnt3a) would result in a decrease in CPS/DNA ratio, which is what was observed. However, this is also surprising since PCR revealed that ERα levels rebound in 24 hours after removal from ICI exposure. Treatment with ICI causes ERα receptor half-life to decrease from 5 hours to 30 minutes (Wijayaratne and McDonnell 2001), so 24 hours is enough time to replenish ERα levels to normal. Interestingly, the secondary treatment of Wnt3a, 17β-estradiol and ICI were not significantly different whether ICI was a pretreatment or not. Both CPS/DNA ratios were lower than their control comparisons of ±ICI pretreatment followed by Wnt3a only, which indicates the secondary treatment of ICI does keep the 17β-estradiol from having an effect.

TOPflash-MLO-Y4 cells subjected to FFSS had a significantly greater CPS/DNA ratio at 24 hours than at 2 hours. As well, static cells exposed to Wnt3a also showed statistically higher CPS/DNA

ratio at 24 hours. This correlates to earlier findings, that the β-catenin signaling pathway reaches peak activation at 24 hours following FFSS (Lara-Castillo et al. 2015).

Several studies have looked at some form of mechanical stimulation, either with influences of estrogen, ER's or ICI, and the response of MLO-Y4 cells. Aguirre and colleagues (2007) used biaxial stretching, following ICI pretreatment or in osteocytes with ERα and ERβ knocked out and found that osteocytes lacking ERα and ERβ were unresponsive to mechanical stimulation, but the response was rescued with the addition of the ligand-binding domain of either receptor. Pulsatile FFSS causes PGE_2 release and β-catenin nuclear translocation in MLO-Y4 cells (Kamel et al. 2010b). Withdraw or inhibition of estrogen caused low levels of PGE_2 release and attenuates calcium oscillations in MLO-Y4 cells following oscillatory FF (Deepak et al. 2017). The presence of estrogen enhanced expression of connexin-43 and gap junction intercellular communication, and enhanced the mechanosensitivity of MLO-Y4 cells to oscillatory FF (Ren et al. 2013). Estrogen withdraw leads to smaller focal adhesions by a reduction in $\alpha_v\beta_3$ integrin, leading to altered responses to oscillatory FF (Geoghegan et al. 2019). These findings correlate to the results of the current study, which found that with ICI, the CPS/DNA ratio is significantly lower than without ICI when Wnt3a is present, regardless of fluid flow or static conditions. This indicates that inhibiting ER mitigates a response to Wnt3a, leading to a diminished β-catenin response. While ICI was able to downregulate the amount of ER, it did not completely abolish it, leading to still some β-catenin translocation and activity. Estrogen remained in the system overall, since the serums (combined) contained concentrations of estrogen that are just high enough to be biologically relevant. This has considerations since estrogen can act through GPR30, which causes release of intracellular calcium, release of PI3K and PIP3, which can activate Akt and amplify the Wnt pathway. This may explain why the FFSS and static treatments were not significantly different. Another explanation may be that the addition of Wnt3a saturated the signaling pathway, masking the response to FFSS.

Chapter 5

CONCLUSIONS

The goal of this research was to determine the effects of estrogen regulation of the Wnt/β-catenin pathway in osteocytes in response to mechanical loading. While many previous studies investigated mechanical loading responses either in whole animals or in cell culture, few utilized both approaches, and among those that did, even less looked at the impact of estrogen on the system. The study design of this dissertation allowed examination into both models, in hopes of correlating the responses and understanding the dynamics in both methods.

The initial hypothesis states that estrogen is a critical factor in the responsiveness of the osteocyte to mechanical loading via regulation of the Wnt/β-catenin pathway; and in the absence of estrogen, osteocytes will have a decreased activation upon mechanical loading. This hypothesis was addressed through two specific aims: first, determine the effects of ovariectomy on the ability of the osteocyte to activate the Wnt/β-catenin pathway in response to mechanical loading; and second, determine the role and relative importance of estrogen on the activation of the Wnt/β-catenin pathway *in vitro* in response to mechanical load.

Specific aim 1 demonstrated post-OVX architectural changes to and loss of trabecular, but not cortical, bone. Bone biomechanical properties were unchanged and lacunar number, size and density remained consistent. At trabecular bone, the number of osteoclasts increased, while osteoblast numbers decreased. Overall, osteocyte numbers were unchanged; however, a dramatic decline was observed in the activation of the Wnt/β-catenin signaling, especially 24 hours post-OVX. Since the loading model primarily loads cortical bone, and cortical bone remained unchanged, it is likely that the changes in osteocyte responsiveness to loading is due to an intrinsic change to the osteocyte itself and not from alterations to gross bone structures. However, the potential does exist for changes to the physiochemical nature of the perilacunar matrix or specific strain felt at the lacunar level. Both of these procedures and methods were outside the limitations of this investigation. However, they provide avenues for investigation in future studies.

Specific aim 2 demonstrated MLO-Y4 cell sensitivity to charcoal stripped serums (specifically during long periods and in low concentrations) and their deviations from normal cell morphology if not provided with full strength serums. Previous studies that utilized stripped serums did not report changes to cell morphology, so this may be considerations for future experiments. TOPflash-MLO-Y4 cells have a lack of β-catenin signaling in the presence of Wnt3a when ICI (an estrogen receptor antagonist) is present in pre- and post-treatment media, regardless of mechanical stimulation via FFSS or static conditions. ERα is a player in Wnt/β-catenin signaling and this decrease in signaling following ICI treatment (which antagonizes both ERα and ERβ) further strengthens its vital role in the pathway. However, this study did have limitations. First, the non-charcoal stripped serum, though they contain low levels of estrogen, may be biologically relevant levels. Although ICI acts by increasing the degradation of ER, the cell can potentially make new ER due to the presence of low levels of estrogen in the media. This would explain the mild reduction in signaling, but not complete loss. Second, fluid flow with estrogen added to the media was not performed. Although there was not a gain under signaling in static conditions, estrogen may have further enhanced signaling in a post-fluid flow environment. Further experimentation, with estrogen, fluid flow and ICI is needed to fully understand and appreciate this interaction. In addition, it may be valuable to replicate the same experimental design with alternative cell lines.

Loss of estrogen attenuates the ability of the osteocyte to activate β-catenin signaling. Mechanistically this appears to be due to alterations in the intrinsic ability of the osteocyte to respond to load, as changes in bone biomechanical behavior and cortical bone architecture were not observed and therefore could not explain the lack of activation. However, further studies such as building finite element models to assess strain fields surrounding osteocytes or nano-indentation at the perilacunar matrix may provide insight into microarchitecture alterations.

The present study takes two separate systems (whole animal and cell culture) and attempts to look at the impact of estrogen on Wnt/β-catenin signaling in osteocytes in response to mechanical loading in a parallel fashion. While OVX in mice creates an environment void of estrogen, providing the same environment to cells in culture creates a challenge. To this end, the dynamics of what occurs in

the animal model can never truly be replicated using cell culture methods. While outcomes and results may be similar, they do not represent identical methodology. Alternative cell lines, such as IDG-SW3, which produce mineral during transition from late osteoblast to osteocyte (Woo et al. 2011), or the OmGFP-66 cell line that differentiates into green fluorescent protein-tagged osteocytes that forms mineral with a bone-like lacunar-canilicular structure (Wang et al. 2019) could provide alternative models to further interrogate the role of estrogen *in vitro* loading model systems.

Overall, the goal is to provide relevant and applicable information about bone and its behavior under estrogen deficient and osteoporotic conditions. Further experimentation and inquiry is needed to completely comprehend the dynamic nature of bone, its cells, and how these cells interact with each other and other body system, and react to disease states. The findings presented in this dissertation provide new knowledge about the role of estrogen in osteocyte biology, which ultimately could lead to new treatments for osteoporosis that would improve patient health and quality of life.

Literature Cited

Aarden EM, Burger EH, Nijweide PJ. Function of osteocytes in bone. J Cell Biochem 1994;55:287-99.

Aguirre JI, Plotkin LI, Gortazar AR, Millan MM, O'Brien CA, Manolagas SC, et al. A novel ligand-independent function of the estrogen receptor is essential for osteocyte and osteoblast mechanotransduction. J Biol Chem 2007;282:25501-8.

Albright F, Smith PH, Richardson AM. Postmenopausal osteoporosis: Its clinical features. JAMA1941;116:2465-74.

Artsi H, Cohen-Kfir E, Gurt I, Shahar R, Bajayo A, Kalish N, et al. The sirtuin1 activator srt3025 down-regulates sclerostin and rescues ovariectomy-induced bone loss and biomechanical deterioration in female mice. Endocrinology 2014;155:3508-15.

Ascenzi P, Bocedi A, Marino M. Structure–function relationship of estrogen receptor α and β: Impact on human health. Mol Aspects Med 2006;27:299-402.

Baek K, Hwang HR, Park HJ, Kwon A, Qadir AS, Ko SH, et al. Tnf-alpha upregulates sclerostin expression in obese mice fed a high-fat diet. J Cell Physiol 2014;229:640-50.

Bartell SM, Han L, Kim HN, Kim SH, Katzenellenbogen JA, Katzenellenbogen BS, et al. Non-nuclear-initiated actions of the estrogen receptor protect cortical bone mass. Mol Endocrinol 2013;27:649-56.

Berthois Y, Katzenellenbogen JA, Katzenellenbogen BS. Phenol red in tissue culture media is a weak estrogen: Implications concerning the study of estrogen-responsive cells in culture. Proc Natl Acad Sci U S A 1986;83:2496-500.

Bonewald LF, Johnson ML. Osteocytes, mechanosensing and wnt signaling. Bone 2008a;42:606-15.

Bonewald LF, Johnson ML. Osteocytes, mechanosensing and wnt signaling. Bone 2008b;42:606-15.

Bonewald LF. The amazing osteocyte. J Bone Miner Res 2011;26:229-38.

Bonivtch AR, Bonewald LF, Nicolella DP. Tissue strain amplification at the osteocyte lacuna: A microstructural finite element analysis. J Biomech 2007a;40:2199-206.

Bonivtch AR, Bonewald LF, Nicolella DP. Tissue strain amplification at the osteocyte lacuna: A microstructural finite element analysis. J Biomech 2007b;40:2199-206.

Boyden LM, Mao J, Belsky J, Mitzner L, Farhi A, Mitnick MA, et al. High bone density due to a mutation in ldl-receptor-related protein 5. N Engl J Med 2002;346:1513-21.

Bozal CB, Fiol JA, Ubios AM. Early osteocyte response to bone resorption stimuli. Acta Odontol Latinoam 2001;14:24-9.

Brennan MA, Haugh MG, O'Brien FJ, McNamara LM. Estrogen withdrawal from osteoblasts and osteocytes causes increased mineralization and apoptosis. Horm Metab Res 2014;46:537-45.

Cao Z, West C, Norton-Wenzel CS, Rej R, Davis FB, Davis PJ, et al. Effects of resin or charcoal treatment on fetal bovine serum and bovine calf serum. Endocr Res 2009;34:101-8.

Carpentier VT, Wong J, Yeap Y, Gan C, Sutton-Smith P, Badiei A, et al. Increased proportion of hypermineralized osteocyte lacunae in osteoporotic and osteoarthritic human trabecular bone: Implications for bone remodeling. Bone 2012;50:688-94.

Chang J, Wang Z, Tang E, Fan Z, McCauley L, Franceschi R, et al. Inhibition of osteoblastic bone formation by nuclear factor-kappab. Nat Med 2009;15:682-9.

Clevers H, Nusse R. Wnt/beta-catenin signaling and disease. Cell 2012;149:1192-205.

DasGupta R, Fuchs E. Multiple roles for activated lef/tcf transcription complexes during hair follicle development and differentiation. Development 1999;126:4557-68.

Deepak V, Kayastha P, McNamara LM. Estrogen deficiency attenuates fluid flow-induced [ca(2+)]i oscillations and mechanoresponsiveness of mlo-y4 osteocytes. FASEB J 2017;31:3027-39.

Dubrow SA, Hruby PM, Akhter MP. Gender specific lrp5 influences on trabecular bone structure and strength. J Musculoskelet Neuronal Interact 2007;7:166-73.

Evans R. The steroid and thyroid hormone receptor superfamily. Science 1988;240:889-95.

Ferreyra RS, Ubios AM, Gendelman H, Cabrini RL. Enlargement of periosteocytic lacunae associated to mechanical forces. Acta Odontol Latinoam 2000;13:31-8.

Frost HM. On our age-related bone loss: Insights from a new paradigm. J Bone Miner Res 1997;12:1539-46.

Gennari L, Merlotti D, Valleggi F, Martini G, Nuti R. Selective estrogen receptor modulators for postmenopausal osteoporosis: Current state of development. Drugs Aging 2007;24:361-79.

Geoghegan IP, Hoey DA, McNamara LM. Estrogen deficiency impairs integrin alphavbeta3-mediated mechanosensation by osteocytes and alters osteoclastogenic paracrine signalling. Sci Rep 2019;9:4654.

Giguere V, Yang N, Segui P, Evans RM. Identification of a new class of steroid hormone receptors. Nature 1988;331:91-4.

Gong Y, Slee RB, Fukai N, Rawadi G, Roman-Roman S, Reginato AM, et al. Ldl receptor-related protein 5 (lrp5) affects bone accrual and eye development. Cell 2001;107:513-23.

Hannon R, Blumsohn A, Naylor K, Eastell R. Response of biochemical markers of bone turnover to hormone replacement therapy: Impact of biological variability. J Bone Miner Res 1998;13:1124-33.

Heino TJ, Hentunen TA, Vaananen HK. Osteocytes inhibit osteoclastic bone resorption through transforming growth factor-beta: Enhancement by estrogen. J Cell Biochem 2002;85:185-97.

Holguin N, Brodt MD, Silva MJ. Activation of wnt signaling by mechanical loading is impaired in the bone of old mice. J Bone Miner Res 2016;31:2215-26.

Howell A, Osborne CK, Morris C, Wakeling AE. Ici 182,780 (faslodex): Development of a novel, "pure" antiestrogen. Cancer 2000;89:817-25.

Javaheri B, Stern AR, Lara N, Dallas M, Zhao H, Liu Y, et al. Deletion of a single beta-catenin allele in osteocytes abolishes the bone anabolic response to loading. J Bone Miner Res 2014;29:705-15.

Javaheri B, Stern, A., Lara, N., Dallas, M., Robling A. and Johnson, M.L. Major gender-related differences in bone mass and strength in aged sost knockout mice. J Bone Miner Res 2012;27:S:80.

Kamel MA, Picconi JL, Lara-Castillo N, Johnson ML. Activation of beta-catenin signaling in mlo-y4 osteocytic cells versus 2t3 osteoblastic cells by fluid flow shear stress and pge2: Implications for the study of mechanosensation in bone. Bone 2010a;47:872-81.

Kamel MA, Picconi JL, Lara-Castillo N, Johnson ML. Activation of beta-catenin signaling in mlo-y4 osteocytic cells versus 2t3 osteoblastic cells by fluid flow shear stress and pge(2): Implications for the study of mechanosensation in bone. Bone 2010b;47:872-81.

Kato Y, Windle J, Koop B, Qiao M, Bonewald LF. Establishment of an osteocyte-like cell line, mlo-y4. J Bone Miner Res 1997;12:2014-23.

Kaya S, Basta-Pljakic J, Seref-Ferlengez Z, Majeska RJ, Cardoso L, Bromage TG, et al. Lactation-induced changes in the volume of osteocyte lacunar-canalicular space alter mechanical properties in cortical bone tissue. J Bone Miner Res 2017;32:688-97.

Khosla S, Amin S, Orwoll E. Osteoporosis in men. Endocr Rev 2008;29:441-64.

Khosla S, Melton LJ, Riggs BL. The unitary model for estrogen deficiency and the pathogenesis of osteoporosis: Is a revision needed? J Bone Miner Res 2011;26:441-51.

Kondoh S, Inoue K, Igarashi K, Sugizaki H, Shirode-Fukuda Y, Inoue E, et al. Estrogen receptor alpha in osteocytes regulates trabecular bone formation in female mice. Bone 2014;60:68-77.

Kousteni S, Bellido T, Plotkin LI, O'Brien CA, Bodenner DL, Han L, et al. Nongenotropic, sex-nonspecific signaling through the estrogen or androgen receptors: Dissociation from transcriptional activity. Cell 2001;104:719-30.

Kringelbach TM, Aslan D, Novak I, Schwarz P, Jorgensen NR. Utp-induced atp release is a fine-tuned signalling pathway in osteocytes. Purinergic Signal 2014;10:337-47.

Lara-Castillo N, Kim-Weroha NA, Kamel MA, Javaheri B, Ellies DL, Krumlauf RE, et al. In vivo mechanical loading rapidly activates beta-catenin signaling in osteocytes through a prostaglandin mediated mechanism. Bone 2015;76:58-66.

Li CY, Schaffler MB, Wolde-Semait HT, Hernandez CJ, Jepsen KJ. Genetic background influences cortical bone response to ovariectomy. J Bone Miner Res 2005;20:2150-8.

Li X, Ominsky MS, Niu QT, Sun N, Daugherty B, D'Agostin D, et al. Targeted deletion of the sclerostin gene in mice results in increased bone formation and bone strength. J Bone Miner Res 2008;23:860-9.

Li X, Ominsky MS, Warmington KS, Morony S, Gong J, Cao J, et al. Sclerostin antibody treatment increases bone formation, bone mass, and bone strength in a rat model of postmenopausal osteoporosis. J Bone Miner Res 2009;24:578-88.

Lindsay R, Hart DM, Aitken JM, MacDonald EB, Anderson JB, Clarke AC. Long-term prevention of postmenopausal osteoporosis by oestrogen. Evidence for an increased bone mass after delayed onset of oestrogen treatment. Lancet 1976;1:1038-41.

Little RD, Carulli JP, Del Mastro RG, Dupuis J, Osborne M, Folz C, et al. A mutation in the ldl receptor-related protein 5 gene results in the autosomal dominant high-bone-mass trait. Am J Hum Genet 2002;70:11-9.

Looker AC, Sarafrazi Isfahani N, Fan B, Shepherd JA. Trends in osteoporosis and low bone mass in older us adults, 2005-2006 through 2013-2014. Osteoporos Int 2017;28:1979-88.

MacDonald BT, Tamai K, He X. Wnt/β-catenin signaling: Components, mechanisms, and diseases. Dev Cell 2009;17:9-26.

Manolagas SC, Jilka RL. Bone marrow, cytokines, and bone remodeling. Emerging insights into the pathophysiology of osteoporosis. N Engl J Med 1995;332:305-11.

Manolagas SC, Almeida M. Gone with the wnts: Beta-catenin, t-cell factor, forkhead box o, and oxidative stress in age-dependent diseases of bone, lipid, and glucose metabolism. Mol Endocrinol 2007;21:2605-14.

Marathe N, Rangaswami H, Zhuang S, Boss GR, Pilz RB. Pro-survival effects of 17beta-estradiol on osteocytes are mediated by nitric oxide/cgmp via differential actions of cgmp-dependent protein kinases i and ii. J Biol Chem 2012;287:978-88.

Martin-Millan M, Almeida M, Ambrogini E, Han L, Zhao H, Weinstein RS, et al. The estrogen receptor-alpha in osteoclasts mediates the protective effects of estrogens on cancellous but not cortical bone. Mol Endocrinol 2010;24:323-34.

Mendelsohn ME, Karas RH. Rapid progress for non-nuclear estrogen receptor signaling. J Clin Invest 2010;120:2277-9.

Mittra E, Rubin C, Gruber B, Qin YX. Evaluation of trabecular mechanical and microstructural properties in human calcaneal bone of advanced age using mechanical testing, microct, and dxa. J Biomech 2008;41:368-75.

Modder U, Riggs B, Spelsberg T, Fraser D, Atkinson E, Arnold R, et al. Dose-response of estrogen on bone versus the uterus in ovariectomized mice. Eur J Endocrinol 2004;151:503-10.

Morello KC, Wurz GT, DeGregorio MW. Serms: Current status and future trends. Crit Rev Oncol Hematol 2002;43:63-76.

Mulcahy LE, Taylor D, Lee TC, Duffy GP. Rankl and opg activity is regulated by injury size in networks of osteocyte-like cells. Bone 2011;48:182-8.

Nakamura T, Imai Y, Matsumoto T, Sato S, Takeuchi K, Igarashi K, et al. Estrogen prevents bone loss via estrogen receptor alpha and induction of fas ligand in osteoclasts. Cell 2007;130:811-23.

National Osteoporosis Foundation. Available from www.nof.org. Accessed July 1, 2019.

Negishi-Koga T, Shinohara M, Komatsu N, Bito H, Kodama T, Friedel RH, et al. Suppression of bone formation by osteoclastic expression of semaphorin 4d. Nat Med 2011;17:1473-80.

Nicolella DP, Moravits DE, Gale AM, Bonewald LF, Lankford J. Osteocyte lacunae tissue strain in cortical bone. J Biomech 2006;39:1735-43.

Nilsson S, Mäkelä S, Treuter E, Tujague M, Thomsen J, Andersson G, et al. Mechanisms of estrogen action. Physiol Rev 2001;81:1535-65.

Osterhoff G, Morgan EF, Shefelbine SJ, Karim L, McNamara LM, Augat P. Bone mechanical properties and changes with osteoporosis. Injury 2016;47 Suppl 2:S11-20.

Parfitt AM, Drezner MK, Glorieux FH, Kanis JA, Malluche H, Meunier PJ, et al. Bone histomorphometry: Standardization of nomenclature, symbols, and units: Report of the asbmr histomorphometry nomenclature committee. J Bone Miner Res 1987;2:595-610.

Pinson KI, Brennan J, Monkley S, Avery BJ, Skarnes WC. An ldl-receptor-related protein mediates wnt signalling in mice. Nature 2000;407:535-8.

Qing H, Ardeshirpour L, Pajevic PD, Dusevich V, Jahn K, Kato S, et al. Demonstration of osteocytic perilacunar/canalicular remodeling in mice during lactation. J Bone Miner Res 2012;27:1018-29.

Raisz LG. Pathogenesis of osteoporosis: Concepts, conflicts, and prospects. J Clin Invest 2005;115:3318-25.

Recker R, Lappe J, Davies K, Heaney R. Characterization of perimenopausal bone loss: A prospective study. J Bone Miner Res 2000;15:1965-73.

Ren J, Wang XH, Wang GC, Wu JH. 17beta estradiol regulation of connexin 43-based gap junction and mechanosensitivity through classical estrogen receptor pathway in osteocyte-like mlo-y4 cells. Bone 2013;53:587-96.

Revankar CM, Cimino DF, Sklar LA, Arterburn JB, Prossnitz ER. A transmembrane intracellular estrogen receptor mediates rapid cell signaling. Science 2005;307:1625-30.

Riggs BL, Melton LJ, 3rd. Involutional osteoporosis. N Engl J Med 1986;314:1676-86.

Riggs BL, Khosla S, Melton LJ. Sex steroids and the construction and conservation of the adult skeleton. Endocr Rev 2002;23:279-302.

Robinson JA, Chatterjee-Kishore M, Yaworsky P, Cullen DM, Zhao W, Li C, et al. Wnt/β-catenin signaling is a normal physiological response to mechanical loading in bone. J Biol Chem 2006;281:31720-8.

Robling AG, Niziolek PJ, Baldridge LA, Condon KW, Allen MR, Alam I, et al. Mechanical stimulation of bone in vivo reduces osteocyte expression of sost/sclerostin. J Biol Chem 2008;283:5866-75.

Rosales Rocabado JM, Kaku M, Nozaki K, Ida T, Kitami M, Aoyagi Y, et al. A multi-factorial analysis of bone morphology and fracture strength of rat femur in response to ovariectomy. J Orthop Surg Res 2018;13:318.

Sato T, Fukazawa Y, Kojima H, Ohta Y, Iguchi T. Multiple mechanisms are involved in apoptotic cell death in the mouse uterus and vagina after ovariectomy. Reprod Toxicol 2003;17:289-97.

Sawakami K, Robling AG, Ai M, Pitner ND, Liu D, Warden SJ, et al. The wnt co-receptor lrp5 is essential for skeletal mechanotransduction, but not for the anabolic bone response to parathyroid hormone treatment. J Biol Chem 2006;281:23698-711.

Sharma D, Ciani C, Marin PA, Levy JD, Doty SB, Fritton SP. Alterations in the osteocyte lacunar-canalicular microenvironment due to estrogen deficiency. Bone 2012;51:488-97.

Song RX, Santen RJ. Apoptotic action of estrogen. Apoptosis 2003;8:55-60.

Srivastava S, Toraldo G, Weitzmann MN, Cenci S, Ross FP, Pacifici R. Estrogen decreases osteoclast formation by down-regulating receptor activator of nf-kappa b ligand (rankl)-induced jnk activation. J Biol Chem 2001;276:8836-40.

Stern AR, Yao X, Wang Y, Berhe A, Dallas M, Johnson ML, et al. Effect of osteoporosis treatment agents on the cortical bone osteocyte microenvironment in adult estrogen-deficient, osteopenic rats. Bone Rep 2018;8:115-24.

Tamai K, Semenov M, Kato Y, Spokony R, Liu C, Katsuyama Y, et al. Ldl-receptor-related proteins in wnt signal transduction. Nature 2000;407:530-5.

Tomkinson A, Reeve J, Shaw RW, Noble BS. The death of osteocytes via apoptosis accompanies estrogen withdrawal in human bone. J Clin Endocrinol Metab 1997;82:3128-35.

Tomkinson A, Gevers EF, Wit JM, Reeve J, Noble BS. The role of estrogen in the control of rat osteocyte apoptosis. J Bone Miner Res 1998;13:1243-50.

Wakeling AE. Use of pure antioestrogens to elucidate the mode of action of oestrogens. Biochem Pharmacol 1995;49:1545-9.

Wang K, Le L, Chun BM, Tiede-Lewis LM, Shiflett LA, Prideaux M, et al. A novel osteogenic cell line that differentiates into gfp-tagged osteocytes and forms mineral with a bone-like lacunocanalicular structure. J Bone Miner Res 2019;34:979-95.

Wehrli M, Dougan ST, Caldwell K, O'Keefe L, Schwartz S, Vaizel-Ohayon D, et al. Arrow encodes an ldl-receptor-related protein essential for wingless signalling. Nature 2000;407:527-30.

Wijayaratne AL, McDonnell DP. The human estrogen receptor-alpha is a ubiquitinated protein whose stability is affected differentially by agonists, antagonists, and selective estrogen receptor modulators. J Biol Chem 2001;276:35684-92.

Windahl SH, Borjesson AE, Farman HH, Engdahl C, Moverare-Skrtic S, Sjogren K, et al. Estrogen receptor-alpha in osteocytes is important for trabecular bone formation in male mice. Proc Natl Acad Sci U S A 2013a;110:2294-9.

Windahl SH, Saxon L, Borjesson AE, Lagerquist MK, Frenkel B, Henning P, et al. Estrogen receptor-alpha is required for the osteogenic response to mechanical loading in a ligand-independent manner involving its activation function 1 but not 2. J Bone Miner Res 2013b;28:291-301.

Woo SM, Rosser J, Dusevich V, Kalajzic I, Bonewald LF. Cell line idg-sw3 replicates osteoblast-to-late-osteocyte differentiation in vitro and accelerates bone formation in vivo. J Bone Miner Res 2011;26:2634-46.

Wood GA, Fata JE, Watson KL, Khokha R. Circulating hormones and estrous stage predict cellular and stromal remodeling in murine uterus. Reproduction 2007;133:1035-44.

World Health Organization. Assessment of fracture risk and its application to screening for postmenopausal osteoporosis: Report of a WHO study group [meeting held in rome from 22 to 25 june 1992]. 1994.

Yee CS, Schurman CA, White CR, Alliston T. Investigating osteocytic perilacunar/canalicular remodeling. Curr Osteoporos Rep 2019;17:157-68.

Zaman G, Jessop HL, Muzylak M, De Souza RL, Pitsillides AA, Price JS, et al. Osteocytes use estrogen receptor α to respond to strain but their erα content is regulated by estrogen. J Bone Miner Res 2006;21:1297-306.

Zhang Y, Lai WP, Leung PC, Wu CF, Wong MS. Short- to mid-term effects of ovariectomy on bone turnover, bone mass and bone strength in rats. Biol Pharm Bull 2007;30:898-903.

VITA

NAME

Erica N. M. Jackson

EDUCATION

2002-2006	B.S. Health Promotions, Biology Minor	Emporia State University
2006-2008	M.A. Biology, emphasis in A&P	Emporia State University

TEACHING EXPERIENCE

2008-2009	Visiting Faculty Member-Biology Dept.	Emporia State University
2008-2009	Adjunct Professor	Flint Hills Technical College
2009-Present	Lecturer-Biology Department	Washburn University

PROFESSIONAL ORGANIZATIONS

American Society of Bone and Mineral Research (ASBMR)

PRESENTATIONS (* denotes presenter)

Nuria Lara-Castillo; Erica Jackson; Kika Masunaga; Mark Dallas; Mark Gray; Julian Vallejo; Michael Wacker and *Mark L. Johnson. “The Role of Estrogen in Bone-Muscle Crosstalk” Indiana University Bone Muscle Day August 16, 2019

*Erica Jackson, Nuria Lara-Castillo, Mohammed Akhter and Mark L. Johnson “Osteocyte Wnt/β-catenin Pathway Activation upon Mechanical Loading is Altered in OVX Mice” ASBMR Annual Meeting, Orlando FL, September 21, 2019